

2-11
2002

**LIBRARY
Michigan State
University**

This is to certify that the
dissertation entitled

COUPLING BETWEEN CAVITY-BACKED ANTENNAS
ON AN ELLIPTIC CYLINDER

presented by

Chi-Wei Wu

has been accepted towards fulfillment
of the requirements for

PhD degree in Electrical Eng



Major professor

Date 12/03/01

PLACE IN RETURN BOX to remove this checkout from your record.
TO AVOID FINES return on or before date due.
MAY BE RECALLED with earlier due date if requested.

DATE DUE	DATE DUE	DATE DUE

**COUPLING BETWEEN CAVITY-BACKED ANTENNAS ON
AN ELLIPTIC CYLINDER**

By

Chi-Wei Wu

A DISSERTATION

Submitted to
Michigan State University
in partial fulfillment of the requirements
for the degree of

DOCTOR OF PHILOSOPHY

Department of Electrical and Computer Engineering

2001

ABSTRACT

COUPLING BETWEEN CAVITY-BACKED ANTENNAS ON AN ELLIPTIC CYLINDER

By

Chi-Wei Wu

Radiation by conformal antennas, flush-mounted to surfaces with varying curvature, is of considerable importance to design engineers. Applications of such antennas are found in the aerospace, automobile, and watercraft industries. Conformal antennas are important in these areas due to their relatively low cost, low profile, and consumer appeal. However, accurate and flexible design methods for such antennas have not been offered in the literature to date.

In this research, the highly versatile finite element method is combined in a hybrid formulation with a boundary integral mesh closure scheme to accurately model the fields within, and in the aperture of, a cavity-backed antenna flush-mounted in a perfectly conducting infinite elliptic cylinder. For the sake of efficiency, an asymptotically valid dyadic Green's function based on the Uniform Theory of Diffraction (UTD) for surface fields due to a source on a smooth perfectly conducting surface with arbitrary curvature is used in the boundary integral. This development represents a significant advancement over prior techniques since surface curvature variation, either across a single element or across an array of elements, is now accurately included into the antenna model. An advantage of this approach is the ability to model cavities with curvature varying from

planar to the constant curvature of a circular cylinder. Eigenmodes will be given for planar-rectangular, circular-rectangular, and elliptic-rectangular cavities recessed in the cylinder. Furthermore, the input impedance of a conformal cavity-backed patch antenna will be given. Also, The mutual coupling between microstrip antennas mounted in a ground plane, a circular and an elliptic cylinder is investigated in this research.

to every member of my family

ACKNOWLEDGEMENTS

In August 2000, I considered quitting my Ph.D. studies when I was informed that my mother had a serious stroke and had been unconscious for more than one week after major brain surgery. It would not have been possible for me to continue this dissertation without the strong support from all my family members, especially my father, Hwa Jing, who quick from his job after that. I also want to express my sincere appreciation to my young sister, Soal-Phane, and my two brothers, Chung-Yi, and Ling-Gate for taking turns caring for mother after normal working hours. Without their sacrifice and patience, I could not focus on my studies and complete this research effort while living more than ten thousand miles away from home. Special thanks go to my loving wife, Kwei-Yin, for devoting herself to take a good care of my daily life without complaining.

In addition to my family members, those people who guided me academically have been equally important. I'd like to thank the members of my thesis committee for their time and insight. Especially, I am grateful to my two advisors, Dr. Kempel and Dr. Edward Rothwell for their enthusiastic guidance over the years. I am also grateful to Dr. Dennis Nyquist for the valuable advice and mentoring he has provided. Finally I would like to thanks Dr. Byron Drachman for his time throughout this study.

Appreciation is extended to Taiwan Department of Defense for providing financial support in the past four years.

TABLE OF CONTENTS

LIST OF TABLES	viii
LIST OF FIGURES	ix
CHAPTER 1	
Introduction	1
CHAPTER 2	
2.1 Introduction.....	8
2.2. FE-BI formulation.....	8
2.3. Vector Weight Functions	13
2.4. Finite Element Matrix	17
2.5. Validation of Finite Element Formulation: The Closed Cavity	20
CHAPTER 3	
3.1 Introduction	33
3.2 Eigenfunction expansion method	34
3.2.1 Mathieu's Equation	34
3.2.2 Modified Mathieu's Equation	37
3.2.3 Vector Wave Functions In An Elliptic Cylinder Coordinate System	39
3.2.4 The Free-Space Dyadic Green's function	42
3.2.5 The Electric Dyadic Green's function Of The First Kind	49
3.2.6 The Electric Dyadic Green's function Of The Second Kind	51
3.3 The Asymptotic Dyadic Green's Function	53
3.4 Boundary Integral Matrix	57
3.5 Excitation: FE-BI	60
CHAPTER 4	
4.1 Introduction.....	69
4.2 System Solution	70
4.3 Input Impedance.....	71
4.4 Numerical Results and Discussions	74
4.4.1 The Empty Cavity.....	74

4.4.2 The Slot Antenna	75
4.4.3 The Conformal Patch Antenna	77
4.5 Conclusion	81
CHAPTER 5	
5.1 Introduction.....	107
5.2 Mutual Coupling	108
5.3 Numerical Results and Discussions.....	109
5.3.1 Comparisons between FE-BI and Moment Method for H-Plane Coupling.....	110
5.3.2 Comparisons between FE-BI and Moment Method for E-Plane Coupling	113
5.3.3 Numerical Results and Discussions for H-Plane Coupling on a Curved Surface.....	114
5.3.4 Numerical Results and Discussions for E-Plane Coupling on a Curved Surface.....	116
5.3.5 Numerical Results for Different Size of Patch Antenna.....	120
5.4 Conclusion	122
CHAPTER 6	
Conclusion	159
BIBLIOGRAPHY	164

LIST OF TABLES

Table 2.1	The eigenvalues for a rectangular cavity.....	23
Table 2.2	The eigenvalues for a circular shell cavity.....	24
Table 2.3	The eigenvalues for a circular shell cavity.....	25
Table 2.4	The eigenvalues for an elliptic shell cavity.....	26
Table 2.5	Comparison of eigenvalues between a cavity	27
Table 2.6	Comparison of eigenvalues between a cavity	28

LIST OF FIGURES

Figure 2.1	A cross-sectional view of the elliptic coordinate system	29
Figure 2.2	The geometry of the cavity-backed antenna embedded in a metallic elliptic cylinder	30
Figure 2.3	Geometry of an elliptic shell element	31
Figure 2.4	Geometry of a cylindrical shell element	32
Figure 3.1	Contour for converting the eigenfunction expansion into a mode expansion.....	62
Figure 3.2	The scattering wave and incident wave for an elliptic cylinder	63
Figure 3.3	Illustration of unit vectors for a convex surface.....	64
Figure 3.4	Geodesic path for the creeping wave on an elliptic cylinder	65
Figure 3.5	Magnitude of the three components of asymptotic dyadic Green's function for an elliptic cylinder	66
Figure 3.6	Magnitude of the three components of asymptotic dyadic Green's Function for a circular cylinder	67
Figure 3.7	Cavity-backed probe-fed conformal patch antenna recessed in an infinite, perfectly conducting elliptic cylinder	68
Figure 4.1	The geometry of model of source generator	80
Figure 4.2	An empty cavity: 1.5 cm x 6.0 cm x 3.75 cm and its unit cell.....	81
Figure 4.3	Input impedance for an empty cavity mounted in the ground.....	82

F

F

F

Fi

Fi

Fig

Fig

Figure 4.4	Input impedance for an empty cavity mounted in two circular cylinders with different radii	83
Figure 4.5	Slot antenna: 1.5 cm x 6.0 cm x 3.75 cm and its unit cell.....	84
Figure 4.6	Input impedance for slot antenna embedded in a ground plane	85
Figure 4.7	Input resistance for slot antenna on cylinders	86
Figure 4.8	Input reactance for slot antenna on cylinders	87
Figure 4.9	Input resistance for slot antenna on cylinder and elliptic cylinder.....	88
Figure 4.10	Input reactance for slot antenna on cylinder and elliptic cylinder	91
Figure 4.11	Fields configurations (modes) for rectangular microstrip patch	92
Figure 4.12	Input impedance for rectangular patch antenna in a ground plane	93
Figure 4.13	Input impedance for rectangular patch antenna in a ground plane	94
Figure 4.14	Input impedance for rectangular patch antenna in a ground plane	95
Figure 4.15	Input impedance for rectangular patch antenna in a ground plane	96
Figure 4.16	Patch antenna: 1.5 cm x 6.0 cm x 3.75 cm.....	97
Figure 4.17	Input impedance for a patch antenna in a ground plane.....	98
Figure 4.18	Resistance for a patch antenna on cylinders	99
Figure 4.19	Reactance for a patch antenna on cylinders	100

Figure 4.20	Resistance for a patch antenna on cylinders with azimuthal polarization	101
Figure 4.21	Reactance for a patch antenna on cylinders with azimuthal polarization	102
Figure 4.22	Resistance for a patch antenna on cylinders with azimuthal polarization	103
Figure 4.23	Reactance for a patch antenna on cylinders with azimuthal polarization	104
Figure 4.24	Resistance for a patch antenna on elliptic cylinders with azimuthal polarization.....	105
Figure 4.25	Reactance for a patch antenna on elliptic cylinders with azimuthal polarization.....	106
Figure 5.1	Experimental arrangement for measurement of microstrip antenna S-parameter Geometry of an elliptic shell element	125
Figure 5.2	Measured and calculated mutual coupling between two coax-fed microstrip antennas	126
Figure 5.3	Geometry for patch antennas with H-plane coupling in pseudo- ground plane	127
Figure 5.4	Mutual coupling for H-plane case.....	128
Figure 5.5	Comparison of mutual coupling calculated by FE-BI with a moment method solution and data by measurements.....	129
Figure 5.6	Comparison of mutual coupling using FE-BI method between different size of cavity.....	130

Figure 5.7	Geometry for patch antennas with H-plane coupling in pseudo-ground plane	131
Figure 5.8	Comparison of mutual coupling calculated by FE-BI with a moment method solution and data by measurements.....	132
Figure 5.9	Comparison of mutual coupling calculated by FE-BI with a moment method solution and data by measurements	133
Figure 5.10	Geometry for patch antennas with E-plane coupling in a pseudo-plane ground.....	134
Figure 5.11	Comparison of mutual coupling calculated by FE-BI with a moment method solution and data by measurements	135
Figure 5.12	Comparison of mutual coupling calculated by FE-BI with a moment method solution and data by measurements	136
Figure 5.13	Geometry for patch antennas mounted in curved surface with H-plane Coupling.....	137
Figure 5.14	Mutual resistance for patch antennas with H-plane coupling	138
Figure 5.15	Mutual reactance for patch antennas with H-plane coupling.....	139
Figure 5.16	Mutual Coupling for patch antennas with H-plane coupling	140
Figure 5.17	Mutual resistance for patch antennas mounted in an elliptic cylinder with H-plane coupling.....	141
Figure 5.18	Mutual reactance for patch antennas mounted in an elliptic cylinder with H-plane coupling.....	142
Figure 5.19	Mutual coupling for patch antennas mounted in an elliptic cylinder with H-plane coupling.....	143

Figure 5.20	Geometry for patch antennas mounted in curved surface with E-plane coupling.....	144
Figure 5.21	Mutual resistance for patch antennas with E-plane coupling.....	145
Figure 5.22	Mutual reactance for patch antennas with E-plane coupling	146
Figure 5.23	Mutual Coupling for patch antennas with E-plane coupling.....	147
Figure 5.24	Mutual resistance for patch antennas mounted in an elliptic cylinder with E-plane coupling	148
Figure 5.25	Mutual reactance for patch antennas mounted in an elliptic cylinder with E-plane coupling	149
Figure 5.26	Mutual coupling for patch antennas mounted in an elliptic cylinder with E-plane coupling	150
Figure 5.27	Geometry for patch antennas mounted in curved surface with special E-plane coupling	151
Figure 5.28	Mutual resistance for patch antennas with special E-plane coupling.....	152
Figure 5.29	Mutual reactance for patch antennas with special E-plane coupling	153
Figure 5.30	Mutual Coupling for patch antennas with special E-plane coupling	154
Figure 5.31	Geometry for patch antennas with different patch size.....	155
Figure 5.32	Mutual Coupling between antennas	156
Figure 5.33	Mutual Coupling between antennas	157
Figure 5.34	Mutual Coupling between antennas	158

CHAPTER 1

INTRODUCTION

Conformal antennas are increasingly being mounted on the surfaces of air vehicles primarily due to their low volume consumption, low drag, and low cost array properties. An antenna that has received considerable attention in the literature is the microstrip patch. This antenna consists of a radiating metallic patch printed on a grounded dielectric substrate. Typically these antennas are designed using analysis methods developed for planar apertures. Often such an approach is sufficient for design purposes; however, there are significant applications where explicit inclusion of surface curvature is necessary. For example, a characteristic phenomenon of patch antennas conformal to curved platforms is the dependence of resonant input impedance on surface curvature [1]. During the previous development of these antennas, due to a lack of rigorous analysis techniques, antenna designers have had to resort to expensive measurements in order to develop a conformal array design. This process is very time-consuming since any change in the antenna geometry will necessitate re-measurement, especially at the resonant frequency, of the input impedance and mutual coupling properties of the antenna. Due to the narrow bandwidth of patch antennas, it is important to include variations in the input impedance attributed to curvature so that the number of prototypes required during the design cycle can be minimized.

Various theoretical techniques have been employed in the past for the analysis and design of conformal antennas such as the cavity model [2], integral equation based methods [3-5], and mode-matching techniques [6]. Many of these techniques were originally developed for planar surfaces; however, they have also been extended to

inc

dis

the

ign

off

the

for

ant

lim

the

bee

Bot

BI r

cyli

the

cyli

una

suit

ava

bou

con

incorporate surface curvature [2]. Each of these methods has advantages and disadvantages.

The cavity model is computationally inexpensive and offers considerable insight into the behavior of the antenna. However, it is not amenable to large array simulation since it ignores mutual interactions amongst array elements. The integral equation-based methods offer high accuracy through the rigorous inclusion of mutual coupling effects. However, these are not particularly efficient due to the fully-populated matrix associated with the formulation. Highly efficient methods can be developed, particularly for cavity-backed antennas; however, in doing so the antenna element shape and cavity shape are typically limited [7].

The finite element-boundary integral (FE-BI) method is successfully employed for the analysis of large planar arrays of arbitrary composition [8], and this approach has been extended for aperture antennas conformal to a circular cylinder metallic surface [9]. Both the radiation and scattering problems have been developed in the context of the FE-BI method. In contrast to the planar aperture array, the implementation of the cylindrically conformal array requires cylindrical shell elements rather than bricks, and the required external Green's function is that of the circular perfectly conducting cylinder. In its exact form, this Green's function is an infinite series that imposes unacceptable computational burden on the method. However, for large radius cylinders, suitable asymptotic formulas developed from Uniform Theory of Diffraction (UTD) are available and used for an efficient evaluation of the Green's function. The finite element-boundary integral (FE-BI) method provides an alternative approach to modeling conformal antennas for both planar [8] and curved platforms [9-10].

bo

ele

the

a f

cap

ele

ape

ord

eler

on t

of a

amo

confi

curva

reson

estab

rectar

associ

a cavi

V

the ell

1994

The FE-BI approach is a hybrid method combining the finite element method with a boundary integral. The finite element method is used to model the volumetric total electric fields in the cavity as well as the tangential electric fields in the aperture. With the FE-BI method, the constitutive material parameters are assumed to be constant within a finite element but are allowed to vary across elements; consequently, this method is capable of modeling cavity-backed antennas with inhomogeneous loading. Hence, a finite element based model is capable of being used to design both geometrically complex apertures and apertures with complex material loading. However, as with all second-order partial differential equation based representations of the wave equation, the finite element method requires specification of both the tangential electric and magnetic fields on the boundary of the computational volume. This is accomplished via the introduction of a boundary integral that includes a dyadic Green's function to describe the coupling amongst various portions of the aperture.

In this research, the FE-BI method is extended to model cavity-backed antennas conformal to a perfectly conducting elliptic cylinder that has a surface with varying curvature along one principal plane. This hybrid FE-BI method will be used to model the resonant behavior of cavities recessed in an elliptic cylinder and its validity will be established by reduction to known results for planar-rectangular and cylindrical-rectangular cavities. In addition, new results will be presented for the resonance associated with an elliptic-rectangular cavity and for the input impedance associated with a cavity-backed patch antenna flush-mounted on an elliptic cylinder.

Vector wave equations in an elliptic cylinder coordinate system are generated when the elliptic cylinder scalar wave functions are used. Once the orthogonal properties of

these

dyac

equa

the s

poss

usec

func

With

form

elem

elem

shel

expa

a co

whil

serie

succ

this c

very

perfo

these functions are known, we can find the eigenfunction expansion of the free-space dyadic Green function [11].

In Chapter 2, the FE-BI formulation will be introduced first using the vector wave equation in elliptic cylinder coordinates and be extended to cavities that are embedded on the surface of a metallic elliptic cylinder of infinite extent. Since the elliptic shell element possess both geometrical fidelity and simplicity for the elliptic-rectangular cavity, it is used to mesh the elliptic cavity-backed conformal antenna volume. New vector weight functions for the each edge of the elliptic shell element are presented in this dissertation. With these vector weight functions, the FE-BI can be written as a matrix equation and the formulations for each matrix entry are shown in Chapter 2. For validation of the finite element formulation, a comparison between computed eigenvalues using the finite element method and analytical values for a closed rectangular cavity and a closed circular shell cavity is made.

In Chapter 3, the free space dyadic Green function in terms of eigenfunction expansion is developed. The angular functions, or Mathieu functions, are represented by a cosine series in the case of even functions and a sine series in the case of odd functions while the radial functions, or modified Mathieu functions, are expressed in the form of a series of Bessel functions. Each dyadic component of the dyadic Green function has been successfully developed in terms of Mathieu functions or modified Mathieu functions in this chapter; however, the convergence performance of the modified Mathieu functions is very slow. Hence an asymptotic dyadic Green function that has a good convergence performance is developed and used.

I

Theo

Gree

same

elect

the s

Gree

form

form

func

comp

pseu

In

print

cavit

prese

From

anten

discu

locati

In

plane

Base on the development of an approximate asymptotic solution using the Uniform Theory of Diffraction (UTD) for surface fields by Pathak and Wang [12], the dyadic Green function is derived for both a source point and an observation point located on the same surface of the elliptic cylinder, and thus an approximate asymptotic solution for the electromagnetic fields that are induced by an infinitesimal magnetic current moment on the same elliptic surface is generated. In this approach the contributions to the dyadic Green function for the short path and long path are developed. The reduction of this formulation for the special case of a circular cylinder will be shown to have the same form as previous results [9]. The numerical results for the magnitude of the dyadic Green function with respect to the geodesic path will be discussed in Chapter 3. The numerical comparison will be demonstrated there for a wave traveling on an elliptic cylinder and a pseudo-circular cylinder.

In Chapter 4, the calculation model for the input impedance of a cavity-backed, printed antenna is introduced. The input impedance and resonant frequency for an empty cavity, a slot antenna and a conformal patch antenna embedded on a ground plane are presented as well as antennas recessed in an elliptic cylinder and a circular cylinder. From those numerical results, the relationship between the input impedance of different antennas and the local surface curvature in the vicinity of the antenna mount is found and discussed. Also, the probe feed for the patch antennas will be located in different locations to observe effects of the surface curvature with different excited modes.

In Chapter 4, the computation results using FE-BI for antennas mounted in a ground plane is verified with planar FE-BI results [10] by setting the radius of curvature to be

large. Also, for the empty cavity mounted in a ground plane, the calculated resonant frequency will be compared with the theoretical value.

In Chapter 5, the mutual coupling between microstrip antennas mounted in a ground plane, and in a circular and an elliptic cylinder is investigated. A moment method solution to the microstrip antenna problem was proposed [13] in 1981 and the mutual coupling between patch antennas embedded on an infinite coated ground plane was calculated and measured in [14] and [15], respectively. The numerical results using the FE-BI method are compared to these moment method results.

The mutual coupling between patch antennas embedded in different circular cylinders with different radii are calculated. The mutual resistance, reactance and coupling coefficient, S_{12} , are graphed with respect to frequency to assess the effects of curvature on coupling. Also the same antenna is mounted in the different portions of the elliptic cylinder and the computed results are discussed. The field structure with the cavity is mainly dependent on the position of the probe feed this affects the mutual coupling. Therefore, the probe feed is relocated and numerical results for coupling are inspected to determine the influences of the location of the probe feed.

In addition to curvature, the position of the probe feed, the size of the patches and the separation between the two rectangular patches play an important role in mutual coupling. In Chapter 5, the different patch sizes are used to analyze mutual coupling. Also, numerical results are computed for the antenna mounted in circular cylinders with different radii. For convenience, symmetric patches are used for computation.

th

im

In Chapter 5, a two-port network model is used to determine mutual coupling. Also, the coupling parameter, S_{12} , is determined from the input impedance and mutual impedance using conversion between two-port network parameters.

2.1 In

T

mathe

Integr

Hsieh

there

of ele

contri

Fouri

low O

to cav

that w

may b

In

the su

metho

introd

2.2. F

B

perame

• • • • •

CHAPTER 2

FINITE ELEMENT–BOUNDARY INTEGRAL METHOD

2.1 Introduction

The Finite Element (FE) Method is a computational technique that has been used in mathematical physics since the 1940's. It was first coupled with an exact Boundary Integral (BI) termination condition in an electromagnetics application by Silvester and Hsieh [16] and McDonal and Wexler [17] in 1971 and 1972, respectively. In the 1990's, there has been renewed interest in the Finite Element-Boundary Integral (FE-BI) method of electromagnetics principally due to the work of Jin and Volakis [18-20]. Their major contribution was coupling the FE-BI approach with the Biconjugate Gradient-Fast Fourier Transform (BiCG-FFT) technique, thus allowing high fidelity simulations with low $O(N)$ memory and computational demand. In 1994, the FE-BI method was extended to cavities that are recessed in a metallic circular cylinder of infinite extent [1] and [9], In that work, the boundary integral utilized uniform zoning and hence the Bi-CG-FFT solver may be employed to retain low memory and computational burden.

In this chapter the FE-BI method will be extended to cavities that are embedded on the surface of a metallic elliptic cylinder of infinite extent. The derivation of the FE method starting with the vector wave equation will be presented first, followed by the introduction of the boundary integral in the next Chapter.

2.2. FE-BI formulation

Before the scalar wave equation in elliptic cylinder coordinates is discussed, the parameters of elliptic cylinder coordinate system are described. As shown in Figure 2.1,

the re
are g

where

C

2.2. T

the ca

T

differe

manip

where

A

bounda

weighte

valued

given b

the relations between the rectangular coordinate and elliptic cylinder coordinate systems are given by

$$\begin{aligned} x &= c \cosh u \cos v \\ y &= c \sinh u \sin v \quad \text{for } 0 \leq v \leq 2\pi, 0 \leq u < \infty \\ z &= z \end{aligned} \quad (2.1)$$

where $2c$ is the distance between the foci of the ellipse.

Consider a cavity recessed in an infinite metallic elliptic cylinder, shown in Figure 2.2. The cavity walls are assumed to coincide with constant u -, v -, and z -surfaces and the cavity is filled with an inhomogeneous, isotropic material.

The FE-BI formulation is developed by considering the coupled first-order partial differential equations, the time harmonic Maxwell's Equations, and performing some manipulations, to give the vector wave equation,

$$\begin{aligned} \nabla \times \nabla \times \mathbf{E} - k^2 \mathbf{E} &= -j\omega\mu\mathbf{J} - \nabla \times \mathbf{M} \\ \nabla \times \nabla \times \mathbf{H} - k^2 \mathbf{H} &= -j\omega\epsilon\mathbf{M} + \nabla \times \mathbf{J} \end{aligned} \quad (2.2)$$

where \mathbf{J} and \mathbf{M} represent, respectively, the electric and magnetic source current.

A unique solution of the wave equation requires the specification of sufficient boundary conditions. To generate a system of equations from (2.2), the method of weighted residuals is applied, which results in the symmetric inner product of a vector-valued weight function and the vector wave equation. The integro-differential equation is given by

where

V_i is the

source

this in

Upon a

the time

(2.3) ca

where n

with the

magnetic

$$\begin{aligned}
& \int_{V_i} \left[\mathbf{W}_i(u, v, z) \cdot \nabla \times \left(\frac{\nabla \times \mathbf{E}(u, v, z)}{\mu_r} \right) - k_0^2 \mathbf{W}_i(u, v, z) \cdot \epsilon_r \mathbf{E} \right] dV = \\
& - \int_{V_i} \mathbf{W}_i(u, v, z) \cdot \nabla \times \left[\frac{\mathbf{M}^i(u, v, z)}{\mu_r} \right] dV \\
& - jk_0 z_0 \int_{V_i} \mathbf{W}_i(u, v, z) \cdot \mathbf{J}^i(u, v, z) dV
\end{aligned} \tag{2.3}$$

where $\mathbf{W}_i(u, v, z)$ is a subdomain vector-valued weight function to be defined later and V_i is the i^{th} volume element resulting from a discretization of the cavity. The impressed sources ($\mathbf{J}^i, \mathbf{M}^i$) enclosed by the volume V_i give rise to the right-hand side of (2.3) and this interior excitation function is defined by

$$f_i^{\text{int}} = - \int_{V_i} \mathbf{W}_e(u, v, z) \cdot \nabla \times \left[\frac{\mathbf{M}^i(u, v, z)}{\mu_r} \right] dV - jk_0 z_0 \int_{V_i} \mathbf{W}_i(u, v, z) \cdot \mathbf{J}^i(u, v, z) dV \tag{2.4}$$

Upon application of the first vector Green's theorem [11],

$$\int_V \mathbf{W} \cdot \nabla \times (\nabla \times \mathbf{E}) dV = \int_V (\nabla \times \mathbf{E}) \cdot (\nabla \times \mathbf{W}) dV - \int_S \mathbf{W} \times (\nabla \times \mathbf{E}) \cdot \mathbf{n} dS \tag{2.5}$$

the time Harmonic Faraday's Law for a source free region and the vector identity,

$$\nabla \times \mathbf{E} = -j\omega u \mathbf{H} \tag{2.6}$$

$$\mathbf{A} \cdot \mathbf{B} \times \mathbf{C} = \mathbf{C} \cdot \mathbf{A} \times \mathbf{B} \tag{2.7}$$

(2.3) can be recognized as the weak form of the wave equation

$$\begin{aligned}
& \int_{V_i} \frac{\nabla \times \mathbf{E}(u, v, z) \cdot \nabla \times \mathbf{W}_i(u, v, z)}{\mu_r} dV - k_0^2 \int_{V_i} \epsilon_r \mathbf{E} \cdot \mathbf{W}_i(u, v, z) dV - \\
& - jk_0 z_0 \int_{S_i} \mathbf{n}(u, v, z) \times \mathbf{H}(u, v, z) \cdot \mathbf{W}_i(u, v, z) ds = f_i^{\text{int}}
\end{aligned} \tag{2.8}$$

where $\mathbf{n}(u, v, z)$ indicates the outward pointing normal of the element surface associated with the i^{th} unknown, S_i is the surface area of that element, and $\mathbf{H}(u, v, z)$ is the total magnetic field, evaluated at the test point denoted by the triplet (u, v, z) . It can be shown

that

apert

field

the c

zero

field

equi

kind

that

to

when

deno

the e

medi

Y

and s

that the surface integral of (2.8) vanishes for all elements that do not border the cavity aperture due to the fact that the test function, $\mathbf{W}_i(u, v, z)$, is in fact a tangential electric field. For this formulation, all metal is assumed to be a perfect electrical conductor and the only portion of the cavity boundary that is not metal is the aperture. Hence, the non-zero contribution is limited to the portion of the surface that coincides with the aperture.

The weak form of the wave equation, (2.8), contains unknown electric and magnetic fields on the surface of the elliptic cylinder. To determine \mathbf{H} in (2.8), the surface equivalence theorem will be introduced with a dyadic Green's function of the second kind (e.g. a dyadic Green's function that satisfies the Neumann boundary condition) such that the radiated fields due to the equivalent currents can be reduced from [21].

$$\mathbf{H}(\mathbf{r}) = \iint_S \mathbf{n} \times \mathbf{H} \cdot \nabla \times \overline{\overline{G}}(R) dS + jkY \iint_S \mathbf{n} \times \mathbf{E} dS \quad (2.9)$$

to

$$\mathbf{H}(\mathbf{r}) = jkY \iint_S \mathbf{n} \times \mathbf{E} \cdot \overline{\overline{G}}_2(R) dS \quad (2.10)$$

where $\overline{\overline{G}}$, $\overline{\overline{G}}_2$ represent the dyadic Green's function and its second kind, $R = |\mathbf{r} - \mathbf{r}'|$, \mathbf{r} denotes the observation point and \mathbf{r}' is the integration point, while the surface on which the equivalence theorem is applied is denoted by S . Also, Y is the wave admittance in the medium.

By expanding the unknown electric field in terms of subdomain basis functions as

$$\mathbf{E} = \sum_{j=1}^{N_v} E_j \mathbf{W}_j(u, v, z) \quad (2.11)$$

and substituting (2.11) and (2.10) into (2.8), the resulting system of equations is obtained

In (2

exp

func

the t

aper

edge

equa

when

The F

$$\begin{aligned}
\sum_{j=1}^{N_v} E_j \left\{ \int_{V_i} \left[\frac{\nabla \times \mathbf{W}_j(u, v, z) \cdot \nabla \times \mathbf{W}_i(u, v, z)}{\mu_r} \right. \right. \\
\left. \left. - k_0^2 \epsilon_r \mathbf{W}_j(u, v, z) \cdot \mathbf{W}_i(u, v, z) \right] dV \right. \\
\left. + k_0^2 \delta_a(i) \delta_a(j) \int_{S_j} \int_{S_i} \mathbf{W}_i(u, v, z) \cdot \mathbf{u}(u, v, z) \times \right. \\
\left. [\mathbf{u}(u, v, z) \times \mathbf{W}_j(u, v, z) \cdot \overline{\overline{G}}_{e2}(v, z; v', z')] dS dS' \right\} = f_i^{\text{int}}
\end{aligned} \tag{2.12}$$

In (2.11), the subscript indicates the j^{th} unknown and $\mathbf{W}_j(u, v, z)$ is the same edge-based expansion function as that used for testing in (2.3); e.g. Galerkin's procedure is used. The function $\delta_a(i) \delta_a(j)$ is a product of two Kronecker functions and simply indicates that the boundary integral only contributes when both the test and source unknowns are on the aperture. The symbol N_v in (2.11) denotes the total number of unknowns or the free-edges space in the mesh.

Expressed in elliptic cylinder coordinates, (2.12) becomes the system of linear equations given by

$$\begin{aligned}
\sum_{j=1}^{N_v} E_j \left\{ \int_{V_i} \left[\frac{\nabla \times \mathbf{W}_j(u, v, z) \cdot \nabla \times \mathbf{W}_i(u, v, z)}{\mu_r} \right. \right. \\
\left. \left. - k_0^2 \epsilon_r \mathbf{W}_j(u, v, z) \cdot \mathbf{W}_i(u, v, z) \right] \beta^2 du dv dz \right. \\
\left. + k_0^2 \delta_a(i) \delta_a(j) \int_{S_j} \int_{S_i} \mathbf{W}_i(u', v', z') \cdot \mathbf{u}(v, z; v', z') \times \right. \\
\left. [\mathbf{u}(u, v, z) \times \mathbf{W}_j(u, v, z) \cdot \overline{\overline{G}}_{e2}(v, z; v', z')] \beta' \beta dv' dz' dvdz \right\} = f_i^{\text{int}}
\end{aligned} \tag{2.13}$$

where

$$\begin{aligned}
\beta(u, v, z) &= c(\cosh^2 u - \cos^2 v)^{1/2} \\
\beta'(u', v', z') &= c(\cosh^2 u' - \cos^2 v')^{1/2}
\end{aligned} \tag{2.14}$$

The FE-BI formulation can be written as a matrix equation

$$[\mathbf{A}]\{\mathbf{E}\} - k_0^2 [\mathbf{B}]\{\mathbf{E}\} + k_0^2 [\mathbf{C}]\{\mathbf{E}\} = \{f\}. \tag{2.15}$$

Here
where

Also

where

Also,

S_A, S_B

respect

bound,

matrix

elemen

matrix

differen

2.3. Vec

An

elemen

and the

associate

Here $A_{ij} = I_{st}^{(1)ij}$ and $B_{ij} = I_{st}^{(2)ij}$,
 where

$$\begin{aligned} I_{st}^{(1)ij} &= \int_{V_i} [\nabla \times \mathbf{W}_i \cdot \nabla \times \mathbf{W}_j] dV \\ I_{st}^{(2)ij} &= \int_{V_e} [\mathbf{W}_i \cdot \mathbf{W}_j] dV \end{aligned} \quad (2.16)$$

Also

$$C_{ij} = \int_{S_{A_i}} \left[\mathbf{W}_i \cdot \mathbf{u} \times \int_{S_{A_j}} \mathbf{u} \times \mathbf{W}_j \cdot \overline{\overline{\mathbf{G}_{e2}}} dS' \right] dS \quad (2.17)$$

where i and j represent the global test and source unknown numbers, respectively.

Also, V_i denotes the element volume associated with the test function i , while

S_{A_i}, S_{A_j} represent the surface that coincides with the aperture, of the i^{th}, j^{th} element,

respectively. The FEM matrix was formed by the matrix sum of [A] and [B], while the boundary integral matrix was formed by the sub-matrix [C]. The entries in the FEM matrix are identically zero unless both the test and source edges are within the same element and hence the FEM matrix is sparsely populated. However, the boundary integral matrix has entries that are nonzero even if the source and test edges are located in different elements. Hence, the boundary integral sub-matrix, [C], is fully populated.

2.3. Vector Weight Functions

An important factor in choosing the finite elements for gridding the cavity is the elements' suitability for satisfying both the mathematical requirements of the formulation and the physical features of the antenna system. Traditional node-based finite elements associate the degrees of freedom with the nodal fields. However, these functions have

pro

not

gene

with

short

design

remov

of th

[20]

struct

for ca

ellipt

E

ellipti

eight

orthog

associ

proven unsatisfactory for three-dimensional electromagnetics applications since they do not correctly represent the null space of the curl operator and hence spurious modes are generated [22-23]. Edge-based finite elements, whose degrees of freedom are associated with the edges of the finite element mesh, have been shown to be free of the above shortcomings. In the source-free solution region, edge-based finite elements can be designed to satisfy the divergence-free condition such that the spurious mode can be removed from the solutions. In addition, edge-based elements avoid explicit specification of the fields at corners where edge conditions may require a singularity. Jin and Volakis [20] presented edge-based brick elements that are convenient for rectangular-type structures and cavities. Later, Kempel and Volakis [9] designed the cylinder shell element for cavities embedded in a circular cylinder. For cavities recessed in an elliptic cylinder, elliptical shell elements are the natural choice.

Elliptical shell finite elements possess both geometrical fidelity and simplicity for elliptical-rectangular cavities. Figure 2.3 illustrates a typical shell element, which has eight nodes connected by twelve edges: four edges aligned along each of the three orthogonal directions of the elliptic cylinder coordinate system. Each element is associated with twelve vector shape functions given by

$$\begin{aligned}
W_{14} &= v \frac{\Delta_{v_l}(\rho_u - \rho_{u_b})(z - z_t)}{\Delta t h} = W_v(\rho_u, v, z; \rho_{u_b}, \cdot, z_t, +1) \\
W_{23} &= -v \frac{\Delta_{v_l}(\rho_u - \rho_{u_a})(z - z_t)}{\Delta t h} = W_v(\rho_u, v, z; \rho_{u_a}, \cdot, z_t, -1) \\
W_{58} &= -v \frac{\Delta_{v_l}(\rho_u - \rho_{u_b})(z - z_b)}{\Delta t h} = W_v(\rho_u, v, z; \rho_{u_b}, \cdot, z_t, -1) \\
W_{67} &= v \frac{\Delta_{v_l}(\rho_u - \rho_{u_a})(z - z_b)}{\Delta t h} = W_v(\rho_u, v, z; \rho_{u_a}, \cdot, z_b, +1) \\
W_{12} &= u \frac{\Delta_{u_b}(v - v_l)(z - z_t)}{\Delta \alpha h} = W_u(\rho_u, v, z; \cdot, v_l, z_t, +1) \\
W_{43} &= -u \frac{\Delta_{u_b}(v - v_r)(z - z_t)}{\Delta \alpha h} = W_u(\rho_u, v, z; \cdot, v_r, z_t, -1) \\
W_{56} &= -u \frac{\Delta_{u_b}(v - v_l)(z - z_b)}{\Delta \alpha h} = W_u(\rho_u, v, z; \cdot, v_l, z_b, -1) \\
W_{78} &= u \frac{\Delta_{u_b}(v - v_r)(z - z_b)}{\Delta \alpha h} = W_u(\rho_u, v, z; \cdot, v_r, z_b, +1) \\
W_{15} &= z \frac{(\rho_u - \rho_{u_b})(v - v_l)}{t \alpha} = W_z(\rho_u, v, z; \rho_{u_b}, v_l, \cdot, +1) \\
W_{26} &= -z \frac{(\rho_u - \rho_{u_a})(v - v_l)}{t \alpha} = W_z(\rho_u, v, z; \rho_{u_a}, v_l, \cdot, -1) \\
W_{48} &= -z \frac{(\rho_u - \rho_{u_b})(v - v_r)}{t \alpha} = W_z(\rho_u, v, z; \rho_{u_b}, v_r, \cdot, -1) \\
W_{37} &= z \frac{(\rho_u - \rho_{u_a})(v - v_r)}{t \alpha} = W_z(\rho_u, v, z; \rho_{u_a}, v_r, \cdot, +1)
\end{aligned} \tag{2.18}$$

where

$$\begin{aligned}
\rho_u &= \frac{c}{2} e^u \\
\alpha &= v_l - v_r \\
h &= z_t - z_b \\
t &= \rho_{u_b} - \rho_{u_a} = \frac{c}{2} (e^{u_b} - e^{u_a}) \\
\Delta &= (\cosh^2 u - \cos^2 v)^{1/2} \\
\Delta_{v_l} &= (\cosh^2 u - \cos^2 v_l)^{1/2} \\
\Delta_{u_b} &= (\cosh^2 u_b - \cos^2 v)^{1/2}
\end{aligned} \tag{2.19}$$

Also

2.3.

each

finit

wher

is di

a sp

circ

Rew

be w

Also, W_{ij} is associated with the edge defined by local nodes i and j as shown in Figure

2.3. As seen from (2.18), three fundamental vector weight functions, one associated with each coordinate axis, are required for the complete representation of the elliptical shell finite element. They are

$$\begin{aligned}
 \mathbf{W}_u(\rho_u, v, z; \cdot, \tilde{v}, \tilde{z}, \tilde{s}) &= \mathbf{u} \frac{\tilde{s} \Delta_{u_b} (v - \tilde{v})(z - \tilde{z})}{\Delta \alpha h} \\
 \mathbf{W}_v(\rho_u, v, z; \rho_{\tilde{u}}, \cdot, \tilde{z}, \tilde{s}) &= \mathbf{v} \frac{\tilde{s} \Delta_{v_l} (\rho_u - \rho_{\tilde{u}})(z - \tilde{z})}{\Delta t h} \\
 \mathbf{W}_z(\rho_u, v, z; \rho_{\tilde{u}}, \tilde{v}, \cdot, \tilde{s}) &= \mathbf{z} \frac{\tilde{s} (\rho_u - \rho_{\tilde{u}})(v - \tilde{v})}{t \alpha}
 \end{aligned} \tag{2.20}$$

where the element parameters ($u_a, u_b, v_r, v_l, z_b, z_l$) are shown Figure 2.3. Each local edge is distinguished by the parameters $\tilde{s}, \tilde{u}, \tilde{v}$ and \tilde{z} as given in (2.20). The circular cylinder is a special case of the elliptic cylinder, thus the elliptic cylinder can be reduced to the circular cylinder and then

$$\begin{aligned}
 \phi &\approx v \\
 \rho &\approx \frac{c}{2} e^u \\
 \Delta &= (\cosh^2 u - \cos^2 v)^{\frac{1}{2}} \approx \frac{e^u}{2} \\
 t &= \rho_{u_b} - \rho_{u_a} \approx \rho_b - \rho_a \\
 \alpha &= v_r - v_l \approx \phi_r - \phi_l
 \end{aligned} \tag{2.21}$$

Rewriting (2.20) with (2.21), the vector weight function for the circular cylinder [10] can be written as

The

Wh

that

dec

pre

2.4.

sho

the s

sub

from

are s

used

1997-98

$$\begin{aligned}
\mathbf{W}_{12}(\rho, \phi, z) &= \mathbf{W}_\rho(\rho, \phi, z; \cdot, \phi_r, z_t, +1), & \mathbf{W}_{43}(\rho, \phi, z) &= \mathbf{W}_\rho(\rho, \phi, z; \cdot, \phi_l, z_t, -1) \\
\mathbf{W}_{56}(\rho, \phi, z) &= \mathbf{W}_\rho(\rho, \phi, z; \cdot, \phi_r, z_b, -1), & \mathbf{W}_{87}(\rho, \phi, z) &= \mathbf{W}_\rho(\rho, \phi, z; \cdot, \phi_l, z_b, +1) \\
\mathbf{W}_{14}(\rho, \phi, z) &= \mathbf{W}_\phi(\rho, \phi, z; \rho_b, \cdot, z_t, +1), & \mathbf{W}_{23}(\rho, \phi, z) &= \mathbf{W}_\phi(\rho, \phi, z; \rho_a, \cdot, z_t, -1) \\
\mathbf{W}_{58}(\rho, \phi, z) &= \mathbf{W}_\phi(\rho, \phi, z; \rho_b, \cdot, z_b, -1), & \mathbf{W}_{67}(\rho, \phi, z) &= \mathbf{W}_\phi(\rho, \phi, z; \rho_a, \cdot, z_b, +1) \\
\mathbf{W}_{15}(\rho, \phi, z) &= \mathbf{W}_z(\rho, \phi, z; \rho_b, \phi_r, \cdot, +1), & \mathbf{W}_{26}(\rho, \phi, z) &= \mathbf{W}_z(\rho, \phi, z; \rho_a, \phi_r, \cdot, -1) \\
\mathbf{W}_{48}(\rho, \phi, z) &= \mathbf{W}_z(\rho, \phi, z; \rho_b, \phi_l, \cdot, -1), & \mathbf{W}_{37}(\rho, \phi, z) &= \mathbf{W}_z(\rho, \phi, z; \rho_a, \phi_l, \cdot, +1)
\end{aligned} \tag{2.22}$$

The three fundamental vector weight functions are

$$\begin{aligned}
\mathbf{W}_\rho(\rho, \phi, z; \bar{\rho}, \bar{\phi}, \bar{z}, \bar{s}) &= \rho \frac{\bar{s} \rho_b (\phi - \bar{\phi})(z - \bar{z})}{\alpha h \rho} \\
\mathbf{W}_\phi(\rho, \phi, z; \bar{\rho}, \bar{\phi}, \bar{z}, \bar{s}) &= \phi \frac{\bar{s}(\rho - \bar{\rho})(z - \bar{z})}{t h} \\
\mathbf{W}_z(\rho, \phi, z; \bar{\rho}, \bar{\phi}, \bar{z}, \bar{s}) &= z \frac{\bar{s}(\rho - \bar{\rho})(\phi - \bar{\phi})}{t \alpha}
\end{aligned} \tag{2.23}$$

Where the element parameters $(\rho_a, \rho_b, \phi_r, \phi_l, z_b, z_t)$ are shown in Figure 2.4. It is noted that as the radius of the cylinder becomes larger, the curvature of these elements decreases, resulting in weight functions that are functionally similar to the bricks presented by Jin and Volakis [20].

2.4. Finite Element Matrix

The volumetric mesh of the cavity is formed using the elliptic shell element shown in Figure 2.3 by meshing the cavity such that all the radius-dividing layers have the same foci as the surface ellipse, while the meshing along the z and v direction is subdivided uniformly by the fixed length of the geodesic path, which can be obtained from the perimeter divided by the total number of nodes in that direction. These elements are shell elements conformal to the surface of the elliptic cylinder. The exterior functions used to expand the aperture fields are similar to the volume elements. Applying the

ve

w

the

[C

for

for

fun

$I_{uu}^{(1)}$

$I_{u^i}^{(1)}$

$I_{\alpha}^{(1)}$

$I_{\xi}^{(1)} =$

$I_{\xi}^{(1)} =$

vector weight function defined by (2.18)-(2.20) in (2.13), the FE-BI formulation can be written as a matrix equation as shown in (2.15). The FEM matrix is composed by adding the matrices [A] and [B] while the boundary integral matrix is formed by the sub-matrix [C]. Carrying out the required vector operations and organizing each integral in separable form, as shown in (2.16), six combinations for $I_{st}^{(1)ij}$ and three combinations for $I_{st}^{(2)ij}$ remain. The two auxiliary functions are defined in (2.16). These elliptic auxiliary functions are

$$\begin{aligned}
I_{uu}^{(1)} &= \frac{c^2 \bar{s}_i \bar{s}_j}{\alpha^2 h} \int_{u_a}^{u_b} \int_{v_r}^{v_l} \Delta_{ub}^2 (v - \bar{v}_j)(v - \bar{v}_i) dudv + \frac{\bar{s}_i \bar{s}_j}{\alpha^2 h^2} \int_{u_a}^{u_b} \int_{v_r}^{v_l} \frac{\Delta_{ub}^2}{\Delta^2} dudv \cdot \int_{z_i}^{z_b} (z - \bar{z}_j)(z - \bar{z}_i) dz \\
I_{uv}^{(1)} &= -\frac{\bar{s}_i \bar{s}_j}{\alpha h^2} \int_{u_a}^{u_b} \int_{v_r}^{v_l} \frac{1}{\Delta^2} [(v - \bar{v}_j) \sin v \cdot \cos v \cdot \rho_u \frac{\Delta_{vl}}{\Delta_{ub}} \\
&\quad + (v - \bar{v}_j) \sin v \cos v \cosh u \sinh u \cdot \frac{(\rho_u - \rho_{\bar{u}_i})}{\Delta_{ub} \Delta_{vl}} \\
&\quad + \Delta_{ub} \Delta_{vl} \rho_u + \frac{(\rho_u - \rho_{\bar{u}_i}) \Delta_{ub}}{\Delta_{vl}} \cosh u \sin v \sinh u] dvdu \\
&\quad \cdot \int_{z_i}^{z_b} (z - \bar{z}_j)(z - \bar{z}_i) dz \\
I_{vv}^{(1)} &= \frac{c^2 \alpha \bar{s}_i \bar{s}_j}{t^2 h} \int_{u_a}^{u_b} \Delta_{vl}^2 (\rho_u - \rho_{\bar{u}_i})(\rho_u - \rho_{\bar{u}_j}) du \\
&\quad + \frac{\bar{s}_i \bar{s}_j}{t^2 h^2} \int_{u_a}^{u_b} \int_{v_r}^{v_l} \frac{1}{\Delta^2} [\Delta_{vl}^2 \rho_u^2 + \rho_u (\rho_u - \rho_{\bar{u}_i}) \cosh u \sinh u \\
&\quad + \rho_u (\rho_u - \rho_{\bar{u}_j}) \cosh u \sinh u + \frac{(\rho_u - \rho_{\bar{u}_i})(\rho_u - \rho_{\bar{u}_j}) \cosh^2 u \sinh^2 u}{\Delta_{vl}^2}] \\
&\quad \cdot \int_{z_i}^{z_b} (z - \bar{z}_j)(z - \bar{z}_i) dz \\
I_{vz}^{(1)} &= -\frac{c \bar{s}_i \bar{s}_j}{t^2} \int_{u_a}^{u_b} \Delta_{vl} (\rho_u - \rho_{\bar{u}_i})(\rho_u - \rho_{\bar{u}_j}) du \\
I_{zz}^{(1)} &= \frac{h \bar{s}_i \bar{s}_j}{\alpha^2 t^2} \int_{u_a}^{u_b} \int_{v_r}^{v_l} [\rho_u^2 (v - \bar{v}_j)(v - \bar{v}_i) + \rho_u^2 - \rho_u (\rho_{\bar{u}_i} + \rho_{\bar{u}_j}) + \rho_{\bar{u}_i} \rho_{\bar{u}_j}] dudv
\end{aligned} \tag{2.24}$$

and

cylind

circu

circu

circu

$$\begin{aligned}
I_{uu}^{(2)} &= \frac{c^2 \tilde{s}_i \tilde{s}_j}{\alpha^2 h^2} \int_{u_a}^{u_b} \int_{r_r}^{r_l} \Delta_{ub}^2 (v - \tilde{v}_i)(v - \tilde{v}_j) dv du \cdot \int_{z_t}^{z_b} (z - \tilde{z}_j)(z - \tilde{z}_i) dz \\
I_{vv}^{(2)} &= \frac{c^2 \alpha \tilde{s}_i \tilde{s}_j}{t^2 h^2} \int_{u_a}^{u_b} \Delta_{v_l}^2 (\rho_u - \rho_{\tilde{u}_i})(\rho_u - \rho_{\tilde{u}_j}) du \cdot \int_{z_t}^{z_b} (z - \tilde{z}_j)(z - \tilde{z}_i) dz \quad (2.25) \\
I_{zz}^{(2)} &= \frac{c^2 h \tilde{s}_i \tilde{s}_j}{t^2 \alpha^2} \int_{u_a}^{u_b} \Delta^2 (\rho_u - \rho_{\tilde{u}_i})(\rho_u - \rho_{\tilde{u}_j}) du \cdot \int_{r_r}^{r_l} (v - \tilde{v}_i)(v - \tilde{v}_j) dv
\end{aligned}$$

It should be noted that $I_{ab}^{(k)} = I_{ba}^{(k)}$, and therefore the FEM matrix is symmetric,

and only the upper or lower triangle of the FEM matrix needs to be stored. The cylindrical auxiliary function, which was developed from the FEM method for the circular cylinder [24], also can be obtained by reducing the elliptical auxiliary function in circular cylinder coordinates with the relations in (2.21). The auxiliary functions for the circular cylinder system are given by

$$\begin{aligned}
I_{\rho\rho}^{(1)} &= \frac{\tilde{s}_i \tilde{s}_j}{\alpha^2 h^2} \left[\rho_b^2 h \ln\left(\frac{\rho_b}{\rho_a}\right) \int_{\phi_l}^{\phi_r} (\phi - \tilde{\phi}_s)(\phi - \tilde{\phi}_t) d\phi + \frac{\alpha}{2} \left(\frac{\rho_b^2}{\rho_a^2} - 1\right) \int_{z_b}^{z_t} (z - \tilde{z}_i)(z - \tilde{z}_j) dz \right] \\
I_{\rho\phi}^{(1)} &= -\frac{\tilde{s}_i \tilde{s}_j}{th^2} \left[2\rho_b \ln\left(\frac{\rho_b}{\rho_a}\right) + \tilde{\rho}_t \left(1 - \frac{\rho_b}{\rho_a}\right) \right] \int_{z_b}^{z_t} (z - \tilde{z}_s)(z - \tilde{z}_t) dz \\
I_{\rho z}^{(1)} &= -\frac{\tilde{s}_i \tilde{s}_j \rho_b}{\alpha^2} \int_{\phi_l}^{\phi_r} (\phi - \tilde{\phi}_s)(\phi - \tilde{\phi}_t) d\phi \\
I_{\phi\phi}^{(1)} &= \frac{\alpha \tilde{s}_i \tilde{s}_j}{(th)^2} \left[h \left(\frac{1}{4} (\rho_b^4 - \rho_a^4) + \frac{1}{3} (\tilde{\rho}_s + \tilde{\rho}_t) (\rho_a^3 - \rho_b^3) + \frac{1}{2} \tilde{\rho}_s \tilde{\rho}_t (\rho_b^2 - \rho_a^2) \right) \right. \\
&\quad \left. + (2(\rho_b^2 - \rho_a^2) - 2t(\tilde{\rho}_s + \tilde{\rho}_t) + \tilde{\rho}_s \tilde{\rho}_t \ln\left(\frac{\rho_b}{\rho_a}\right)) \int_{z_b}^{z_t} (z - \tilde{z}_s)(z - \tilde{z}_t) dz \right] \\
I_{\phi z}^{(1)} &= -\frac{\tilde{s}_i \tilde{s}_j}{t^2} \int_{\rho_a}^{\rho_b} (\rho - \tilde{\rho}_s)(\rho - \tilde{\rho}_t) d\rho \\
I_{zz}^{(1)} &= \frac{h \tilde{s}_i \tilde{s}_j}{t^2 \alpha^2} \left[\alpha \left(\frac{1}{2} (\rho_b^2 - \rho_a^2) - t(\tilde{\rho}_s + \tilde{\rho}_t) + \tilde{\rho}_s \tilde{\rho}_t \ln\left(\frac{\rho_b}{\rho_a}\right) \right) \right. \\
&\quad \left. + \frac{1}{2} (\rho_b^2 - \rho_a^2) \int_{\phi_l}^{\phi_r} (\phi - \tilde{\phi}_s)(\phi - \tilde{\phi}_t) d\phi \right] \quad (2.26)
\end{aligned}$$

when

2.5.

Ident

oper

cavit

com

recta

for a

com

finit

lcm

$$\begin{aligned}
I_{\rho\rho}^{(2)} &= \frac{\tilde{s}_i \tilde{s}_j \rho_b^2}{\alpha^2 h^2} \ln\left(\frac{\rho_b}{\rho_a}\right) \int_{\phi_l}^{\phi_r} (\phi - \tilde{\phi}_s)(\phi - \tilde{\phi}_t) d\phi \int_{z_b}^{z_t} (z - \tilde{z}_s)(z - \tilde{z}_t) dz \\
I_{\phi\phi}^{(2)} &= \frac{\tilde{s}_i \tilde{s}_j \alpha}{t^2 h^2} \left[\frac{1}{4}(\rho_b^4 - \rho_a^4) + \frac{1}{3}(\tilde{\rho}_s + \tilde{\rho}_t)(\rho_a^3 - \rho_b^3) + \frac{1}{2}\tilde{\rho}_s \tilde{\rho}_t(\rho_b^2 - \rho_a^2) \right] \\
&\quad \times \int_{z_b}^{z_t} (z - \tilde{z}_s)(z - \tilde{z}_t) dz \\
I_{zz}^{(2)} &= \frac{\tilde{s}_i \tilde{s}_j h}{t^2 h^2} \left[\frac{1}{4}(\rho_b^4 - \rho_a^4) + \frac{1}{3}(\tilde{\rho}_s + \tilde{\rho}_t)(\rho_a^3 - \rho_b^3) + \frac{1}{2}\tilde{\rho}_s \tilde{\rho}_t(\rho_b^2 - \rho_a^2) \right] \quad (2.27) \\
&\quad \times \int_{\phi_l}^{\phi_r} (\phi - \tilde{\phi}_s)(\phi - \tilde{\phi}_t) d\phi
\end{aligned}$$

where each of the unevaluated integrals is of the form

$$\int_L^U (\xi - \tilde{\xi}_s)(\xi - \tilde{\xi}_t) d\xi = \frac{1}{2}(L^2 - U^2)(\tilde{\xi}_s + \tilde{\xi}_t) + \frac{1}{3}(U^3 - L^3) + \tilde{\xi}_s \tilde{\xi}_t (U - L) \quad (2.28)$$

2.5. Validation of Finite Element Formulation: The Closed Cavity

Finite elements for closed domains can be used for analyzing cavity resonances. Identification of these resonances is important for understanding and controlling the operation of many devices including microwave ovens. The eigenvalues for each empty cavity are computed by solving the generalized eigenvalue problem. The eigenvalues computed by the finite element method, as well as analytical results for the cylindrical-rectangular and planar-rectangular cavities, will be discussed in this section. A new result for an elliptical-rectangle cavity will be presented.

The rectangular cavity is a geometrically simple structure, but is widely used in complex microwave devices. A comparison between computed eigenvalues using the finite element method and analytical values is shown in Table 2.1. For a 2cm x 1cm x 1cm rectangular cavity, the average error percentage is less than 1.0% with 520

unkn

very

cavity

2.2%

such

unkno

with

good

Howe

result

determ

an ell

comp

vari

anten

sett

easil

Phys

great

whe

unknowns. Particularly, for the first two most important modes, the numerical results are very accurate.

In Table 2.2, the total unknowns for a 3cm x 3cm x 3cm quasi-circular shell cavity mounted on a cylinder of $\rho = 20$ cm are 450 and the average error percentage is 2.2%. To have more accurate results, the cavity was subdivided into finer finite elements such that the variation of electrical field inside the cavity can be represented by more unknown edges (e.g. degrees of freedom.) In Table 2.3, the error was improved to 1.3% with 1176 unknowns. It can be concluded that the eigenvalues can be computed with good accuracy and the accuracy is expected to increase with higher mesh density. However, the computational cost will rise and several negative trivial eigenvalues may result. Significantly, these results illustrate the fact that the FE method can be used to determine the resonance frequency of arbitrary shaped cavities.

The eigenvalues of an elliptic shell cavity mounted in three different locations of an elliptic cylinder with a major axis of $a=50$ cm and a minor axis of $b=20$ cm were computed and tabulated in Table 2.4. The eigenvalue for the lowest mode, TE₀₁₁, has less variation compared to other modes in those cases as one would expect. For the conformal antenna mounted in the elliptic cylinder starting from the elliptic angle of $\nu=0.02$ by setting the value of the initial angular parameter ν_0 to 0.02 in computation, it also can be easily observed that the eigenvalues have larger deviation from the other two cases. Physically, the cavity embedded in a region of rapidly changing curvature results in greater variation of field distribution inside the cavity while the field exhibits less change when the cavity is mounted in a region of surface with little curvature change.

ellip

con

For

ellip

$\rho=2$

resp

equi

The

surfa

How

on th

ellip

eigen

integ

The comparison of eigenvalues for a cavity mounted in different portions of an elliptic cylinder and the approximately equivalent circular cylinder is of course a major concern for the design of conformal antenna embedded on a curvature-varying surface. For a cavity (3cm x 3cm x 3cm) mounted in different positions, $v_0 = 0.02$, and $\pi/2$, of an elliptic cylinder with $a=50\text{cm}$, $b=20\text{cm}$ and the equivalent circular cylinder with radius of $\rho=20\text{cm}$ and $\rho=50\text{cm}$, the computational results are tabulated in Table 2.5 and 2.6, respectively. The average deviation of eigenvalues between the elliptic cavity and its equivalent circular shell cavity is 10.8% in Table 2.5 while it is 1.3% in Table 2.6. Therefore, the eigenvalues for the elliptic shell cavity mounted in the less curved elliptic surface can be approximately determined using its equivalent circular shell cavity. However, it is necessary to accurately model the elliptic shell cavity when it is embedded on the highly curved area.

From the discussion above it has been verified that the FE method using the new elliptic shell elements and its vector weight functions successfully compute the eigenvalues of the rectangular and shell cavities. It remains to develop the boundary integral and the dyadic Green's functions so that open problems may be examined.

Tab
ellip

Table 2.1 The eigenvalues for a rectangular cavity (2cm x 1cm x 1cm) represented in elliptic cylinder coordinates as $u=2$, $v=1$, $z=1$ (cm), utilizing 520 unknowns.

Eigenmod	Analytical	FEM	Error (%)
TE ₀₁₁	3.561	3.561	<0.01
TE ₁₀₁	3.561	3.561	<0.01
TM ₁₁₀	4.488	4.521	0.8
TE ₀₁₂	4.487	4.522	0.8
TM ₁₁₂	5.520	5.555	0.6

Tal
ellip

Table 2.2 The eigenvalues for a circular shell cavity (3cm x 3cm x 3cm) represented in elliptic cylinder coordinates as $u=v=z=3(\text{cm})$, utilizing 520 unknowns.

Eigenmode	Analytical	FEM	Error (%)
TE ₀₁₁	2.195	2.244	2.2
TE ₁₁₁	2.369	2.424	2.3
TM ₁₁₀	2.377	2.433	2.3
TM ₁₁₁	3.474	3.553	2.2
TE ₁₂₁	3.520	3.585	2.3

Table 2.3 The eigenvalues for a circular shell cavity (3cm x 3cm x 3cm) represented in elliptic cylinder coordinates as $u=v=z=3(\text{cm})$, utilizing 1176 unknowns.

Eigenmode	Analytical	FEM	Error (%)
TE ₀₁₁	2.195	2.224	1.3
TE ₁₁₁	2.369	2.399	1.2
TM ₁₁₀	2.377	2.409	1.3
TM ₁₁₁	3.474	3.520	1.3
TE ₁₂₁	3.520	3.546	1.2

Tabl
ellipt
 $v_0 = \pi$

Table 2.4 The eigenvalues for an elliptic shell cavity (3cm x 3cm x 3cm) mounted in an elliptic cylinder with a=50cm, b=20cm, starting from three different angles of $\nu_0=0.02$, $\nu_0=\pi/4$ and $\nu_0=\pi/2$ and utilizing 450 unknowns.

Eigenmode	$\nu_0=0.02$,	$\nu_0=\pi/4$	$\nu_0=\pi/2$
TE ₀₁₁	2.224	2.223	2.244
TE ₁₁₁	2.725	2.280	2.270
TM ₁₁₀	2.817	2.299	2.271
TM ₁₁₁	3.942	3.400	3.393
TE ₁₂₁	4.409	3.409	3.393

Tal
an d
app
unk

H

T

T

T

T

T

Table 2.5 Comparison of eigenvalues between a cavity (3cm x 3cm x 3cm) mounted in an elliptic cylinder with $a=50\text{cm}$, $b=20\text{cm}$, starting from the angle of $\nu_0=0.02$, and its approximate equivalent circular cylinder with radius of $\rho=20\text{ cm}$, utilizing 450 unknowns.

Eigenmode	Elliptic shell cavity, $\nu_0=0.02$,	Circular shell cavity, $\rho=20\text{ cm}$	Deviation (%)
TE ₀₁₁	2.224	2.244	0.90
TE ₁₁₁	2.725	2.424	11.0
TM ₁₁₀	2.817	2.433	13.6
TM ₁₁₁	3.942	3.553	9.9
TE ₁₂₁	4.409	3.585	18.7

Table 2.6 Comparison of eigenvalues between a cavity (3cm x 3cm x 3cm) mounted in an elliptic cylinder with a=50cm, b=20cm, starting from the angle of $\nu_0 = \pi/2$, and its approximate equivalent circular cylinder with radius of $\rho = 50$ cm, utilizing 450 unknowns.

Eigenmode	Elliptic shell cavity, $\nu_0 = \pi/2$	Circular shell cavity, $\rho = 50$ cm	Deviation (%)
TE ₀₁₁	2.244	2.245	<0.05
TE ₁₁₁	2.270	2.312	1.85
TM ₁₁₀	2.271	2.313	1.85
TM ₁₁₁	3.393	3.437	1.30
TE ₁₂₁	3.393	3.438	1.32

Figure

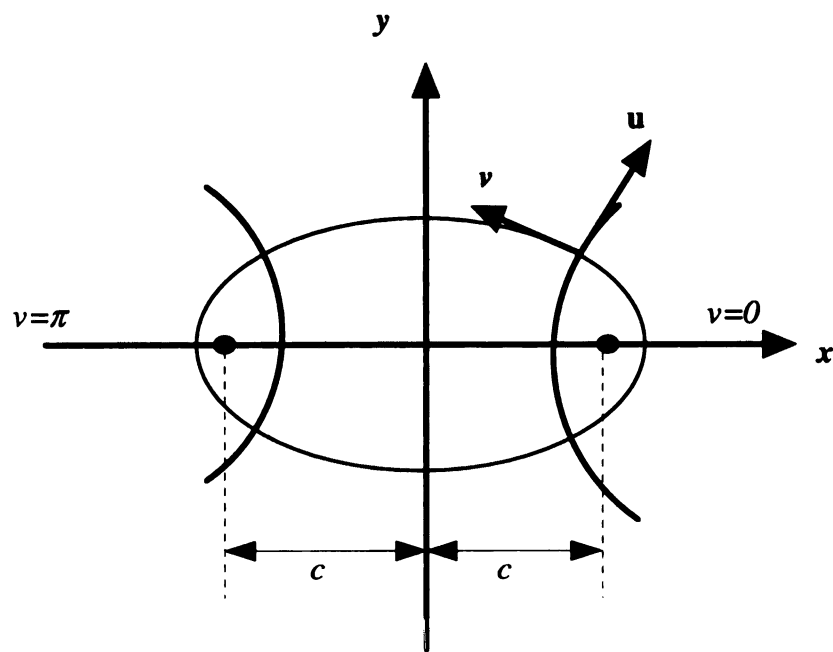


Figure 2.1 A cross-sectional view of the elliptic coordinate system

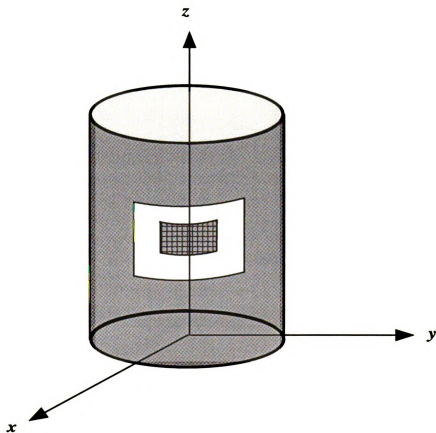


Figure 2.2 The geometry of the cavity-backed antenna embedded in a metallic elliptic cylinder.

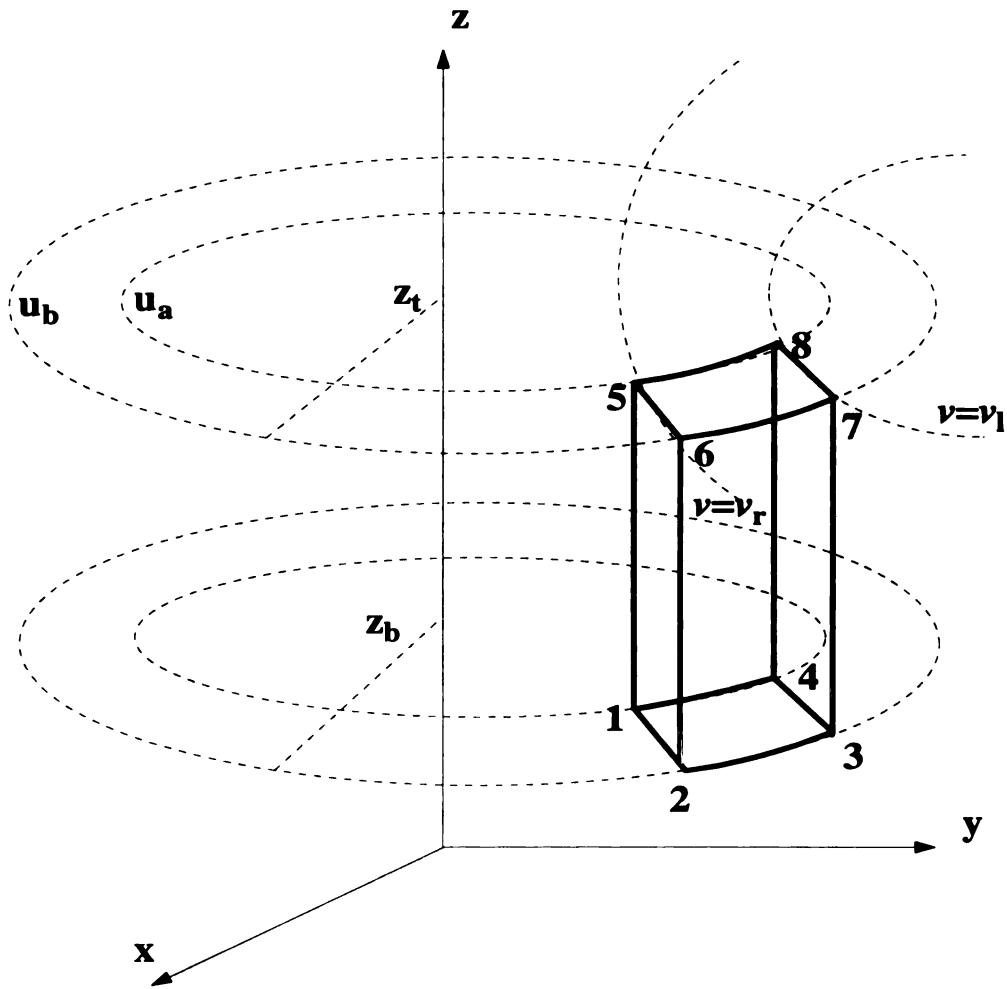


Figure 2.3 Geometry of an elliptic shell element. The numbers denote the local node numbering scheme for these elements.

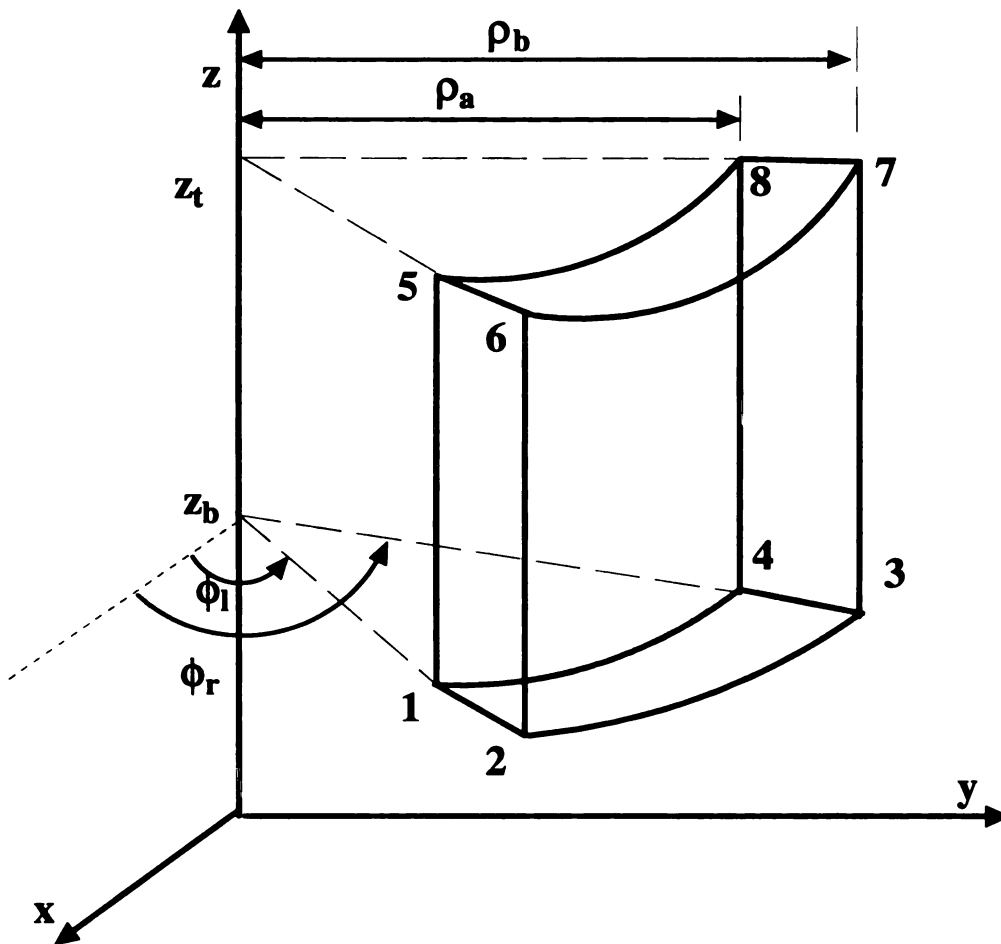


Figure 2.4 Geometry of a cylindrical shell element. The numbers denote the local node numbers for this element.

CHAPTER 3

DYADIC GREEN'S FUNCTION FOR ELLIPTIC CYLINDER

3.1 Introduction

In this chapter the surface dyadic Green's function for an infinitely long, perfectly conducting elliptic cylinder is derived [11]. In this approach, vector wave functions approximate for representing electromagnetic fields in the elliptic cylinder coordinate system are generated based on the elliptic cylinder scalar wave functions.

Eigenfunction expansion of the required field quantities is the first approach applied to find the dyadic Green's function necessary to describe on-surface interactions. In this chapter, the scalar wave equation is used and its eigenfunctions can be written in terms of separated angular and radial functions. The radial functions, which are the solution of the modified Mathieu's equation and finite at the origin, can be written as a series of Bessel functions. The angular functions, which are solutions of Mathieu's equation, are required to be periodic with respect to the angle of the elliptic cylinder so that the field represented by these functions is a single-valued function of position.

Since the dyadic Green's function developed by eigenfunction expansion is very difficult to evaluate numerically, an approximate asymptotic solution based on the Uniform Theory of Diffraction (UTD) has also been developed. In this, the surface fields attributed to a source on a smooth, perfectly conducting surface with arbitrary curvature are computed using a representation developed by Pathak and Wang [25]. Base on this development, an approximate asymptotic solution for the electromagnetic fields is found. These fields are induced by an infinitesimal magnetic current moment on the same surface. Hence, this solution of the surface magnetic field attributed to the aperture field

h

s

c

t

m

c

d

m

g

in

e

3

3

3

3

so

th

d

sh

co

in the year of

located on the same surface represents the dyadic Green's function. The superposition of such aperture field elements represents the total electric field in the aperture of a conformal antenna. This solution can be employed to calculate mutual coupling between two or more antenna elements. The volumetric cavity region behind the aperture is modeled using the finite element method. This hybrid approach allows the simulation of complex antennas with minimal computational effort. Such information is essential for designing conformal antenna arrays and for studying the electromagnetic compatibility of multiple antennas. In this UTD solution, the surface fields that propagate along each ray's geodesic path remain uniformly valid within the shadow boundary transition region including the immediate vicinity of the source. Again, it is noted that time convention $e^{j\omega t}$ is used through the whole dissertation.

3.2 Eigenfunction expansion method

3.2.1 Mathieu's Equation

Before the scalar wave equation in elliptic cylinder coordinates is introduced, the solutions for both Mathieu's and the modified Mathieu's equation must be developed. In the elliptic cylinder coordinate system, the set of coordinates used in this dissertation is designated by (u, v, z) . A cross-sectional view of a plane perpendicular to the z -axis is shown in Figure 2.1. The relations between rectangular coordinates and elliptic cylinder coordinates are given in (2.1).

Mathieu's equation can be written in the form

$$\frac{d^2 f(v)}{dv^2} + (a - 2q \cos 2v) f(v) = 0 \quad (3.1)$$

where a and q are parameters that are usually real number. Also, a is the eigenvalue of the system and it forms a denumerable set such that the corresponding angular functions is periodic functions of v

Since the angular solution for Mathieu's equation should be periodic over the elliptic cylinder, viz. $a = q = 0$, then the periodic solution of Mathieu's equation is constant, i.e., $f(v) = c$, where c is constant. This is the Mathieu function of order zero, associated with the eigenvalue $a = 0$. If $a \neq 0$ and $q = 0$, then

$$\frac{d^2 f(v)}{dv^2} + af(v) = 0 \quad (3.2)$$

The solution of (3.2) can be represented as

$$f_1(v) = \cos mv \quad \text{or} \quad f_2(v) = \sin mv \quad (3.3)$$

where $m = 1, 2, 3, \dots$

For the general solution of (3.1), where $a \neq 0$ and $q \neq 0$, the eigenfunction can be represented in series form as

$$f(v) = \sum_{j=0}^{\infty} A_j \cos(jv) + B_j \sin(jv) \quad (3.4)$$

where A_j and B_j are the expansion coefficients to be determined. Substituting (3.4) into (3.1), four different types of corresponding eigenfunctions are obtained:

$$\begin{aligned}
f_{2k \text{ even}}^{2m}(\nu) &= \sum_{k=0}^{\infty} A_{2k}^{2m} \cos(2k\nu), \quad m = 0, 1, 2, 3, \dots \\
f_{2k+1 \text{ even}}^{2m+1}(\nu) &= \sum_{k=0}^{\infty} A_{2k+1}^{2m+1} \cos(2k\nu), \quad m = 0, 1, 2, 3, \dots \\
f_{2k \text{ odd}}^{2m}(\nu) &= \sum_{k=0}^{\infty} B_{2k}^{2m} \sin(2k\nu), \quad m = 0, 1, 2, 3, \dots \\
f_{2k+1 \text{ odd}}^{2m+1}(\nu) &= \sum_{k=0}^{\infty} B_{2k+1}^{2m+1} \sin(2k\nu), \quad m = 0, 1, 2, 3, \dots
\end{aligned} \tag{3.5}$$

Here the subscripts *even* and *odd* represent the associated eigenfunction expanded in the base of *cosine* and *sine* functions, respectively. The equations above are four different types of Mathieu function, which are the solutions of Mathieu's equation associated with four different eigenvalues: $a = a_{2m}(q)$, $a = a_{2m+1}(q)$, $a = b_{2m}(q)$ and $a = b_{2m+1}(q)$.

These four types of solutions are isolated by odd and even functions and by their cyclic period of π or 2π .

For simplicity, the four solutions in (3.5) are combined as even and odd Mathieu functions. They are

$$S_{em}(\nu) = \sum_{n=0}^{\infty} D_n^m \cos(n\nu), \quad m = 0, 1, 2, 3, \dots \tag{3.6}$$

$$S_{om}(\nu) = \sum_{n=0}^{\infty} F_n^m \sin(n\nu), \quad m = 0, 1, 2, 3, \dots \tag{3.7}$$

where the summation is to be extended over even values of n if m is even and odd values of n if m is odd. $S_{em}(\nu)$ and $S_{om}(\nu)$ are also called the even and odd solutions of Mathieu's equation, respectively. The coefficients D_n^m and F_n^m are normalized, i.e.,

$$\sum_{n=0}^{\infty} D_n^m = 1, \quad \sum_{n=0}^{\infty} F_n^m = 1 \tag{3.8}$$

such that the following relationship between the even and odd solutions of Mathieu's equation is established

$$\frac{1}{\pi} \int_0^{2\pi} S_{em}^2(v) dv = \frac{1}{\pi} \int_0^{2\pi} S_{om}^2(v) dv = 1 \quad (3.9)$$

Using (3.9), it can be shown that $S_{em}(v)$ and $S_{om}(v)$ form a complete orthogonal set. The orthogonality relationships are

$$\begin{aligned} \int_0^{2\pi} S_{ei}(v) S_{ej}(v) dv &= \pi \sum_n (D_n^i)^2 \cdot (1 + \delta), & \text{for } i = j \\ \int_0^{2\pi} S_{ei}(v) S_{ej}(v) dv &= 0 & \text{for } i \neq j \\ \int_0^{2\pi} S_{oi}(v) S_{oj}(v) dv &= \pi \sum_n (F_n^i)^2, & \text{for } i = j \\ \int_0^{2\pi} S_{oi}(v) S_{oj}(v) dv &= 0 & \text{for } i \neq j \end{aligned} \quad (3.10)$$

where $\delta=1$ if $n=0$ and $\delta=0$ if $n \neq 0$.

3.2.2 Modified Mathieu's Equation

For convenience, Mathieu's equation can be rewritten as follows

$$\frac{d^2 f(v)}{dv^2} + (a - 2q \cos 2v) f(v) = 0 \quad (3.11)$$

The modified Mathieu's Equation can be obtained by replacing the variable v by the complex form jv [26]. Then (3.11) becomes

$$\frac{d^2 f(jv)}{dv^2} - (a - 2q \cosh 2v) f(jv) = 0 \quad (3.12)$$

which is the modified Mathieu's equation. The solutions of the modified Mathieu's equation are found by replacing the variable v with ju in the eigenfunction expressions

(3.5). The resulting expressions for the modified Mathieu functions are

$$\begin{aligned}
 f_{2k \text{ even}}^{2m}(ju) &= \sum_{k=0}^{\infty} A_{2k}^{2m} \cosh(2kv), & m = 0, 1, 2, 3, \dots \\
 f_{2k+1 \text{ even}}^{2m+1}(ju) &= \sum_{k=0}^{\infty} A_{2k+1}^{2m+1} \cosh(2k+1)v, & m = 0, 1, 2, 3, \dots \\
 f_{2k+1 \text{ odd}}^{2m+1}(ju) &= \sum_{k=0}^{\infty} B_{2k+1}^{2m+1} \sinh(2k+1)v, & m = 0, 1, 2, 3, \dots \\
 f_{2k+2 \text{ odd}}^{2m+2}(ju) &= \sum_{k=0}^{\infty} B_{2k+2}^{2m+2} \sinh(2k+2)v, & m = 0, 1, 2, 3, \dots
 \end{aligned} \tag{3.13}$$

Replacing the parameter q and v in (3.12) with $\frac{c_0^2 k_\rho^2}{4}$ and u , respectively, then the

quantity $2q \cosh 2v$ becomes by $(c_0 k_\rho \cosh u)^2 - \frac{c_0^2 k_\rho^2}{2}$, giving

$$\frac{d^2 f(u)}{du^2} + (c_0^2 k_\rho^2 \cosh^2 u - b) f(u) = 0 \tag{3.14}$$

where $b = a + \frac{c_0^2 k_\rho^2}{2}$. The solutions of (3.14), which are equivalent to (3.13), now can be

written and expanded in terms of a series of Bessel functions as [27]

$$\begin{aligned}
 R_{emk\rho}^1(u) &= \sqrt{\frac{\pi}{2}} \sum_{n=0}^{\infty} (j)^{m-n} A_n^m J_n(c_0 k_\rho \cosh u) \\
 R_{emk\rho}^2(u) &= \sqrt{\frac{\pi}{2}} \sum_{n=0}^{\infty} (j)^{m-n} A_n^m Y_n(c_0 k_\rho \cosh u) \\
 R_{omk\rho}^1(u) &= \sqrt{\frac{\pi}{2}} \tanh u \sum_{n=0}^{\infty} (j)^{n-m} n B_n^m J_n(c_0 k_\rho \cosh u) \\
 R_{omk\rho}^2(u) &= \sqrt{\frac{\pi}{2}} \tanh u \sum_{n=0}^{\infty} (j)^{n-m} n B_n^m Y_n(c_0 k_\rho \cosh u)
 \end{aligned} \tag{3.15}$$

where superscript 1 represent function $J_n(z)$, which is the n^{th} order Bessel function of first type, while 2 denotes function Y_n , which is the n^{th} order Bessel function of second type. Also, the summation is to be extended over even values of n if m is even and odd values of n if m is odd. It is noted that for these four eigenfunctions, each is associated with its own eigenvalue in the modified Mathieu's equation. For simplicity these four radial eigenfunctions are combined as follows

$$\begin{aligned} R_{emk\rho}(u) &= \sqrt{\frac{\pi}{2}} \sum_{n=0}^{\infty} (j)^{m-n} D_n^m J_n(c_0 k_\rho \cosh u) \\ R_{omk\rho}(u) &= \sqrt{\frac{\pi}{2}} \tanh u \sum_{n=0}^{\infty} (j)^{n-m} F_n^m J_n(c_0 k_\rho \cosh u) \end{aligned} \quad (3.16)$$

3.2.3 Vector Wave Functions In An Elliptic Cylinder Coordinate System

The scalar wave equation in an elliptic cylinder coordinate system can be written in the form

$$\frac{1}{\beta} \left(\frac{\partial^2 \psi}{\partial u^2} + \frac{\partial^2 \psi}{\partial v^2} \right) + \frac{\partial^2 \psi}{\partial z^2} + (k_\rho^2 + k_z^2) \psi = 0 \quad (3.17)$$

where $\beta = c(\cosh^2 u - \cos^2 v)^{\frac{1}{2}}$

The variables u , v and z are the radial, angular and axial coordinates in the elliptic cylinder coordinate system, respectively. The parameter c is again the distance between the foci of the ellipse. Assuming that $f = f_1(\cosh u) f_2(\cos v)$ is the solution of (3.17) and using it in (3.17), then the following two equations result

$$\frac{d^2 f_1(u)}{du^2} + (c^2 k_\rho^2 \cosh^2 u - b) f_1(u) = 0 \quad (3.18)$$

$$\frac{d^2 f_2(v)}{dv^2} + (b - c^2 k_\rho^2 \cos^2 v) f_2(v) = 0 \quad (3.19)$$

Here (3.18) is the modified Mathieu's equation, while (3.19) is Mathieu's equation. The eigenvalues b form a denumerable set such that the corresponding angular functions is periodic functions of v , and thus a single-valued function of position for the electromagnetic fields can be described. Because the wave functions of the elliptic cylinder can be written as

$$\psi = f(u, v) e^{-jk_z z} = f_1(u) f_2(v) e^{-jk_z z} \quad (3.20)$$

Thus, by applying the solutions of Mathieu's and the modified Mathieu's equation, which have been derived in sections 3.2.1 and 3.2.2, into (3.20), the resulting wave function is given by

$$\psi = S_{e_{omk_\rho}}(v) R_{e_{omk_\rho}}(u) e^{-jk_z z} \quad (3.21)$$

where

$$\begin{aligned} R_{emk_\rho}(u) S_{emk_\rho}(v) &= \sqrt{\frac{\pi}{2}} \sum_{n=0}^{\infty} (j)^{n-m} D_n^m \cos(nv) J_n(ck_\rho \cosh u) \\ R_{omk_\rho}(u) S_{omk_\rho}(v) &= \sqrt{\frac{\pi}{2}} \sum_{n=0}^{\infty} (j)^{n-m} F_n^m \sin(nv) J_n(ck_\rho \cosh u) \end{aligned} \quad (3.22)$$

Equation (3.22) is given by Stratton [28] and can be used to represent the standing wave function inside the elliptic cylinder, while the outgoing wave which is traveling outward from the cylinder can be represented in the form of Hankel functions of the second kind as follows

Sim
con

wh

M

N

T

$$\begin{aligned}
R_{emk_\rho}^{(2)}(u)S_{emk_\rho}(v) &= \sqrt{\frac{\pi}{2}} \sum_{n=0}^{\infty} (j)^{n-m} D_n^m \cos nv H_n^{(2)}(ck_\rho \cosh u) \\
R_{omk_\rho}^{(2)}(u)S_{omk_\rho}(v) &= \sqrt{\frac{\pi}{2}} \sum_{n=0}^{\infty} (j)^{n-m} F_n^m \sin nv H_n^{(2)}(ck_\rho \cosh u)
\end{aligned} \tag{3.23}$$

Since ψ is the solution of the scalar wave equation in elliptic cylindrical coordinates, the corresponding vector wave functions are defined by

$$\begin{aligned}
\mathbf{M}_{e_{omk_\rho}}(-k_z) &= \nabla \times \psi \\
\mathbf{N}_{e_{omk_\rho}}(-k_z) &= \frac{1}{\kappa} \nabla \times \nabla \times \psi
\end{aligned} \tag{3.24}$$

where $\kappa^2 = k_\rho^2 + k_z^2$. Then these two vector wave functions are

$$\mathbf{M}_{e_{omk_\rho}}(-k_z) = \frac{1}{\beta} \left[R_{e_{omk_\rho}} \frac{\partial S_{e_{omk_\rho}}}{\partial v} \mathbf{u} - S_{e_{omk_\rho}} \frac{\partial R_{e_{omk_\rho}}}{\partial u} \mathbf{v} \right] e^{-jk_z z} \tag{3.25}$$

$$\begin{aligned}
\mathbf{N}_{e_{omk_\rho}}(-k_z) &= \frac{1}{k\beta} \left[-jk_z S_{e_{omk_\rho}} \frac{\partial R_{e_{omk_\rho}}}{\partial u} \mathbf{u} - jk_z R_{e_{omk_\rho}} \frac{\partial S_{e_{omk_\rho}}}{\partial v} \mathbf{v} \right. \\
&\quad \left. + \beta k_\rho^2 R_{e_{omk_\rho}} S_{e_{omk_\rho}} \mathbf{z} \right] e^{-jk_z z}
\end{aligned} \tag{3.26}$$

The orthogonal properties of these functions are stated by the following equation [11]

$$\iiint \mathbf{M}_{e_{omk_\rho}}(-k_z) \cdot \mathbf{N}_{e_{om'k_\rho}}(k'_z) dV = 0 \tag{3.27}$$

$$\begin{aligned}
&\iiint \mathbf{M}_{e_{omk_\rho}}(-k_z) \cdot \mathbf{M}_{e_{om'k_\rho}}(k'_z) dV \\
&= \begin{cases} 0 & m \neq m' \\ \pi^2 k_\rho I_{e_{omk_\rho}} \delta(k_z - k'_z) \delta(k_\rho - k'_\rho) & m = m' \end{cases}
\end{aligned} \tag{3.28}$$

who

3.2

eq

an

ex

B

B

e

a

$$\begin{aligned} & \iiint \mathbf{N}_{e_{omk\rho}}(-k_z) \cdot \mathbf{N}_{e_{om'k\rho}}(k_z) dV \\ & = \left\{ \begin{array}{ll} 0 & m \neq m' \\ \pi^2 k_\rho I_{e_{omk\rho}} \delta(k_z - k_z') \delta(k_\rho - k_\rho') & m = m' \end{array} \right\} \end{aligned} \quad (3.29)$$

where

$$I_{emk\rho} = \pi \sum_{n=0}^{\infty} (1 + \delta_0) (D_n^m)^2, \quad I_{omk\rho} = \sum_{n=0}^{\infty} (F_n^m)^2$$

3.2.4. The Free-Space Dyadic Green's function

The free-space magnetic dyadic Green's function satisfies the dyadic differential equation [11]

$$\nabla \times \nabla \times \bar{\bar{G}}_{m0}(\mathbf{R}, \mathbf{R}') - k^2 \bar{\bar{G}}_{m0}(\mathbf{R}, \mathbf{R}') = \nabla \times [\bar{\bar{I}} \delta(\mathbf{R}, \mathbf{R}')] \quad (3.30)$$

and the radiation condition at infinity. Here $\bar{\bar{I}}$ is called an idem factor, and its explicit expression is

$$\bar{\bar{I}} = \sum_i \mathbf{x}_i \mathbf{x}_i \quad (3.31)$$

By using the eigenfunction expansion, the right hand side of (3.30) can be written as

$$\nabla \times [\bar{\bar{I}} \delta(\mathbf{R} - \mathbf{R}')] = \int_0^\infty dk_\rho \int_{-\infty}^\infty dk_z \sum_{m=1}^\infty [A_{e_{omk\rho}}(-k_z) \mathbf{N}_{e_{omk\rho}}(-k_z) + B_{e_{omk\rho}}(-k_z) \mathbf{M}_{e_{omk\rho}}(-k_z)] \quad (3.32)$$

By taking the anterior scalar product of (3.32) with $\mathbf{N}_{e_{omk\rho}}(k_z)$ and integrating the equation over all space, as a result of the orthogonal relationships given in (3.27), (3.28) and (3.29), the following relationships are obtained

1

wh

so

giv

N

ei

S

T

$$\mathbf{A}_{e_{omk\rho}}(k_z) = \frac{\kappa}{\pi^2 k_\rho I_{e_{omk\rho}}} \mathbf{M}'_{e_{omk\rho}}(k_z) \quad (3.33)$$

$$\mathbf{B}_{e_{omk\rho}}(k_z) = \frac{\kappa}{\pi^2 k_\rho I_{e_{omk\rho}}} \mathbf{N}'_{e_{omk\rho}}(k_z) \quad (3.34)$$

where $\kappa^2 = k_\rho^2 + k_z^2$ and the superscript in $\mathbf{M}'_{e_{omk\rho}}(k_z)$ and $\mathbf{N}'_{e_{omk\rho}}(k_z)$ represents the

source field point. Hence the continuous eigenfunction expansion of $\nabla \times [\bar{I} \delta(\mathbf{R}, \mathbf{R}')]$ is

given by

$$\begin{aligned} \nabla \times [\bar{I} \delta(\mathbf{R}, \mathbf{R}')] = & \int_0^\infty dk_\rho \int_{-\infty}^\infty dk_z \sum_{m=1}^\infty \frac{\kappa}{\pi^2 k_\rho I_{e_{omk\rho}}} \{ \mathbf{N}_{e_{omk\rho}}(-k_z) \mathbf{M}'_{e_{omk\rho}}(k_z) \\ & + \mathbf{M}_{e_{omk\rho}}(-k_z) \mathbf{N}'_{e_{omk\rho}}(k_z) \} \end{aligned} \quad (3.35)$$

Now, $\bar{G}_{m0}(\mathbf{R}, \mathbf{R}')$ in the left hand side of (3.30) may be expanded in terms of eigenfunction as

$$\begin{aligned} \bar{G}_{m0}(\mathbf{R}, \mathbf{R}') = & \int_0^\infty dk_\rho \int_{-\infty}^\infty dk_z \sum_{m=1}^\infty [a(k_z) \mathbf{N}_{e_{omk\rho}}(-k_z) \mathbf{M}'_{e_{omk\rho}}(k_z) \\ & + b(k_z) \mathbf{M}_{e_{omk\rho}}(-k_z) \mathbf{N}'_{e_{omk\rho}}(k_z)] \end{aligned} \quad (3.36)$$

Substituting (3.35) and (3.36) into (3.30), the coefficients are determined as

$$a(k_z) = b(k_z) = \frac{\kappa}{\pi^2 k_\rho I_{e_{omk\rho}} (\kappa^2 - k^2)} \quad (3.37)$$

Thus the expression for $\bar{G}_{m0}(\mathbf{R}, \mathbf{R}')$ can be written in the form

$$\begin{aligned} \bar{G}_{m0}(\mathbf{R}, \mathbf{R}') = & \int_0^{\infty} dk_{\rho} \int_{-\infty}^{\infty} dk_z \sum_{m=1}^{\infty} \frac{\kappa}{\pi^2 k_{\rho} I_{e_{omk\rho}}(\kappa^2 - k^2)} [N_{e_{omk\rho}}(-k_z) M'_{e_{omk\rho}}(k_z) \\ & + M_{e_{omk\rho}}(-k_z) N'_{e_{omk\rho}}(k_z)] \end{aligned} \quad (3.38)$$

To simplify the expression in (3.38), Let

$$I = \int_0^{\infty} k_{\rho} \sum_{m=1}^{\infty} \frac{\kappa}{\pi^2 k_{\rho} I_{e_{omk\rho}}(\kappa^2 - k^2)} [N_{e_{omk\rho}}(-k_z) M'_{e_{omk\rho}}(k_z) + M_{e_{omk\rho}}(-k_z) N'_{e_{omk\rho}}(k_z)] \quad (3.39)$$

and

$$\begin{aligned} N_{e_{omk\rho}}(-k_z) M'_{e_{omk\rho}}(k_z) &= \bar{T}^{(1)} [J_n(ck_{\rho} \cosh u) J_n(ck_{\rho} \cosh u')] \\ M_{e_{omk\rho}}(-k_z) N'_{e_{omk\rho}}(k_z) &= \bar{T}^{(2)} [J_n(ck_{\rho} \cosh u) J_n(ck_{\rho} \cosh u')] \end{aligned} \quad (3.40)$$

Then (3.39) becomes

$$\begin{aligned} I &= \int_0^{\infty} dk_{\rho} \sum_{m=1}^{\infty} \frac{\kappa}{\pi^2 k_{\rho} I_{e_{omk\rho}}(\kappa^2 - k^2)} [\bar{T}^{(1)} + \bar{T}^{(2)}] \\ &= I^{(1)} + I^{(2)} \end{aligned} \quad (3.41)$$

where

$$\begin{aligned} I^{(1)} &= \int_0^{\infty} dk_{\rho} \sum_{m=1}^{\infty} \frac{\kappa}{\pi^2 k_{\rho} I_{e_{omk\rho}}(\kappa^2 - k^2)} \bar{T}^{(1)} \\ I^{(2)} &= \int_0^{\infty} dk_{\rho} \sum_{m=1}^{\infty} \frac{\kappa}{\pi^2 k_{\rho} I_{e_{omk\rho}}(\kappa^2 - k^2)} \bar{T}^{(2)} \end{aligned} \quad (3.42)$$

1829-1830

1830-1831

For field solutions satisfying the vector wave equation in the elliptic cylinder coordinate system and for observation within the elliptic cylinder, i.e., $u < u'$, the first part of (3.39) can be rewritten as

$$I^{(1)} = \int_0^{\infty} k_{\rho} \sum_m \frac{\kappa}{\pi^2 k_{\rho} I_{e_{om} k_{\rho}} (\kappa^2 - k^2)} \{ \tilde{T}^{(1)} [J_n(ck_{\rho} \cosh u) H_n^{(1)}(ck_{\rho} \cosh u')] \} \\ + \int_0^{\infty} k_{\rho} \sum_m \frac{\kappa}{\pi^2 k_{\rho} I_{e_{om} k_{\rho}} (\kappa^2 - k^2)} \{ \tilde{T}^{(1)} [J_n(ck_{\rho} \cosh u) H_n^{(2)}(ck_{\rho} \cosh u')] \} \quad (3.43)$$

Here the Bessel function in (3.40) for the source point has been replaced by the combination of a Hankel function of first kind and second kind, while the Bessel function for the field point was retained to represent the standing wave inside the elliptic cylinder.

Replacing the variable k_{ρ} with $-k_{\rho}$ in the first term of (3.43) and using the following relationships

$$H_n^{(1)}(ck_{\rho} e^{-j\pi} \cosh u') = -e^{-jn\pi} H_n^{(2)}(ck_{\rho} \cosh u') \\ J_n(ck_{\rho} e^{-j\pi} \cosh u) = e^{jn\pi} J_n(ck_{\rho} \cosh u) \quad (3.44)$$

then (3.43) becomes a principal-value integral as follows

$$I^{(1)} = \int_{-\infty}^{\infty} dk_{\rho} \frac{\kappa \tilde{T}^{(1)} [J_n(ck_{\rho} \cosh u) H_n^{(2)}(ck_{\rho} \cosh u')]}{2\pi^2 k_{\rho} I_{e_{om} k_{\rho}} (k_{\rho} + (k^2 - k_z^2)^{1/2})(k_{\rho} - (k^2 - k_z^2)^{1/2})} \quad (3.45)$$

where $J_n(ck_{\rho} \cosh u)$ represents standing wave inside the elliptic cylinder.

The principal-value integral in (3.45) now can be converted to a contour integral along the contour shown in Figure 3.1. Here $e^{-jk_{\rho} r}$ is used to represent outward propagating plane wave in the $e^{j\omega t}$ time convention. Initially the medium is assumed to have a small loss so that the pole at $k_{\rho} = -(k^2 - k_z^2)^{1/2} = x_0 - jy_0$, $y_0 > 0$, lies above the contour and

yang diintegrasikan ke dalam

the pole at $k_\rho = (k^2 - k_z^2)^{1/2} = -x_0 + jy_0$ lies below the contour as shown in Figure. 3.1.

When $k_\rho r$ is very large the Bessel functions have the following asymptotic behavior

$$\begin{aligned} H_n^2(k_\rho r) &\approx \frac{2}{\pi k_\rho r} j^{n+\frac{1}{2}} e^{-jk_\rho r} \\ J_n(k_\rho r) &\approx \sqrt{\frac{2}{\pi k_\rho r}} \cos(k_\rho r - \frac{\pi}{4} - \frac{n\pi}{2}) \end{aligned} \quad (3.46)$$

Consequently, in the lower half of the complex k_ρ plane the product inside the integral of (3.45) becomes exponentially small for large $k_\rho r$. The contour can be closed by a semicircle in the lower half plane, and, when the radius of this circle approaches infinity, the contribution from this part of the contour is negligible. By applying residue theory to evaluate the contribution from pole at $k_\rho = -(k^2 - k_z^2)^{1/2}$, (3.45) becomes

$$\begin{aligned} I^{(1)} &= \int_{-\infty}^{\infty} dk_\rho \frac{\kappa \tilde{T}^{(1)} [J_n(ck_\rho \cosh u) H_n^{(2)}(ck_\rho \cosh u)]}{2\pi^2 k_\rho I_{e, m k_\rho} (k_\rho + (k^2 - k_z^2)^{1/2})(k_\rho - (k^2 - k_z^2)^{1/2})} \\ &= -2\pi j \cdot \text{Residue} \Big|_{k_\rho = -(k^2 - k_z^2)^{1/2}, \kappa = (k^2 + k_z^2)^{1/2} = k} \\ &= \frac{-jk \tilde{T} [J_n(c\eta \cosh u) H_n^{(2)}(c\eta \cosh u)]}{2\pi \eta^2 I_{e, m \eta}} \\ &= \frac{-jk}{2\pi \eta^2 I_{e, m \eta}} \mathbf{N}(-k_z) \mathbf{M}^{(2)'}(k_z) \end{aligned} \quad (3.47)$$

where $\eta = (k^2 - k_z^2)^{\frac{1}{2}}$.

Using the same procedure as above for $I^{(2)}$ in (3.41), gives

$$I^{(2)} = \frac{-jk}{2\pi \eta^2 I_{e, m \eta}} \mathbf{M}(-k_z) \mathbf{N}^{(2)'}(k_z) \quad (3.48)$$

Combining (3.47) and (3.48), then I is expressed as

$$\begin{aligned}
I &= \int_0^{\infty} dk_{\rho} \sum_{m=1}^{\infty} \frac{\kappa}{\pi^2 k_{\rho} I_{e_{omk\rho}} (\kappa^2 - k^2)} [\mathbf{N}(-k_z) \mathbf{M}^{(2)'}(k_z) + \mathbf{M}(-k_z) \mathbf{N}^{(2)'}(k_z)] \\
&= \frac{-jk}{2\pi\eta^2 I_{e_{om\eta}}} [\mathbf{N}(-k_z) \mathbf{M}^{(2)'}(k_z) + \mathbf{M}(-k_z) \mathbf{N}^{(2)'}(k_z)] \quad \text{for } u < u'
\end{aligned} \tag{3.49}$$

For simplicity, the subscripts attached to \mathbf{M} and \mathbf{N} are omitted here. Consequently,

(3.36) becomes

$$\bar{G}_{m0}(\mathbf{R}, \mathbf{R}') = \int_{-\infty}^{\infty} dk_z \frac{-jk}{2\pi\eta^2 I_{e_{om\eta}}} [\mathbf{N}(-k_z) \mathbf{M}^{(2)'}(k_z) + \mathbf{M}(-k_z) \mathbf{N}^{(2)'}(k_z)] \quad \text{for } u < u'$$

(3.50)

For $u > u'$, a Hankel function of the first and second kind are used to represent the traveling waves. Then the first part of (3.39) can be written as

$$\begin{aligned}
I^{(1)} &= \int_0^{\infty} k_{\rho} \sum_{m=1}^{\infty} \frac{\kappa}{\pi^2 k_{\rho} I_{e_{omk\rho}} (\kappa^2 - k^2)} \{ \tilde{T}^{(1)} [\frac{1}{2} H_n^1(ck_{\rho} \cosh u) J_n(ck_{\rho} \cosh u')] \} \\
&+ \int_0^{\infty} k_{\rho} \sum_{m=1}^{\infty} \frac{\kappa}{\pi^2 k_{\rho} I_{e_{omk\rho}} (\kappa^2 - k^2)} \{ \tilde{T}^{(1)} [\frac{1}{2} H_n^2(ck_{\rho} \cosh u) J_n(ck_{\rho} \cosh u')] \}
\end{aligned} \tag{3.51}$$

Likewise, (3.51) can be transferred to a principal integral by a change of variables, and then assuming the medium the wave is traveling has a small loss. The evaluation of the principal integral can proceed as before using the residue theorem to give a closed form for that integral with respect to k_{ρ} . The same procedure is applied to $I^{(2)}$ in (3.41) and then combined. Hence (3.39) for $u > u'$ becomes

$$\begin{aligned}
I &= \int_0^{\infty} k_{\rho} \sum_{m=1}^{\infty} \frac{\kappa}{\pi^2 k_{\rho} I_{e_{omk\rho}} (\kappa^2 - k^2)} [\mathbf{N}^{(2)}(-k_z) \mathbf{M}'(k_z) + \mathbf{M}^{(2)}(-k_z) \mathbf{N}^{(1)}(k_z)] \\
&= \frac{-jk}{2\pi\eta^2 I_{e_{om\eta}}} [\mathbf{N}^{(2)}(-k_z) \mathbf{M}'(k_z) + \mathbf{M}^{(2)}(-k_z) \mathbf{N}'(k_z)]
\end{aligned} \tag{3.52}$$

Th

\bar{G}_m

Cor

vec

\bar{G}_m

wh

defi

disc

wh

field

follo

Thus,

$$\overline{\overline{G}}_{m0}(\mathbf{R}, \mathbf{R}') = \int_{-\infty}^{\infty} dk_z \sum_{m=1}^{\infty} \frac{-jk}{2\pi\eta^2 I_{e,m\eta}} [\mathbf{N}^{(2)}(-k_z)\mathbf{M}'(k_z) + \mathbf{M}^{(2)}(-k_z)\mathbf{N}'(k_z)] \quad \text{for } u > u' \quad (3.53)$$

Consequently, the free-space magnetic dyadic Green's function, which satisfies the vector wave equation in an elliptic cylinder coordinate system, can be expressed as

$$\overline{\overline{G}}_{m0}(\mathbf{R}, \mathbf{R}') = \int_{-\infty}^{\infty} dk_z \sum_{m=1}^{\infty} \frac{-jk}{2\pi\eta^2 I_{e,m\eta}} \begin{cases} [\mathbf{N}(-k_z)\mathbf{M}^{(2)'}(k_z) + \mathbf{M}(-k_z)\mathbf{N}^{(2)'}(k_z)] & \text{for } u < u' \\ [\mathbf{N}^{(2)}(-k_z)\mathbf{M}'(k_z) + \mathbf{M}^{(2)}(-k_z)\mathbf{N}'(k_z)] & \text{for } u > u' \end{cases} \quad (3.54)$$

where the superscript (2) attached to $\mathbf{N}^{(2)}$ and $\mathbf{M}^{(2)}$ means that these functions are now defined with respect to the Hankel function of the second kind. The function $\overline{\overline{G}}_{m0}$ is discontinuous at $u = u'$. The expression for $\overline{\overline{G}}_{e0}$ can be obtained from $\overline{\overline{G}}_{m0}$ as

$$\overline{\overline{G}}_{e0}(\mathbf{R}, \mathbf{R}') = \frac{1}{k^2} [-\mathbf{uu}\delta(\mathbf{R} - \mathbf{R}') + (\nabla \times \overline{\overline{G}}_{m0}^+)U(u - u') + (\nabla \times \overline{\overline{G}}_{m0}^-)U(u' - u)] \quad (3.55)$$

where U is the unit step function and the superscript + and - attached to $\overline{\overline{G}}_{m0}$ denote the field outside and inside the elliptic cylinder, respectively. Inserting (3.54) into (3.55), the following expression for $\overline{\overline{G}}_{e0}$ is obtained

$$\overline{\overline{G}}_{e0}(\mathbf{R}, \mathbf{R}') = \frac{1}{k^2} [-\mathbf{uu}\delta(\mathbf{R} - \mathbf{R}')] - \frac{j}{2\pi} \int_{-\infty}^{\infty} dk_z \sum_{m=1}^{\infty} \frac{1}{\eta^2 I_{e,m\eta}} \begin{cases} [\mathbf{M}(-k_z)\mathbf{M}^{(2)'}(k_z) + \mathbf{N}(-k_z)\mathbf{N}^{(2)'}(k_z)] & \text{for } u < u' \\ [\mathbf{M}^{(2)}(-k_z)\mathbf{M}'(k_z) + \mathbf{N}(-k_z)\mathbf{N}^{(2)'}(k_z)] & \text{for } u > u' \end{cases} \quad (3.56)$$

3.2.5 The Electric Dyadic Green's function Of The First Kind

For a perfectly conducting elliptic cylinder as shown in Figure.3.2, the electric dyadic Green's function of the first kind must satisfies both the vector wave equation and Dirichlet boundary condition at the cylinder surface, $u = u_0$.

The dyadic Green's function of the first kind for a perfectly conducting elliptic cylinder can be written in terms of the free space dyadic Green's function that represents the incident field from source, and a scattering dyadic Green's function that represents the scattered field produced by the induced current on the surface of the elliptic cylinder. To satisfy the Dirichlet boundary condition on the surface of the elliptic cylinder, the following scattered field dyadic is assumed

$$\overline{\overline{G}}_{s1}(\mathbf{R}, \mathbf{R}') = -\frac{j}{2\pi} \int_{-\infty}^{\infty} dk_z \sum_{m=1}^{\infty} \frac{1}{\eta^2 I_{e_{om\eta}}} [\alpha_{\eta} \mathbf{M}^{(2)}(-k_z) \mathbf{M}^{(2)'}(k_z) + \beta_{\eta} \mathbf{N}^{(2)}(-k_z) \mathbf{N}^{(2)'}(k_z)] \quad (3.57)$$

and then the total dyadic Green's function can be represented as the superposition of (3.56) and (3.57)

$$\begin{aligned} \overline{\overline{G}}_{e1}(\mathbf{R}, \mathbf{R}') &= \overline{\overline{G}}_{e0}(\mathbf{R}, \mathbf{R}') + \overline{\overline{G}}_{s1}(\mathbf{R}, \mathbf{R}') \\ &= \frac{1}{k^2} [-\mathbf{u}\mathbf{u}\delta(\mathbf{R} - \mathbf{R}')] - \frac{j}{2\pi} \int_{-\infty}^{\infty} dk_z \sum_{m=1}^{\infty} \frac{1}{\eta^2 I_{e_{om\eta}}} \\ &\quad \cdot \begin{cases} [\mathbf{M}(-k_z) + \alpha_{\eta} \mathbf{M}_{\eta}^{(2)}(-k_z)] \mathbf{M}_{\eta}^{(2)'}(k_z) + [\mathbf{N}(-k_z) + \beta_{\eta} \mathbf{N}^{(2)}(-k_z)] \mathbf{N}^{(2)'}(k_z) & \text{for } u < u' \\ [\mathbf{M}'(k_z) + \alpha_{\eta} \mathbf{M}_{\eta}^{(2)'}(k_z)] \mathbf{M}_{\eta}^{(2)}(-k_z) + [\beta_{\eta} \mathbf{N}^{(2)'}(k_z) + \mathbf{N}'(k_z)] \mathbf{N}^{(2)}(-k_z) & \text{for } u > u' \end{cases} \end{aligned} \quad (3.58)$$

By the Dirichlet boundary condition,

$$\mathbf{u} \times \overline{\overline{G}}_{e1}(\mathbf{R}, \mathbf{R}') = 0 \quad \text{for } u = u_0 \quad (3.59)$$

Th

Di

are

Fro

Ins

an

for

The two unknown variables, α_η and β_η in (3.58), are determined by enforcing the

Dirichlet boundary condition. From (3.27) to (3.29), it is observed that $\mathbf{N}^{(2) \prime}$ and $\mathbf{M}^{(2) \prime}$

are orthogonal. By this orthogonal property, the following relationships are obtained

$$\begin{aligned}\mathbf{u} \times [\mathbf{M}(-k_z) + \alpha_\eta \mathbf{M}^{(2)}(-k_z)]_{u=u_0} &= 0 \\ \mathbf{u} \times [\mathbf{N}(-k_z) + \beta_\eta \mathbf{N}^{(2)}(-k_z)]_{u=u_0} &= 0\end{aligned}\quad (3.60)$$

From (3.25) and (3.26), the vector wave functions are found to be

$$\begin{aligned}\mathbf{N}(-k_z) &= \frac{1}{k\beta} \left(-jk_z S_\eta \frac{\partial R_\eta}{\partial u} \mathbf{u} - jk_z R_\eta \frac{\partial S_\eta}{\partial v} \mathbf{v} + \beta k_\rho^2 R_\eta S_\eta \mathbf{z} \right) e^{-jk_z z} \\ \mathbf{M}(-k_z) &= \frac{1}{\beta} \left(R_\eta \frac{\partial S_\eta}{\partial v} \mathbf{u} - S_\eta \frac{\partial R_\eta}{\partial u} \mathbf{v} \right) e^{-jk_z z} \\ \mathbf{N}^{(2)}(-k_z) &= \frac{1}{k\beta} \left(-jk_z S_\eta \frac{\partial R_\eta^{(2)}}{\partial u} \mathbf{u} - jk_z R_\eta^{(2)} \frac{\partial S_\eta}{\partial v} \mathbf{v} + \beta k_\rho^2 R_\eta^{(2)} S_\eta \mathbf{z} \right) e^{-jk_z z} \\ \mathbf{M}^{(2)}(-k_z) &= \frac{1}{\beta} \left(R_\eta^{(2)} \frac{\partial S_\eta}{\partial v} \mathbf{u} - S_\eta \frac{\partial R_\eta^{(2)}}{\partial u} \mathbf{v} \right) e^{-jk_z z}\end{aligned}\quad (3.61)$$

Inserting (3.61) into (3.60), the unknown coefficients are given by

$$\alpha_\eta = - \frac{\left. \frac{\partial R_\eta(u)}{\partial u} \right|_{u=u_0}}{\left. \frac{\partial R_\eta^{(2)}(u)}{\partial u} \right|_{u=u_0}} \quad \beta_\eta = - \frac{R_\eta(u)}{R_\eta^{(2)}(u)} \Big|_{u=u_0} \quad (3.62)$$

and (3.58) becomes

for $u > u'$

$$\begin{aligned}
\overline{\overline{G}}_{e1}(\mathbf{R}, \mathbf{R}') = & -\frac{1}{k^2} [\mathbf{u}\mathbf{u}\delta(\mathbf{R} - \mathbf{R}')] - \frac{j}{2\pi} \int_{-\infty}^{\infty} dk_z \sum_{m=1}^{\infty} \frac{1}{\eta^2 I_{e_{om\eta}}} \{ [\mathbf{M}'(k_z) \\
& - \left. \frac{\partial R_\eta(u)}{\partial R_\eta^{(2)}(u)} \right|_{\partial u} \Big|_{u=u_0} \mathbf{M}_\eta^{(2)'(-k_z)}] \mathbf{M}_\eta^{(2)}(-k_z) \\
& + \left[\frac{R_\eta(u)}{R_\eta^{(2)}(u)} \right]_{u=u_0} \mathbf{N}^{(2)'(k_z)} + \mathbf{N}'(k_z)] \mathbf{N}^{(2)}(-k_z) \}
\end{aligned} \tag{3.63}$$

for $u < u'$

$$\begin{aligned}
\overline{\overline{G}}_{e1}(\mathbf{R}, \mathbf{R}') = & -\frac{1}{k^2} [\mathbf{u}\mathbf{u}\delta(\mathbf{R} - \mathbf{R}')] - \frac{j}{2\pi} \int_{-\infty}^{\infty} dk_z \sum_{m=1}^{\infty} \frac{1}{\eta^2 I_{e_{om\eta}}} \\
& \left\{ \left[\mathbf{M}(-k_z) - \left. \frac{\partial R_\eta(u)}{\partial R_\eta^{(2)}(u)} \right|_{\partial u} \right]_{u=u_0} \mathbf{M}_\eta^{(2)}(-k_z) \right] \mathbf{M}_\eta^{(2)'}(k_z) \\
& + \left[\mathbf{N}(-k_z) - \frac{R_\eta(u)}{R_\eta^{(2)}(u)} \right]_{u=u_0} \mathbf{N}^{(2)}(-k_z) \right] \mathbf{N}^{(2)'}(k_z) \}
\end{aligned} \tag{3.64}$$

3.2.6 The Electric Dyadic Green's function Of The Second Kind

The electric dyadic Green's function of the second kind can be determined by applying the same procedures used for the derivation of the first kind dyadic Green's function except that the Neumann condition is enforced on the surface instead of the Dirichlet condition. The final expression for the electric Dyadic Green's function is given by

for $u > u'$

$$\begin{aligned}
\overline{G}_{e2}(\mathbf{R}, \mathbf{R}') &= -\frac{1}{k^2} [\mathbf{u}\mathbf{u}\delta(\mathbf{R} - \mathbf{R}')] \\
&\quad - \frac{j}{2\pi} \int_{-\infty}^{\infty} dk_z \sum_{m=1}^{\infty} \frac{1}{\eta^2 I_{\epsilon_{\sigma m \eta}}} \left\{ \left[\mathbf{M}'(k_z) - \frac{R_{\eta}(u)}{R_{\eta}^{(2)}(u)} \right]_{u=u_0} \mathbf{M}_{\eta}^{(2)'}(k_z) \right] \mathbf{M}_{\eta}^{(2)}(-k_z) \\
&\quad + \left[\mathbf{N}'(k_z) - \frac{\partial R_{\eta}(u) / \partial u}{\partial R_{\eta}^{(2)}(u) / \partial u} \right]_{u=u_0} \mathbf{N}^{(2)'}(k_z) \right] \mathbf{N}^{(2)}(-k_z) \left. \right\}
\end{aligned} \tag{3.65}$$

for $u < u'$

$$\begin{aligned}
\overline{G}_{e2}(\mathbf{R}, \mathbf{R}') &= -\frac{1}{k^2} [\mathbf{u}\mathbf{u}\delta(\mathbf{R} - \mathbf{R}')] \\
&\quad - \frac{j}{2\pi} \int_{-\infty}^{\infty} dk_z \sum_{m=1}^{\infty} \frac{1}{\eta^2 I_{\epsilon_{\sigma m \eta}}} \left\{ \left[\mathbf{M}(-k_z) - \frac{R_{\eta}(u)}{R_{\eta}^{(2)}(u)} \right]_{u=u_0} \mathbf{M}_{\eta}^{(2)}(-k_z) \right] \mathbf{M}_{\eta}^{(2)'}(k_z) \\
&\quad + \left[\mathbf{N}(-k_z) - \frac{\partial R_{\eta}(u) / \partial u}{\partial R_{\eta}^{(2)}(u) / \partial u} \right]_{u=u_0} \mathbf{N}^{(2)}(-k_z) \right] \mathbf{N}^{(2)'}(k_z) \left. \right\}
\end{aligned} \tag{3.66}$$

For $u = u' = u_0$, each component of the dyadic Green's function of second kind can be simplified as

$$\begin{aligned}
G_{e2}^{vv'}(u_0, v', z' | u_0, v, z) &= \frac{1}{2\pi} \int_{-\infty}^{\infty} dk_z \sum_{m=1}^{\infty} \frac{1}{\eta^2 I_{\epsilon_{\sigma m \eta}} \beta \beta'} \left[\frac{R_{\eta}'(u_0)}{R_{\eta}^{(2)}(u_0)} S_{\eta}(v) S_{\eta}(v') \right. \\
&\quad \left. - \frac{k_z^2}{k^2} \frac{R_{\eta}^{(2)}(u_0)}{R_{\eta}^{(2)}(u_0)} S_{\eta}'(v) S_{\eta}'(v') \right] e^{-jk_z(z-z')} \\
G_{e2}^{vz'}(u_0, v', z' | u_0, v, z) &= \frac{-j}{2\pi} \int_{-\infty}^{\infty} dk_z \sum_{m=1}^{\infty} \frac{k_z}{I_{\epsilon_{\sigma m \eta}} \beta k^2} \frac{R_{\eta}^{(2)}(u_0)}{R_{\eta}^{(2)}(u_0)} S_{\eta}'(v) S_{\eta}(v') e^{-jk_z(z-z')} \\
G_{e2}^{zz'}(u_0, v', z' | u_0, v, z) &= \frac{-1}{2\pi} \int_{-\infty}^{\infty} dk_z \sum_{m=1}^{\infty} \frac{k_z^2}{I_{\epsilon_{\sigma m \eta}} k^2} \frac{R_{\eta}^{(2)}(u_0)}{R_{\eta}^{(2)}(u_0)} S_{\eta}'(v) S_{\eta}(v') e^{-jk_z(z-z')}
\end{aligned} \tag{3.67}$$

where

$$S_{\eta}(v) = S_{\epsilon_{om\lambda}}(v) = \begin{cases} \sum_{n=0}^{\infty} D_n^m \cos nv, & m=1,2,3,\dots \\ \sum_{n=0}^{\infty} F_n^m \sin nv, & m=1,2,3,\dots \end{cases} \quad (3.68)$$

and the prime attached to S and R denotes the first derivate with respect with v and u , respectively, while it represents the source point for the others. Since (3.67) is computationally prohibitive for $m > 12$ or for a large argument in the Hankel functions, an asymptotic dyadic Green's function is developed for practical implementation.

3.3 The Asymptotic Dyadic Green's Function

The general expression for the magnetic field due to the magnetic source on a convex surface, shown in Figure 3.3, has been developed by Pathak and Wang [25]. For convenience, this general expression is given as follows,

$$\begin{aligned} d\mathbf{H}_m(Q|Q') = \frac{kG_0Y_0}{2\pi j} d\mathbf{P}_m(Q) \{ & \mathbf{b}'\mathbf{b} \left[\left(1 - \frac{j}{kt} - \frac{1}{k^2t^2} - \tilde{T}_0^2 \frac{j}{kt}\right) \tilde{V}(\xi) + \tilde{T}_0^2 \frac{j}{kt} \tilde{U}(\xi) \right] \\ & + \mathbf{t}'\mathbf{t} \left[\left(\frac{j}{kt} + \frac{2}{k^2t^2}\right) \tilde{V}(\xi) + \frac{j}{kt} \tilde{U}(\xi) \right] + (\mathbf{t}'\mathbf{b} + \mathbf{b}'\mathbf{t}) \left[\frac{j}{kt} (\tilde{U}(\xi) - \tilde{V}(\xi)) \tilde{T}_0 \right] \} \end{aligned} \quad (3.69)$$

where the $\tilde{U}(\xi)$ and $\tilde{V}(\xi)$ are related to the soft and hard Fock functions, respectively.

They are characteristic of on-surface creeping wave interactions and have been extensively investigated by Logan [29]. The unit vectors in (3.69) associated with surface coordinates are shown in Figure 3.3. The quantities G_0 and Y_0 are the free-space Green's function and admittance, respectively. The quantities k and t refer to the free-space wavenumber and the surface ray geodesic path from source point Q' to test point Q . The

factor \tilde{T}_0 is identified as a ratio of the surface ray torsion and the surface curvature along the ray direction. It is expressed as

$$\tilde{T}_0^2 = \left[\frac{\sin^2(2\delta)}{4} \left(\frac{1}{R_2(Q')} - \frac{1}{R_1(Q')} \right) \rho_g(Q') \right] \left[\left(\frac{1}{R_2(Q)} - \frac{1}{R_1(Q)} \right) \rho_g(Q) \right] \quad (3.70)$$

where R_1 and R_2 are the principal surface radii of curvature in the \mathbf{b} and \mathbf{t} direction, respectively. Also ρ_g denotes the surface radius of curvature and δ is the angle between the axial axis and the direction of the geodesic trajectory. For the elliptic cylinder, since the principal surface radius of curvature in the axial direction, R_1 , approaches infinity, (3.70) can be reduced to

$$\tilde{T}_0^2 = \frac{\sin^2(2\delta)}{4R_2(Q)R_2(Q')} \rho_g(Q') \rho_g(Q) \quad (3.71)$$

The asymptotic dyadic Green's function for the surface interactions on an elliptic cylinder, as shown in Figure 3.5, can be developed based on the general expression in (3.69) by using the following relationship between surface and elliptic coordinate systems

$$\begin{aligned} \mathbf{u} &= \mathbf{n}, & \mathbf{u}' &= \mathbf{n}' \\ \mathbf{v} &= \mathbf{t} \sin \delta + \mathbf{b} \cos \delta, & \mathbf{v}' &= \mathbf{t}' \sin \delta + \mathbf{b}' \cos \delta \\ \mathbf{z} &= \mathbf{t} \cos \delta - \mathbf{b} \sin \delta, & \mathbf{z}' &= \mathbf{t}' \cos \delta - \mathbf{b}' \sin \delta \end{aligned} \quad (3.72)$$

Hence, the components of the asymptotic dyadic Green's function of the second kind for the surface of the elliptic cylinder can be expressed as

$$\begin{aligned}
G_{\mathbf{v}\mathbf{v}}(Q|Q') &= \frac{G_0}{2\pi} \left\{ \tilde{V}(\xi) [\cos^2 \delta + \frac{j}{kt} (-1 + \tilde{T}_0^2) \cos^2 \delta + \sin^2 \delta - \tilde{T}_0 \sin 2\delta] \right. \\
&\quad \left. + \frac{1}{k^2 t^2} (-\cos^2 \delta + 2 \sin^2 \delta) + \tilde{U}(\xi) [\frac{j}{kt} (\tilde{T}_0^2 \cos^2 \delta + \sin^2 \delta + \tilde{T}_0 \sin 2\delta)] \right\} \\
G_{\mathbf{z}\mathbf{v}}(Q|Q') &= \frac{G_0}{2\pi} \left\{ \tilde{V}(\xi) [-\frac{1}{2} \sin 2\delta + \frac{j}{kt} (\sin 2\delta + \frac{1}{2} \tilde{T}_0^2 \sin 2\delta - (\cos^2 \delta - \sin^2 \delta) \tilde{T}_0) \right. \\
&\quad \left. + \frac{3}{2k^2 t^2} \sin 2\delta + \tilde{U}(\xi) [\frac{j}{kt} (-\frac{1}{2} \tilde{T}_0^2 \sin 2\delta + \frac{1}{2} \sin 2\delta + (\cos^2 \delta - \sin^2 \delta) \tilde{T}_0)] \right\} \quad (3.73)
\end{aligned}$$

$$\begin{aligned}
G_{\mathbf{z}\mathbf{z}}(Q|Q') &= \frac{G_0}{2\pi} \left\{ \tilde{V}(\xi) [\sin^2 \delta + \frac{j}{kt} (-1 + \tilde{T}_0^2) \sin^2 \delta + \cos^2 \delta + \tilde{T}_0 \sin 2\delta] \right. \\
&\quad \left. + \frac{1}{k^2 t^2} (-\sin^2 \delta + 2 \cos^2 \delta) + \tilde{U}(\xi) [\frac{j}{kt} (\tilde{T}_0^2 \sin^2 \delta + \cos^2 \delta - \tilde{T}_0 \sin 2\delta)] \right\}
\end{aligned}$$

where

$$\begin{aligned}
\tilde{u}(\xi) &= \left[\frac{kt}{2m(Q)m(Q')} \right]^{3/2} U(\xi), & \tilde{v}(\xi) &= \left[\frac{kt}{2m(Q)m(Q)\xi} \right]^{1/2} V(\xi) \\
\text{and } \xi &= \int_Q^Q \frac{m(t)}{\rho_g(t)} dt, & m(t) &= \left[\frac{k\rho_g(t)}{2} \right]^{1/3}
\end{aligned} \quad (3.74)$$

Here ξ is the Fock parameter and $\rho_g(t)$ denotes the surface radius of curvature. Also in

(3.74), t is the geodesic path length $t = \sqrt{(\int_Q^Q \rho dv)^2 + z^2}$. From (3.73) and (3.74), it is

observed that the variation of surface field between the source and test points is primarily

governed by the Fock-type functions, $U(\xi)$ and $V(\xi)$. Since reciprocity applies, the

expression for $G_{\mathbf{z}\mathbf{v}}$ is exactly the same as $G_{\mathbf{v}\mathbf{z}}$. For the special case of the circular

cylinder, the various parameters simplify to $\tilde{T}_0 = \cot \delta$, $\rho_g(Q) = \rho_g(Q') = \frac{a}{\sin^2 \delta}$, and

therefore $\tilde{U}(\xi) = U(\xi)$, $\tilde{V}(\xi) = V(\xi)$. Accordingly, (3.73) reduces to the dyadic Green's

function for the circular cylinder as follows,

www.ck12.org

$$\begin{aligned}
G_{\mathbf{v}\mathbf{v}}(Q|Q') &= \frac{-je^{-jk\xi}}{2\pi} kq \{ V(\xi) [\sin^2 \theta + q(1-q)(2-3\sin^2 \theta) + q(U(\xi) - V(\xi)) \sec^2 \theta] \} \\
G_{\mathbf{v}\mathbf{z}}(Q|Q') &= \frac{je^{-jk\xi}}{2\pi} kq \sin \theta \cos \theta \{ [1-3q(1-q)]V(\xi) \} \\
G_{\mathbf{z}\mathbf{z}}(Q|Q') &= \frac{-je^{-jk\xi}}{2\pi} kq \{ [\cos^2 \theta + q(1-q)(2-3\cos^2 \theta)]V(\xi) \}
\end{aligned} \tag{3.75}$$

where $\theta = \frac{\pi}{2} - \delta$ and $q = \frac{j}{kt}$.

The electric dyadic Green's function in the surface integral above is expressed in terms of a rapidly convergent creeping wave series [24] expressed in terms of Fock functions. As an example, consider an ellipse with major and minor axis of 4 cm and 2 cm, respectively, an angle between axial axis and the direction of creeping wave trace $\delta = 80^\circ$, and a frequency of 30 GHz. The magnitude of each component of the electric dyadic Green's function versus the geodesic path length is shown in Figure 3.5. For comparison, the dyadic Green's function on the surface of the circular cylinder with a radius of 4 cm is shown in Figure 3.6.

In figure 3.5 the creeping waves on the surface of the cylinder are found to have greater attenuation in regions with larger curvature than those with less curvature. This can be explained by the fact that the creeping wave energy will rapidly shed away from the surface as it travels in regions with greater curvature. It also can be observed in Figure 3.6 that the rate of energy loss for the creeping wave on the surface of a circular cylinder almost remains constant after traveling three wavelengths along the geodesic path. This is due to the fact that the curvature of the surface over which the wave travels does not vary along the geodesic path.

3.4 Boundary Integral Matrix

In the FE-BI formulation developed in Chapter 2, the entries of the boundary integral sub-matrix are given by

$$G_{ij}^{BI} = k_0^2 \iint_{s_j s_i} \mathbf{W}_i^e(u, v, z) \cdot \mathbf{u}(u, v, z) \times [\mathbf{u}(u, v, z) \times \mathbf{W}_j(u, v, z) \cdot \overline{\mathbf{G}}_{e2}(u, v, z)] \beta' \beta dv' dz' dvdz \quad (3.76)$$

Substituting the vector weight functions given in Chapter 2 into (3.76), the following components of (3.76) are obtained

$$\begin{aligned} G_{zz}^{BI} &= -k_0^2 \frac{\tilde{S}_i \tilde{S}_j}{\alpha_i \alpha_j} \iint_{s_j s_i} (v - \tilde{v}_i)(v' - \tilde{v}_j) G_{e2}^{vv'} \beta_1' \beta_1 dv' dz' dvdz \\ G_{zv}^{BI} &= k_0^2 \frac{\tilde{S}_i \tilde{S}_j c \Delta_{v_l^j}}{\alpha_i h_j} \iint_{s_j s_i} (v - \tilde{v}_i)(z' - \tilde{z}_j) G_{e2}^{zv'} \beta_1' dv' dz' dvdz \\ G_{vz}^{BI} &= k_0^2 \frac{\tilde{S}_i \tilde{S}_j c \Delta_{v_l^i}}{h_i \alpha_j} \iint_{s_j s_i} (z - \tilde{z}_i)(v' - \tilde{v}_j) G_{e2}^{z'v} \beta_1' dv' dz' dvdz \\ G_{vv}^{BI} &= k_0^2 \frac{\tilde{S}_i \tilde{S}_j c^2 \Delta_{v_l^j} \Delta_{v_l^i}}{h_i h_j} \iint_{s_j s_i} (z - \tilde{z}_i)(z' - \tilde{z}_j) G_{e2}^{z'z} dv' dz' dvdz \end{aligned} \quad (3.77)$$

where the components of the dyadic Green's function of the second kind are given in (3.73) and

$$\begin{aligned} \beta_1' &= c(\cosh^2 u_1 - \cos^2 v')^{1/2} \\ \beta_1 &= c(\cosh^2 u_1 - \cos^2 v)^{1/2} \\ \Delta_{v_l^i} &= (\cosh^2 u_1 - \cos^2 v_l^i)^{1/2} \\ \Delta_{v_l^j} &= (\cosh^2 u_1 - \cos^2 v_l^j)^{1/2} \end{aligned} \quad (3.78)$$

When the elliptic cylinder is reduced to a circular cylinder by the transformation

$v = \phi$, $\rho \approx \frac{c}{2} e^u$, the boundary integral contributions for the circular cylinder are given by

$$\begin{aligned}
 G_{zz}^{\text{BI}} &= -k_0^2 \frac{\tilde{S}_i \tilde{S}_j}{\alpha_i \alpha_j} \iint_{s_j s_i} (\phi - \tilde{\phi}_i)(\phi' - \tilde{\phi}_j) G_{e_2}^{\phi\phi'} d\phi' dz' d\phi dz \\
 G_{zv}^{\text{BI}} &= k_0^2 \frac{\tilde{S}_i \tilde{S}_j}{\alpha_i h_j} \iint_{s_j s_i} (\phi - \tilde{\phi}_i)(z - \tilde{z}_j) G_{e_2}^{\phi z} d\phi' dz' d\phi dz \\
 G_{vv}^{\text{BI}} &= -k_0^2 \frac{\tilde{S}_i \tilde{S}_j \rho_1^2}{h_i h_j} \iint_{s_j s_i} (z - \tilde{z}_i)(z' - \tilde{z}_j) G_{e_2}^{z'z} d\phi' dz' d\phi dz
 \end{aligned} \tag{3.79}$$

where the components of the dyadic Green's functions of the second kind are given in (3.75) and

$$\begin{aligned}
 t_{i,j} &= \rho_b - \rho_a \\
 \phi_{i,j} &= \phi_l^{i,j} - \phi_r^{i,j} \\
 h_{i,j} &= z_i^{i,j} - z_b^{i,j}
 \end{aligned} \tag{3.80}$$

The subscript i and j represent the test and source unknown numbers, respectively, and the surface integrals have support over the area of test and source elements containing the test and source edges.

For the non-self-cell contribution, mid-point integration may be used for computation of (3.76) and the asymptotical dyadic Green's functions in (3.73) are applied. Since for the self-cell contribution the source element will coincide with the test element in evaluating (3.76), the planar Green's function is used to overcome the singular integrals in (3.77). The contribution of the planar Green's function is given by

$$G_{ij}^p = 2(k_0 a)^2 \iint_{s_i s_j} \mathbf{w}_i \cdot [\mathbf{u} \times \overline{\overline{G_0}} \times \mathbf{u}] \cdot \mathbf{w}_s ds' ds \tag{3.81}$$

function is applied. Otherwise, the planar dyadic Green's function is used in the calculation.

3.5 Excitation: FE-BI

Conformal antenna patches are typically fed by a microstrip line printed along with the radiator on the surface of the substrate or by a probe from below the patch. The microstrip lines are in turn fed by a coaxial probe that originates behind the cavity as shown in Figure 3.7. For convenience, the internal source is located on one of the unknown edges. The source term f_i^{int} in the FE-BI formulation can be expressed for three probe orientations as follows. For radial probe,

$$\mathbf{J} = \mathbf{u} \frac{\delta(v - v_s) \delta(z - z_s) I_0}{\beta} \quad (3.86)$$

$$f_i^{\text{int}} = -jk_0 Z_0 I_0 \frac{\tilde{s}_i(v_s - \tilde{v}_i)(z_s - \tilde{z}_i)(u_b - u_a) \beta_{u_b, v_s}}{\alpha \cdot h}$$

For azimuthal probe,

$$\mathbf{J} = \mathbf{v} \frac{\delta(u - u_s) \delta(z - z_s) I_0}{\beta} \quad (3.87)$$

$$f_i^{\text{int}} = -jk_0 Z_0 I_0 \frac{\tilde{s}_i(\rho_{u_s} - \rho_{\tilde{u}_i})(z_s - \tilde{z}_i) \beta_{u_s, v_l} \alpha}{t \cdot h}$$

For axial probe,

$$\mathbf{J} = \mathbf{z} \frac{\delta(u - u_s) \delta(v - v_s) I_0}{\beta} \quad (3.88)$$

$$f_i^{\text{int}} = -jk_0 Z_0 I_0 \frac{\tilde{s}_i(\rho_{u_s} - \rho_{\tilde{u}_i})(v_s - \tilde{v}_i) \beta_{u_s, v_s} h}{t \cdot \alpha}$$

where $\beta_{u_s, v_l} = c(\cosh^2 u_s - \cos^2 v_l)^{1/2}$ and the Dirac delta functions serve to specify the location of the infinitesimally thin probe.

It should be remembered that even though the source edge is shared by four elements, only one of them is used for computation [10]. Also, it is observed that the number of non-zero entries in the right hand side of the linear system is equal to the number of sources.

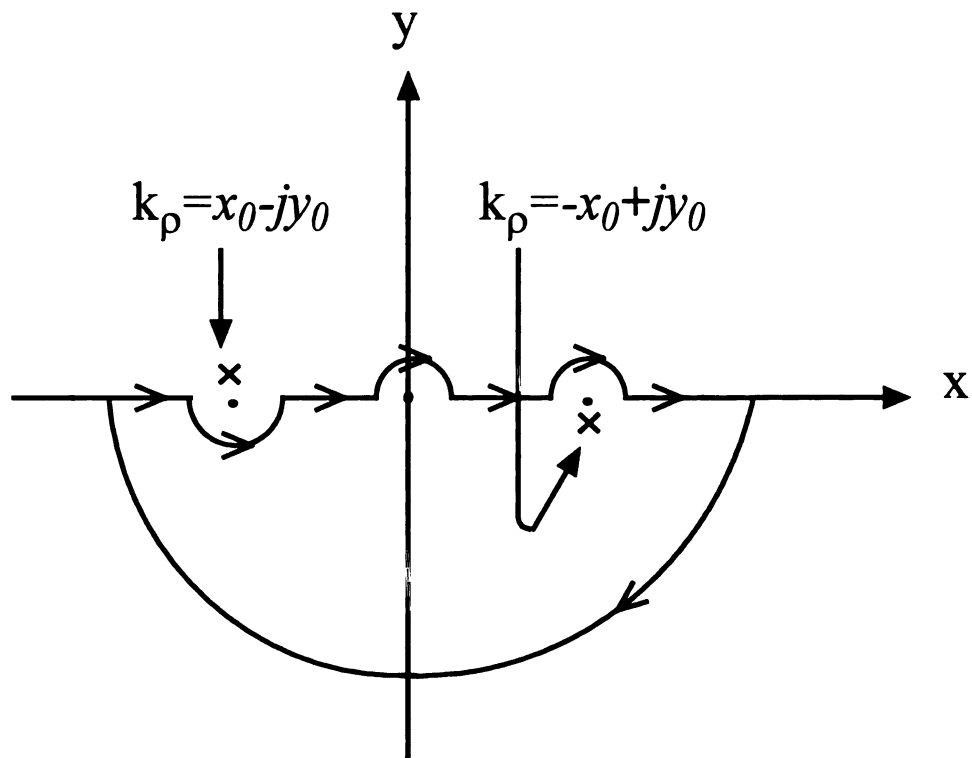


Figure 3.1 Contour for converting the eigenfunction expansion into a mode expansion.

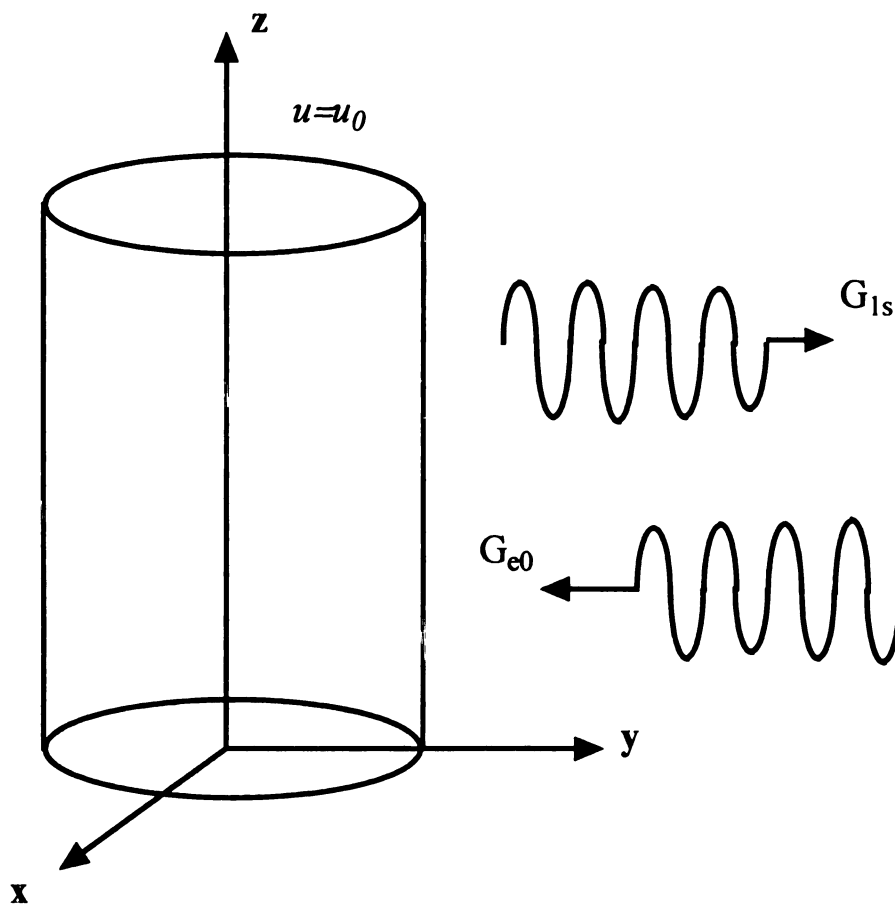


Figure 3.2 The scattering wave and incident wave for an elliptic cylinder.

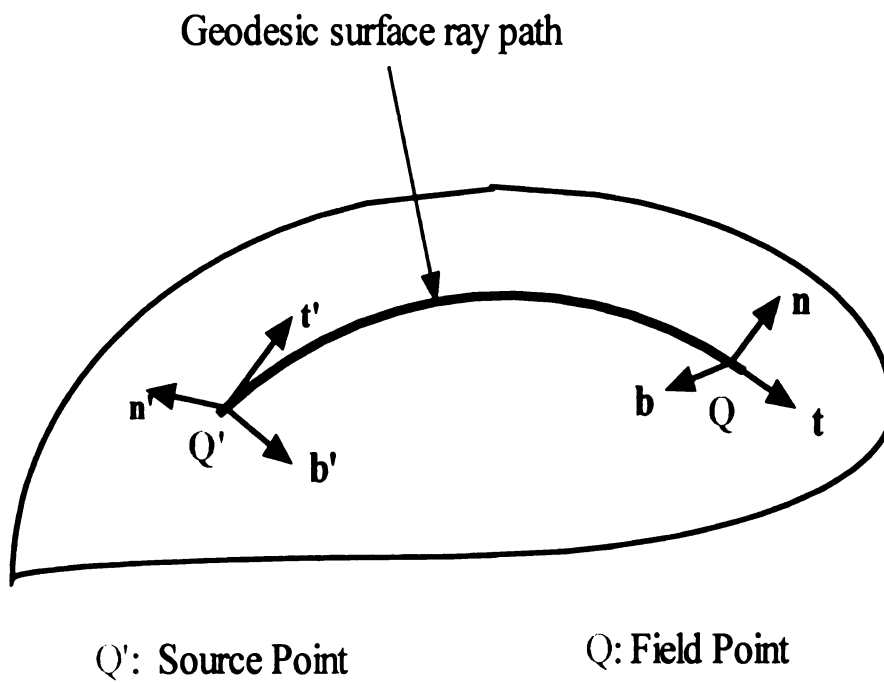


Figure 3.3 Illustration of unit vectors for a convex surface.

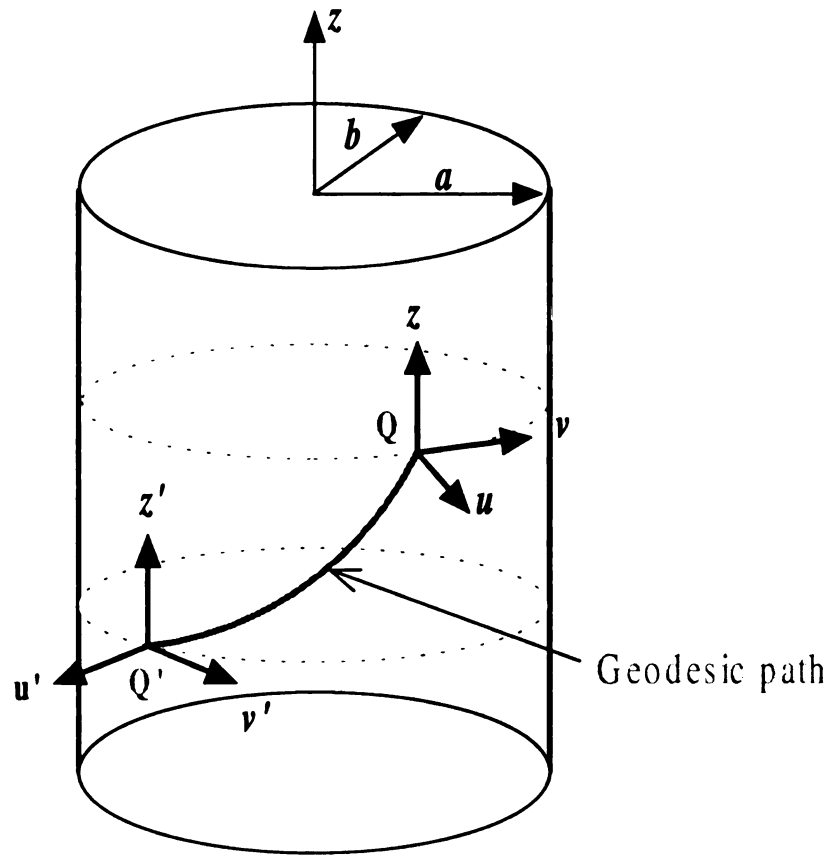


Figure 3.4 Geodesic path for the creeping wave on an elliptic cylinder.

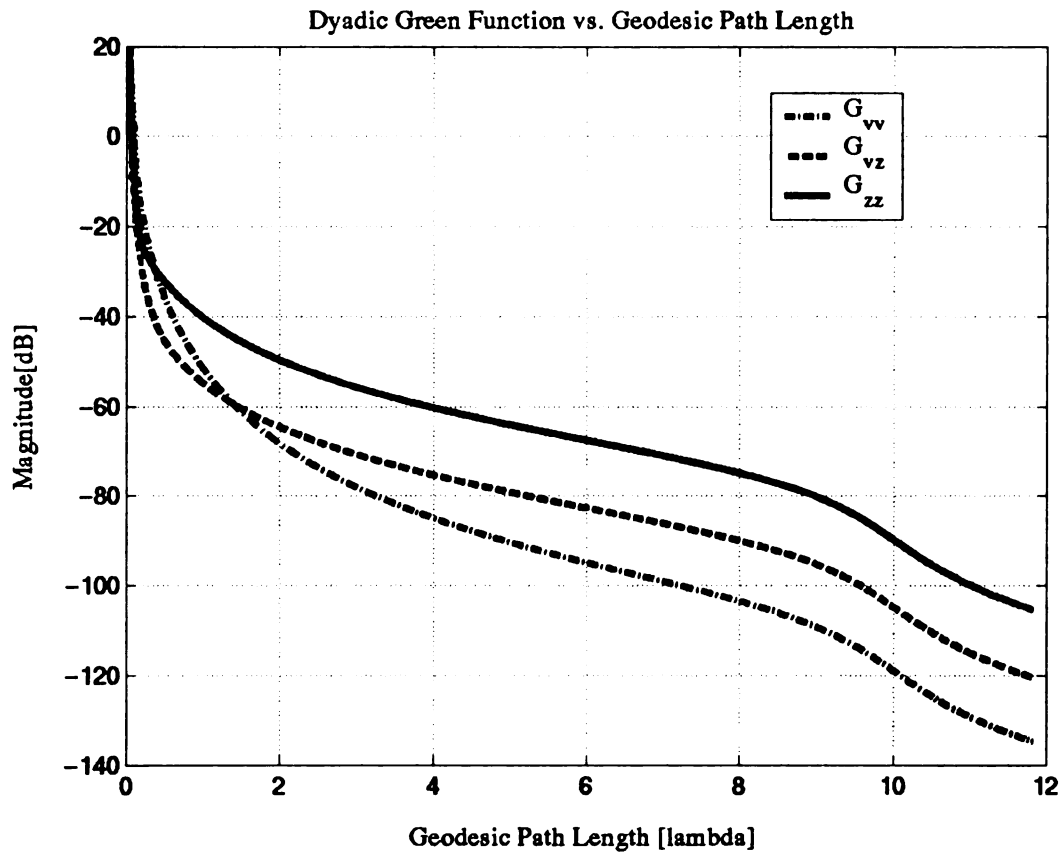


Figure 3.5 Magnitude of the three components of asymptotic dyadic Green's function for an elliptic cylinder.

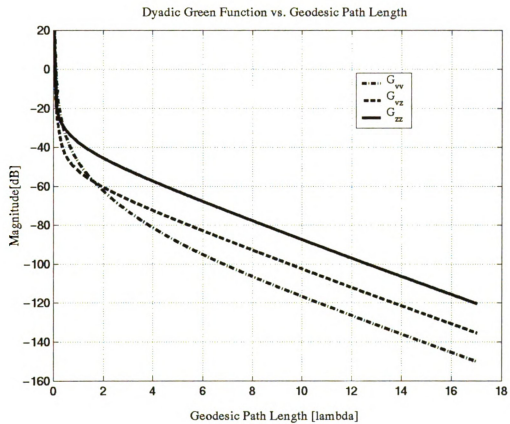


Figure 3.6 Magnitude of the three components of asymptotic dyadic Green's function for a circular cylinder.

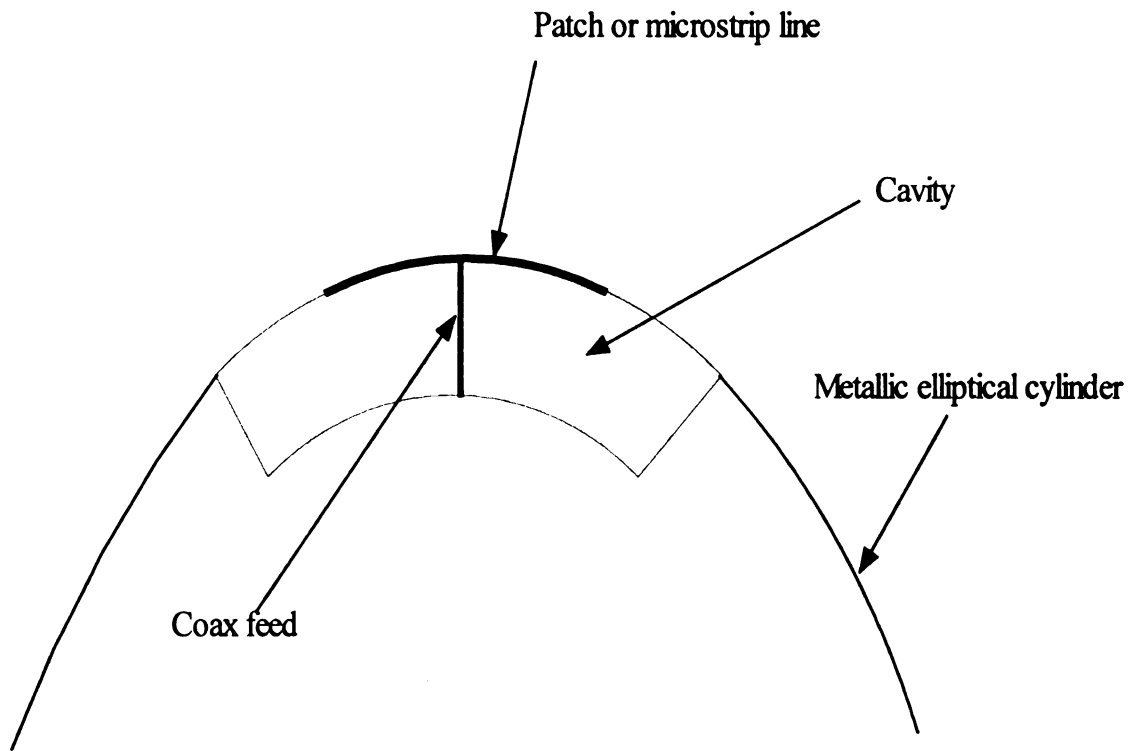


Figure 3.7 Cavity-backed probe-fed conformal patch antenna recessed in an infinite, perfectly conducting elliptical cylinder.

CHAPTER 4

DRIVING POINT IMPEDANCE RESULTS

4.1 Introduction

The increasing use of microstrip antenna technology requires analysis methods capable of accurately predicting the input impedance and mutual coupling between these antennas. The information generated will provide a useful reference for practicing engineers and scientists in the design of microstrip antennas and circuits for installation on curved surfaces and for studying the electromagnetic compatibility of multiple antennas. There are several methods that have been somewhat successful for calculating the input impedance and radiation from microstrip antennas such as the transmission line model, cavity model [2], and moment method. However, those analysis methods only focus on simple planar or non-planar structures such as cylindrical, spherical and conical coated surfaces.

The hybrid finite element – boundary integral (FE-BI) method allows the simulation of complex, cavity-backed antennas with minimal computational effort. The effects of resonant frequency and input impedance due to the variation of curvature for an elliptic cylinder can be examined by this approach. In this solution, the surface fields that propagate along each ray's geodesic path remain uniformly valid within the shadow boundary transition region, including in the immediate vicinity of the source.

In this chapter the calculation model for the input impedance of a cavity-backed, printed antenna is introduced. The input impedance for an empty cavity, a slot antenna and a conformal patch antenna embedded on the surface of an elliptic cylinder are discussed separately. Of course, the elliptic cylinder can be reduced to a circular cylinder. Results from a previous method appropriate for a circular cylinder structure are compared

with the results using this new method. When the radius of curvature of a cylinder becomes large, the conformal antenna model reduces to a similar method for planar antennas.

4.2. System Solution

Since the FE-BI method produces a large, sparse linear matrix system, the biconjugate gradient (BiCG) solver has been chosen as it requires significantly less memory than is required for a direct method. The BiCG method is also computationally efficient, since it utilizes only one matrix-vector product per iteration. This operation represents the bulk of the computational demand of the method and requires $\mathcal{O}(N_s^2)$ complex operations per iteration for the fully populated boundary integral matrix, where N_s is the number of aperture unknowns. If the matrix is not fully populated, i.e. it is a sparse matrix, the Compressed Sparse Row (CSR) format may be used to reduce the memory demand, since only non-zero entries are stored. The FE matrix $[A]$ in (2.14) is such a sparse matrix. The CSR retains only the non-zero entries of the matrix in one long data vector with another data vector, the offset vector, which contains the number of non-zero elements per row of the matrix. An additional long vector, the pointer vector, is required to indicate the matrix column associated with each matrix entry. Thus the position of each element in the sparse matrix is uniquely defined. The matrix-vector product using CSR scheme is carried out by executing the sum

$$y[n] = [A]\{x\} = \sum_{n'=1}^{r[n]} A[e(n, n')]x[n'] \quad n = 1, 2, 3, \dots, N \quad (4.1)$$

where $r[n]$ is the number of non-zero entries per row of the matrix and $e(n, n')$ indicates which entry of the long data vector is associated with the matrix entry $A[e(n, n')]$. The boundary integral matrix-vector product involves the fully populated matrix.

4.3. Input Impedance

To accomplish feedline matching, designers are concerned with the input impedance of the conformal antenna. The FE approach allows the calculation of the input impedance of a radiating structure in a rather elegant manner. The input impedance is composed of two contributions [24]

$$Z_{in} = Z_p + Z_D \quad (4.2)$$

where the first term is the self-impedance associated with a finite thickness probe in the absence of the patch and the second term is the contribution of the patch current to the total input impedance. In this dissertation, the second term will be the focus of the computation, since for very thin substrates and thin probe wires, the contribution from the self-impedance is negligible. To determine the input impedance of a probe feed cavity-backed conformal antenna, the impressed model is applied to determine the formulation of the input impedance. The geometry of the impressed model is given in Figure 4.1. In

Figure 4.1 the impressed field maintained by a magnetic surface current $\mathbf{K}_m = \frac{(\mathbf{n} \times \mathbf{u})V}{2\delta}$

is represented by \mathbf{E}^i , which is a non-conservative field. The scattered “coulomb field” is expressed as \mathbf{E}^s , which also is called the secondary field. For the source generator to drive current \mathbf{J} against the action of \mathbf{E}^s through the terminal source region, the following condition should be satisfied,

$$|\mathbf{E}^i| > |\mathbf{E}^s| \quad (4.3)$$

Since the material is assumed to be a perfect conductor, then

$$\begin{aligned} \lim_{\sigma_t \rightarrow \infty} \mathbf{J} &= \lim_{\sigma_t \rightarrow \infty} \sigma_t (\mathbf{E}^i + \mathbf{E}^s) = \text{finite} \\ \Rightarrow \mathbf{E}^i &= -\mathbf{E}^s \end{aligned} \quad (4.4)$$

Therefore, the total field inside the source generator is zero.

The total field at the conductor surface within the ring in Figure 4.1 can be determined using the integral form of Faraday's Law,

$$\mathbf{E} = \mathbf{E}^s + \mathbf{E}^i = -\mathbf{u} \frac{V}{2\delta} \quad (4.5)$$

thus

$$-\int_{u_0-\delta}^{u_0+\delta} \mathbf{u} \cdot \mathbf{E} du = -\int_{u_0-\delta}^{u_0+\delta} \mathbf{u} \cdot (\mathbf{E}^i + \mathbf{E}^s) du = V \quad (4.6)$$

with (4.6), gives

$$\begin{aligned} VI(u = u_0) &= Z_{in}^i I_0^2 = -\int_{\Gamma} (\mathbf{u} \cdot \mathbf{E}) I(u) du \\ \Rightarrow Z_{in}^i &= -\frac{1}{I_0^2} \int_{\Gamma} \mathbf{u} \cdot \mathbf{E}(u) I(u) du \end{aligned} \quad (4.7)$$

where \mathbf{E} is also the field associated with the feed edge and $I(u)$ is the current at any point u while I_0 is the current at u_0 on the probe. The integration contour Γ represents the path that impressed current flows through.

For a radial post, the impressed current density \mathbf{J}^{int} is represented as

$$\mathbf{J}^{\text{int}}(u, v, z) = \mathbf{u} \frac{\delta(v - v_s) \delta(z - z_s) I_0}{\beta} \quad (4.8)$$

where $\beta = c(\cosh^2 u - \cos^2 v)^{1/2}$. Inserting (4.8) into (4.7), the input impedance for the radial post can be determined by the formula

$$Z_{in}^i = -\frac{E(i)}{I_0} c(\cosh^2 u_b - \cos^2 v_l)^{1/2} (u_b - u_a) \quad (4.9)$$

where $E(i)$ is the expansion coefficient of the electric field for the edge associated with the radial post. This coefficient is numerically determined by the FE-BI program.

Likewise, the impressed current for azimuthal and axial posts can be represented as

$$\begin{aligned} \mathbf{J}^{\text{int}}(u, v, z) &= \mathbf{v} \frac{\delta(u - u_s) \delta(z - z_s) I_0}{\beta} \quad \text{for azimuthal posts} \\ \mathbf{J}^{\text{int}}(u, v, z) &= \mathbf{z} \frac{\delta(u - u_s) \delta(v - v_s) I_0}{\beta} \quad \text{for axial posts} \end{aligned} \quad (4.10)$$

The formulations of the input impedance are

$$\begin{aligned} Z_{in}^i &= -\frac{E(i)}{I_0} c(\cosh^2 u_b - \cos^2 v_l)^{1/2} (v_l - v_r) \quad \text{for azimuthal probes} \\ Z_{in}^i &= -\frac{E(i)}{I_0} c(\cosh^2 u_b - \cos^2 v_l)^{1/2} h \quad \text{for axial probes} \end{aligned} \quad (4.11)$$

Utilizing the same technique that has been used in a previous chapter for reducing elliptic cylinder coordinate to equivalent circular cylinder coordinate, the input impedance for a conformal antenna mounted in circular cylinder are given by

$$\begin{aligned} Z_{in}^i &= -\frac{E(i)}{I_0} \rho_b \ln\left(\frac{\rho_b}{\rho_a}\right) \quad \text{for radial probes} \\ Z_{in}^i &= -\frac{E(i)}{I_0} \rho_b \alpha \quad \text{for azimuthal probes} \\ Z_{in}^i &= -\frac{E(i)}{I_0} \rho_b h \quad \text{for axial probes} \end{aligned} \quad (4.12)$$

where $\alpha = \phi_r - \phi_l$ and $h = z_t - z_b$, and ϕ_r, ϕ_l, z_t, z_b are defined in Figure 2.4.

4.4. Numerical Results and Discussions

After the lengthy theoretical development in the previous chapter, the simulation using this FE-BI model will be applied for the empty cavity, slot and patch conformal antennas and the numerical results will be discussed later.

4.4.1. The Empty Cavity

For simplification, the empty cavity enclosed on all sides by conducting walls having infinite conductivity will be discussed first. It involves the computation of finite elements and the source matrix without the need for the boundary integral matrix. In this case the empty cavity is embedded in a circular cylinder with a radius of 100 cm, shown in Figure 4.2. The size of the cavity is 6 cm x 3.75 cm x 1.5 cm and it was meshed into 576 elements with 1223 unknowns. Its unit cell is also shown in Figure 4.2. The radial probe feed is 0.5 cm long and is located at the point 0.9375 cm above the center of the front surface of cavity. The radial probe feed penetrates the back wall of the cavity and protrudes into the cavity. The computed result of the input impedance vs. frequency is shown in Figure 4.3. Since the radius of cylinder is large compared to the arc length of cavity, the circular shell cavity can be considered a pseudo-rectangular cavity, and thus the input impedance can be compared with the data computed using the program LMBRICK(a.k.a. Low Memory Brick) [10]. That program utilizes the optimization for brick element implementations of the FE-BI method. From the results shown, there is very good agreement between the results calculated by the FE-BI program and

LMBRICK. Since the walls of the cavity are assumed to be a perfect electrical conductor, there is no loss mechanism associated with the cavity and hence its input impedance is purely reactive. The computed resonant frequency is 4.725 GHz for the lowest excited mode. This frequency can be theoretically calculated by the following formulation [30]

$$(f_r)_{mnp}^{TM,TE} = \frac{1}{2\pi\sqrt{\mu\epsilon}} \left[\left(\frac{m\pi}{a}\right)^2 + \left(\frac{n\pi}{b}\right)^2 + \left(\frac{p\pi}{c}\right)^2 \right]^{1/2} \quad (4.13)$$

where $m = 1, 2, 3, \dots$, $n = 1, 2, 3, \dots$, $p = 0, 1, 2, \dots$ for TM modes and $m = 0, 1, 2, 3, \dots$, $n = 0, 1, 2, 3, \dots$, $p = 1, 2, \dots$, $m \neq n = 0$ for TE modes.

The lowest excited mode for this cavity is TE_{101} and its theoretical resonant frequency is 4.717 GHz. The deviation between theoretical and computed results is approximately 0.17%. Agreement can be improved if the sampling frequency step is set to 0.025 GHz or to a smaller value. If the same conformal antenna is embedded in a cylinder with a radius of 5 cm, the computation result shown in Figure 4.4 is obtained. Compared to the previous case it can be observed that the resonant frequency shifts to 4.975 GHz.

From this case the solution involving the computation of the finite element and source matrices agrees with the theoretical solution when an empty cavity is used. It is noted that the resonant frequency will be changed with the variation of the geometry of cavity, since the field distribution inside the cavity is influenced by the boundaries of cavity.

4.4.2 The Slot Antenna

The geometry of a slot conformal antenna and its unit cell are shown in Figure 4.5. The cavity-backed slot antenna was subdivided into 576 elliptic-shell elements with 1261

unknowns. This cavity-backed antenna was embedded in the circular cylinder with very large radius such that it can be considered to be a rectangular cavity-backed slot antenna. Figure 4.6 shows the input impedance vs. frequency for the antenna mounted in a circular cylinder with a radius of 100 cm. Ideally, both the resistance and reactance should exhibit symmetry about the resonant frequency, and the reactance at resonance should equal zero [31]. Thus the resonance associated with zero reactance can be determined from the computed results. In Figure 4.6 it can be observed that the magnitude of the resistance increases as resonance is approached and it reaches peak value at a frequency slightly prior to resonance. Physically the energy radiating out of a slot antenna reaches its maximum at resonance. The reactance is negative across the frequency band, which implies that this cavity-backed slot antenna can be viewed as an energy-stored antenna, like a capacitor. To observe the influence of curvature variance on the input impedance, the slot antenna was mounted in different circular cylinders with radii of 5 cm, 10 cm and 30 cm. Figures 4.7 and 4.8 show that both the resonant frequency and the peak values of input resistance and reactance increase as the radius of the cylinder is decreased.

Therefore, the resonant input impedance and resonant frequency is curvature-dependent.

For the slot antenna mounted on an elliptic cylinder with major axis $a=50$ cm and minor axis $b=25$ cm, computation results associated with different locations on the elliptic cylinder are shown in Figures 4.9 and 4.10. From these results, when the antenna is embedded in the elliptic cylinder starting from $\nu_0 \approx 0$, which is a highly curved region, the resonant frequency is 4.875 GHz and its resonant input resistance is 584 Ω . When the antenna is moved to a region with little curvature change (i.e. $\nu_0 \approx \frac{\pi}{6}$), f_r shifts to 4.825

GHz, and the resonant input resistance remains almost unchanged. At $\nu_0 \approx \frac{\pi}{2}$, the quasi-planar portion of surface, the resonant frequency is 4.80 GHz and the resonant input resistance decreased to 505 Ω . From the analysis above, it can be observed that the resonant frequency and input impedance vary in regions of highly changing curvature.

4.4.3. The Conformal Patch Antenna

Cavity model has been used to analyze field structure inside a rectangular patch antenna with very thin substrate layer very well. Since the height of the substrate is very small, the fields remain constant along the height. In addition, because of the very small substrate height, the fringing of the fields along the edges of the patch are also very small whereby the electric fields is nearly normal to the surface of the patch. Therefore, only TM mode will be concerned within cavity. In this cavity model the top and bottom walls of the cavity are perfectly electric conducting, the four-side walls will be modeled as perfectly conducting magnetic walls. The two most important field modes are TM_{010} and TM_{001} associated with the azimuthal and axial polarization for the rectangular microstrip patch antennas. The field structure for TM_{010} and TM_{001} is shown in Figure 4.11. For TM_{010} , the equivalent magnet current due to the electric fields will exist on all four slot-like walls; however only two walls, referred as radiating slots, that are separated by the length, L, will radiate power outward. The radiation from the other two side walls separated by width, W, is small compared to the other two side walls. Therefore, these two slots are usually referred to as non-radiating slots.

Figure 4.12 to Figure 4.15 show the input impedance vs. frequency for the patch antenna with the azimuthal polarization when the probe feed is removed from the center of the patch to the edge. Figure 4.12, which corresponds to the probe feed located at the center of the patch, shows that TM_{010} is not excited. The input impedance increases as the probe feed moving along the azimuthal central line and away from the center of the patch. Figure 4.15 shows the input impedance reaches maximum when the probe feed is placed right on the edge of the patch.

Figure 4.16 shows the geometry of the patch antenna and its unit cell that are used for computation using the elliptic cylinder FE-BI and LMBRICK codes. The cavity-backed patch antenna was meshed into 192 elements with 411 unknowns. For the probe feed located 0.5 cm left of center, referred as azimuthal polarization, a quasi-planar surface is considered here. The input impedance vs. frequency is shown in Figure 4.17. Figure 4.17 exhibits very good agreement between the computed results using the elliptic cylinder FE-BI method and the planar LMBRICK codes.

For the same patch antenna with the different cavity size of 0.0795 cm x 6.5 cm x 5.5 cm, the cavity-backed patch antenna was mesh into 572 elements with the total unknowns of 1209 and the unit length of about $1/40\lambda$ in axial and azimuthal direction for each cell. For the axial polarization, which probe feed is placed at 1.0 cm below the center of the patch, the input resistance and reactance vs. frequency is plotted as Figure 4.18 and 4.19, respectively. Here the dielectric constant $\epsilon_r = (2.32, 0.0)$ was used. In Figure 4.18 and 4.19, it is observed that the input impedance and resonant frequency are almost independent of curvature while the magnitude of the input impedance very slightly decreases as the radius of circular decreases. For the axial polarization the

TM_{001} is excited here, and because the field remains constant along length or the azimuthal direction, shown in Figure 4.11, it can be observed that the field structure is not disturbed due to the surface curvature along azimuthal direction. Therefore, for the axial polarization the input impedance and resonant frequency are almost independent of curvature. The threshold chosen for using curved dyadic Green's function or planar dyadic Green's function in boundary integral computation is based on the geodesic path that the wave travels. For a curved surface, the curved dyadic Green's function is applied to computation when the wave travels more than half wavelength, while the planar dyadic Green's function is used when the distance between the source and test point is less than half wavelength.

The results for the azimuthal polarization, which the probe feed is placed 1.25 cm to the left of the center of the patch are shown in Figure 4.20 and 4.21. In Figure 4.20 and 4.21, it can be observed that for the patch antenna with azimuthal polarization, the resonant frequency is sensitive to the variation of curvature. The input impedance almost remains unchanged while the resonant frequency shifts to right when the radius of the cylinder decreased from 500.0 cm to 15.0 cm and 10.0 cm. Since the TM_{010} is excited here, and because the field is varying sinusoidally along length or along the azimuthal direction as shown in Figure 4.11, it can be observed that the field structure is easier disturbed due to the surface curvature along azimuthal direction. Therefore, for the azimuthal polarization, the resonant frequency is more dependent on curvature compared to axial polarization. It is also noted that the bandwidth of the patch antenna remained unchanged no matter axial or azimuthal polarization is applied. Also, the resonant input

reactance is approximately zero for both cases, which implies that this cavity-backed patch antenna is not an energy-stored antenna like the slot antenna.

To ensure that the curvature dependence of the resonant frequency for patch antenna with azimuthal polarization is dependant of the field mode excited beneath the patch rather than the geometry of the patch size, now a square patch of 3.0 cm X 3.0 cm with azimuthal polarization is examined. The input resistance and reactance vs. frequency are shown in Figure 4.22 and 4.23. In Figure 4.22 and 4.23, the similar results of the input impedance vs. frequency are observed. Therefore, it can be concluded that the field mode that was excited inside the cavity decides whether the resonant frequency is curvature dependent or not.

If the patch antenna is flush-mounted on different portions of an elliptic cylinder with $a=30.0$ cm and $b=15.0$ cm and the probe feed is placed 1.0 cm to the left of the center point of patch, similar results are obtained as the previous paragraph. The numerical results are shown in Figure 4.24 and 4.25. Based on the variation of the surface curvature for a conformal antenna embedded in an elliptic cylinder, an approximate equivalent circular cylinder can be determined. It can be concluded that for the conformal patch antenna mounted on a surface with a high curvature, the input impedance is much more sensitive to the variation of curvature than in a region of low curvature. That can be used to explain why the performance of the conformal antenna embedded in a region with little curvature variation can be approximated by its equivalent circular cylinder, but such an approximation fails for the case of an antenna embedded in a surface with significant curvature variation.

4.5. Conclusion

In this chapter, from the numerical results and discussion above, it is demonstrated that the exterior and interior portions of a hybrid finite element-boundary integral computer program have been validated for an empty cavity, conformal slot antenna, and conformal patch antenna. In the next chapter, multiple patch antennas embedded on an elliptic cylinder will be studied to assess the effects of mutual coupling between patch antennas mounted on surfaces with varying curvature.

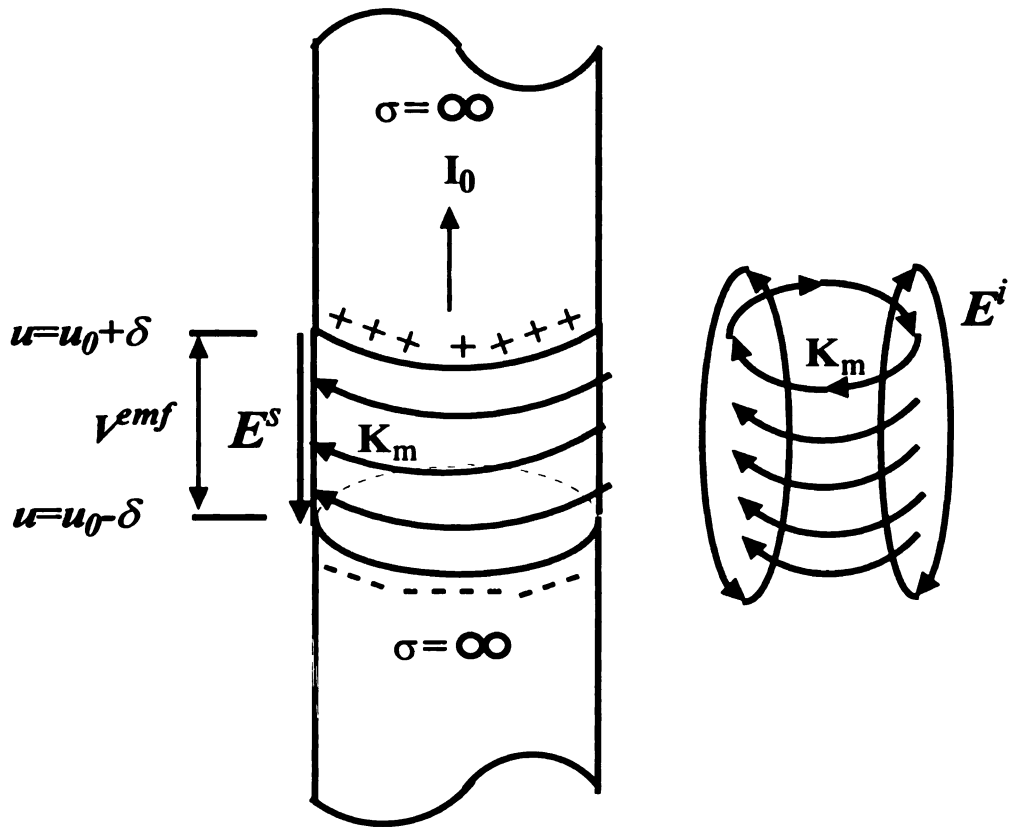
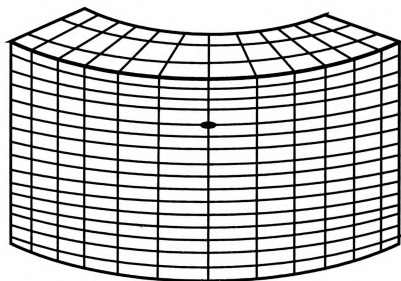


Figure 4.1 .The geometry of model of source generator.

Empty Cavity



Unit Cell

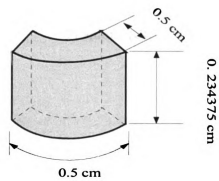


Figure 4.2 An empty cavity: 1.5 cm x 6.0 cm x 3.75 cm and its unit cell.

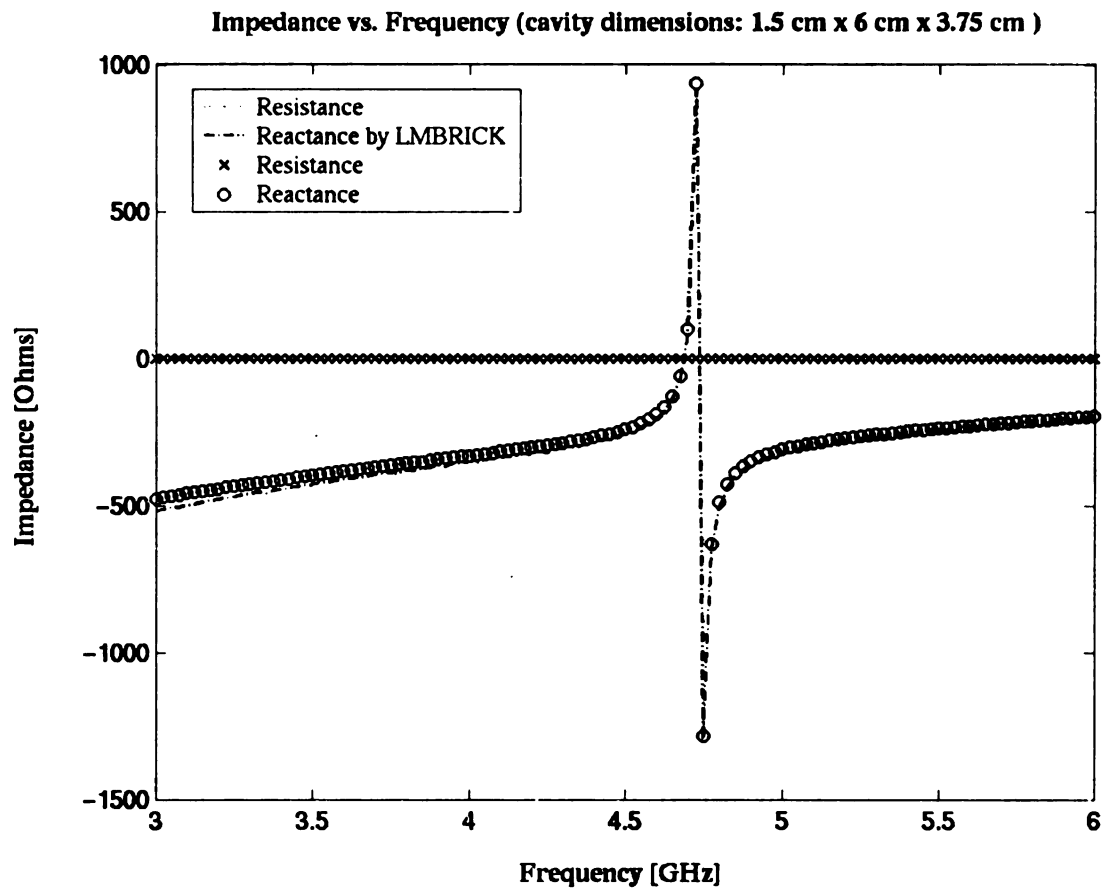


Figure 4.3 Input impedance for an empty cavity mounted in the ground.

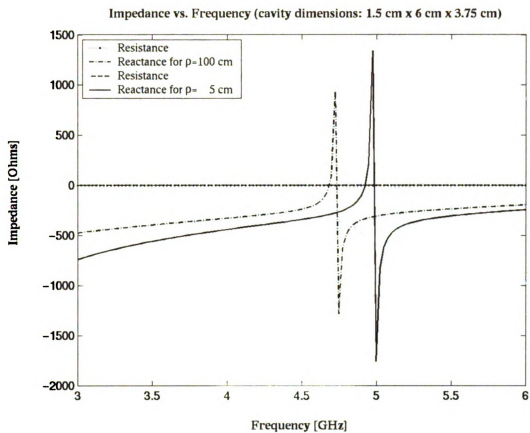
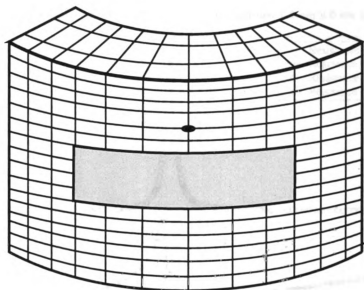


Figure 4.4 Input impedance for an empty cavity mounted in two circular cylinders with different radii.

Slot Antenna



Unit Cell

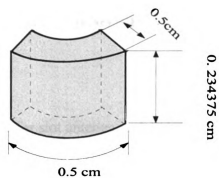


Figure 4.5 Slot antenna: 1.5 cm x 6.0 cm x 3.75 cm and its unit cell.

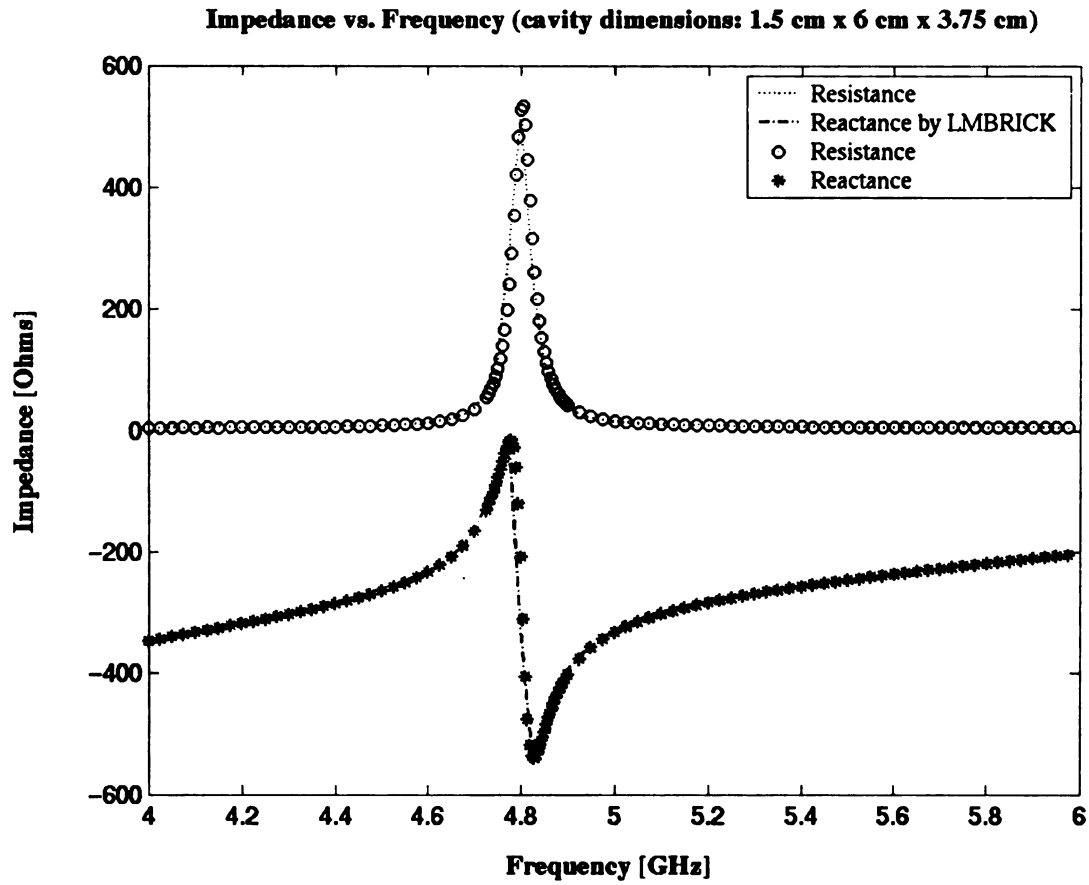


Figure 4.6 Input impedance for slot antenna embedded in a ground plane;
 $\epsilon_r = 1 - j0.01$, $u_r = 1.0$.

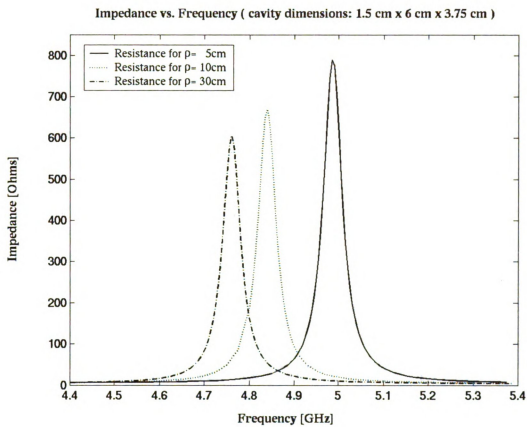


Figure 4.7 Input resistance for slot antenna on cylinders; $\epsilon_r = 1 - j0.01$, $u_r = 1.0$.

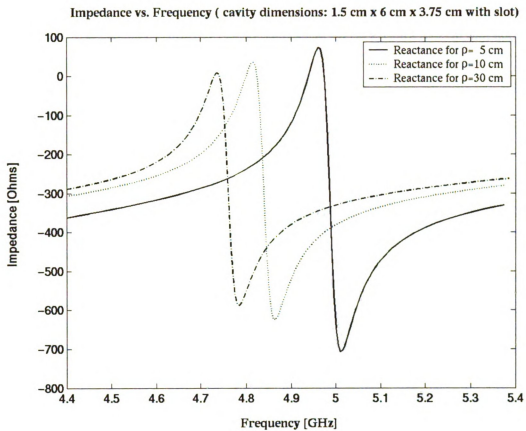


Figure 4.8 Input reactance for slot antenna on cylinders; $\epsilon_r = 1 - j0.01$, $u_r = 1.0$.

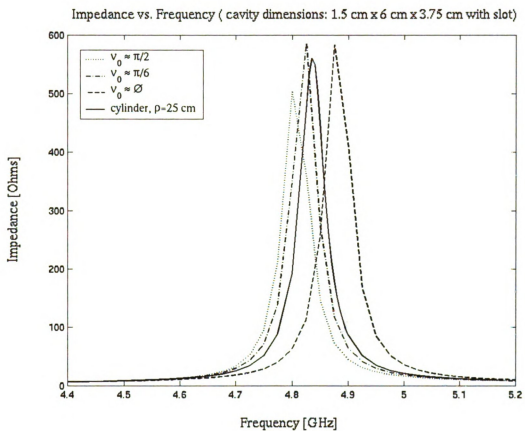


Figure 4.9 Input resistance for slot antenna on cylinder and elliptic cylinder with $a=50$ cm, $b=25$ cm; $\epsilon_r = 1 - j0.01$, $u_r = 1.0$.

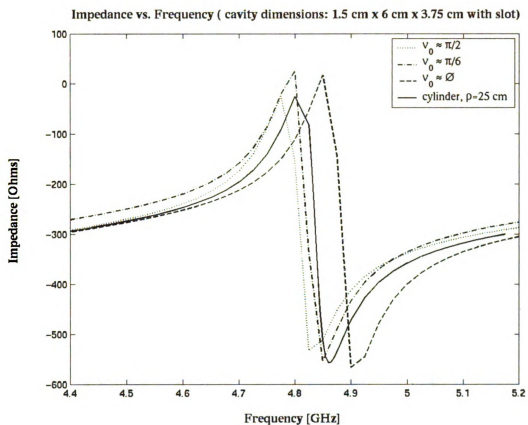


Figure 4.10 Input reactance for slot antenna on cylinder and elliptic cylinder with $a=50$ cm, $b=25$ cm, $\epsilon_r = 1 - j0.01$, $u_r = 1.0$.

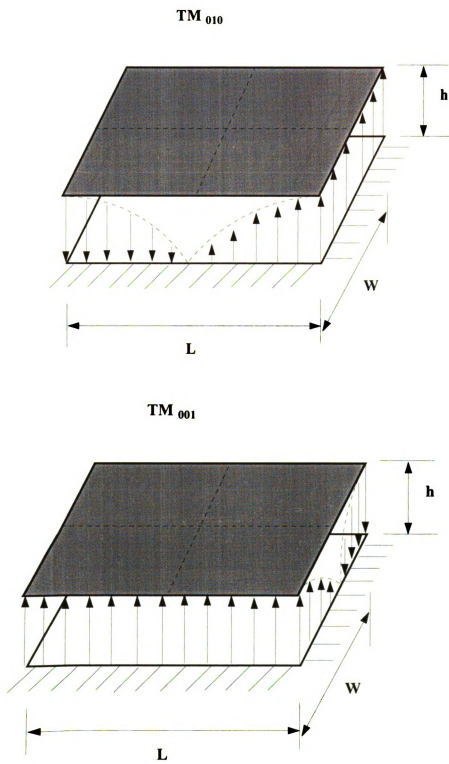
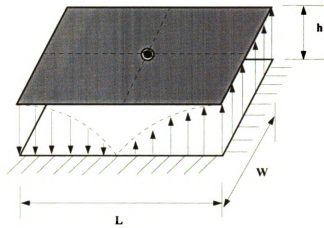


Figure 4.11 Fields configurations (modes) for rectangular microstrip patch.

TM₀₁₀



$h=0.011$ cm
 $L=4.0$ cm
 $w=3.0$ cm

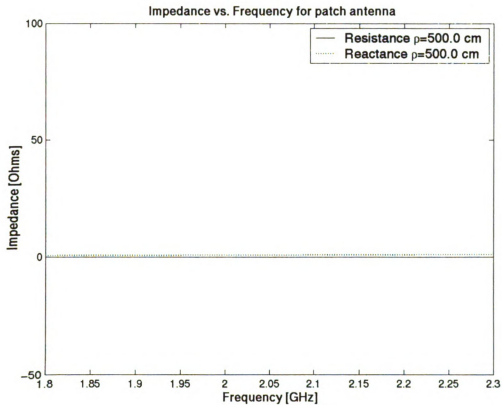


Figure 4.12 Input impedance for the rectangular patch antenna embedded in a ground plane.

TM 010

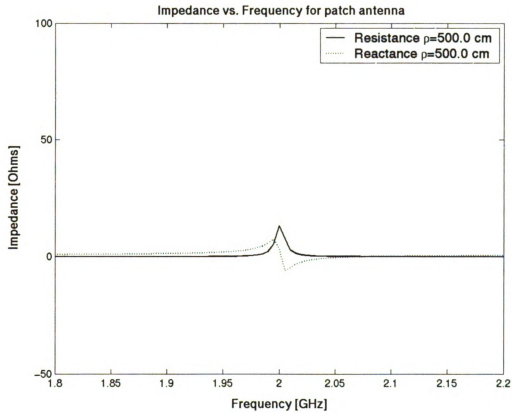
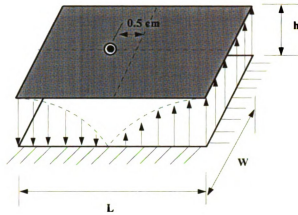


Figure 4.13 Input impedance for the rectangular patch antenna embedded in a ground plane; $\epsilon_r = 3.29 - j0.01316$, $u_r = 1.0$.

TM₀₁₀

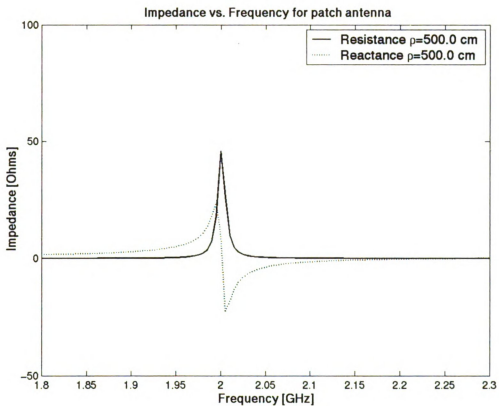
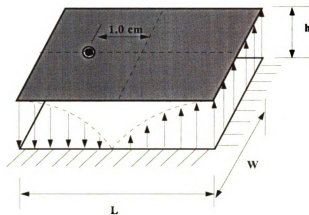


Figure 4.14 Input impedance for the rectangular patch antenna embedded in a ground plane; $\epsilon_r = 3.29 - j0.01316$, $u_r = 1.0$.

TM₀₁₀

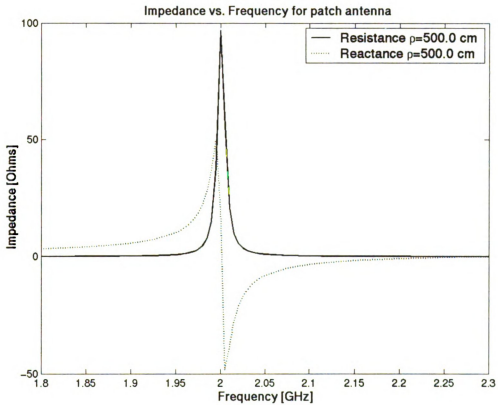
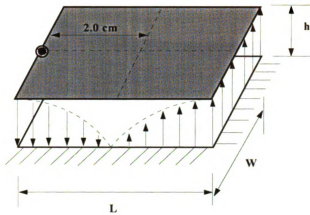
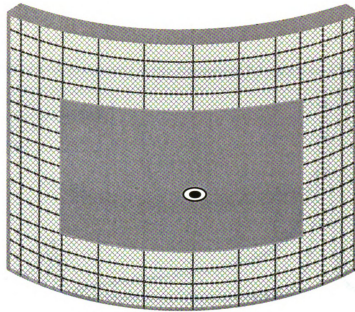


Figure 4.15 Input impedance for the rectangular patch antenna embedded in a ground plane; $\epsilon_r = 3.29 - j0.01316$, $\mu_r = 1.0$.

Cavity: 0.1 cm x 6.0 cm x 8.0 cm
Patch: 3.0 cm x 4.0 cm



Unit Cell

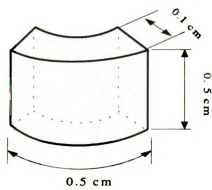


Figure 4.16 Patch antenna: 1.5 cm x 6.0 cm x 3.75 cm.

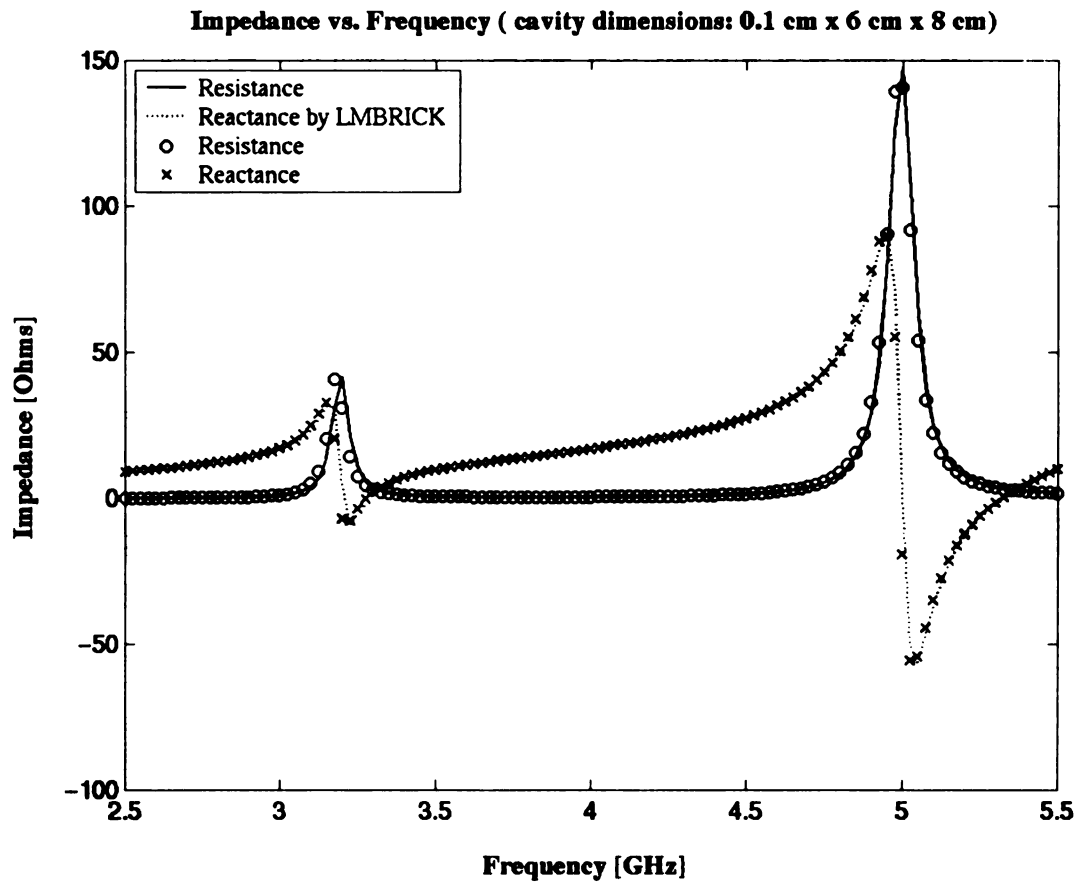


Figure 4.17 Input impedance for a patch antenna in a ground plane; $\epsilon_r = 2.0$, $u_r = 1.0$.

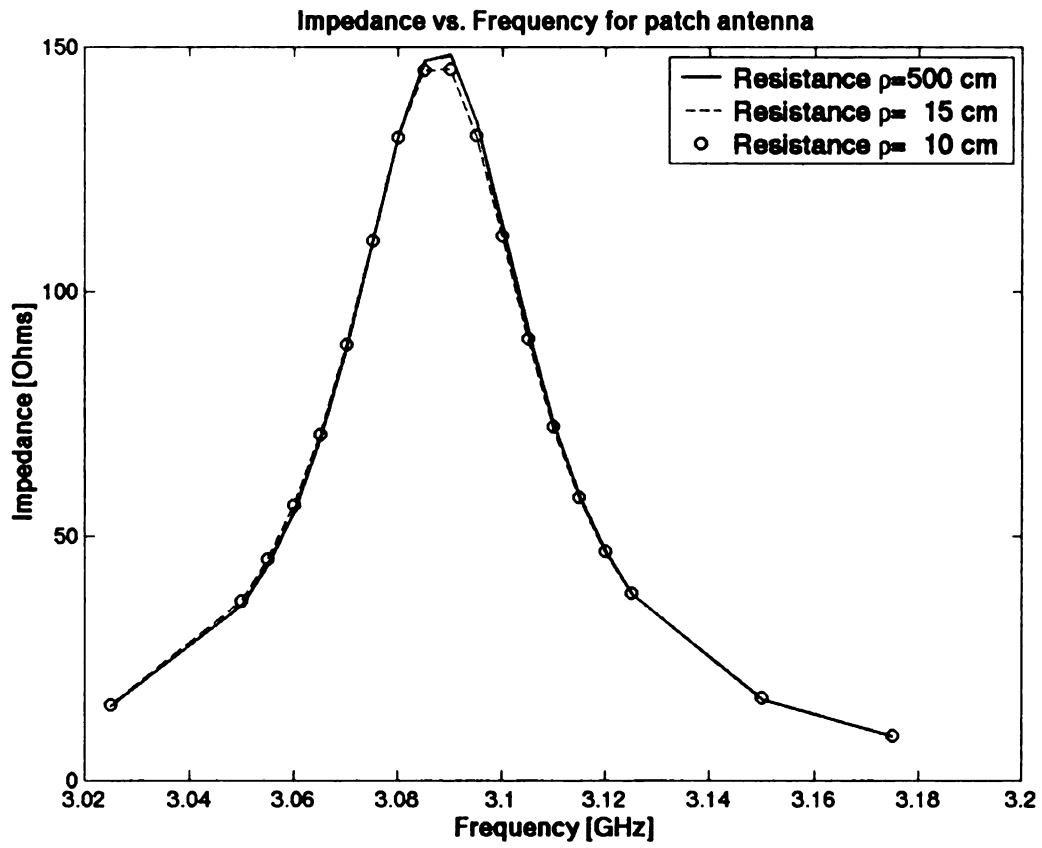


Figure 4.18 Resistance for a patch antenna on cylinders; $\epsilon_r = 2.32 - j0.0$, $u_r = 1.0$.

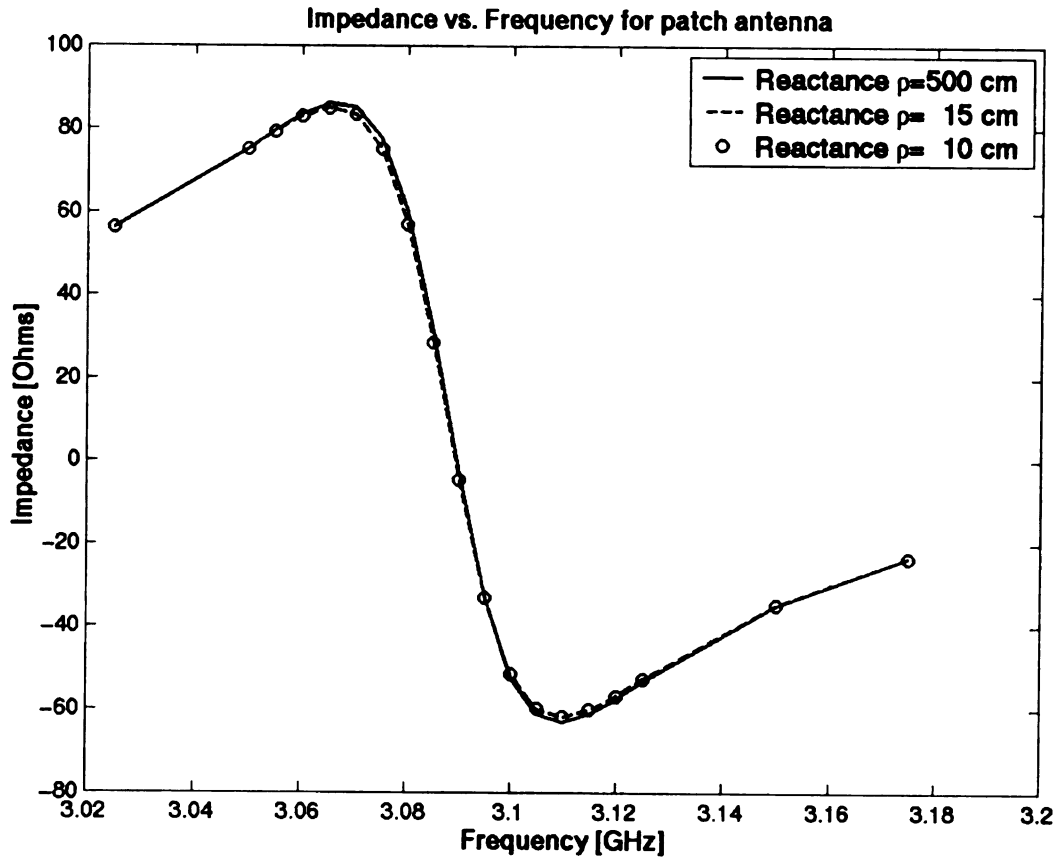


Figure 4.19 Reactance for a patch antenna; $\epsilon_r = 2.32 - j0.0$, $u_r = 1.0$

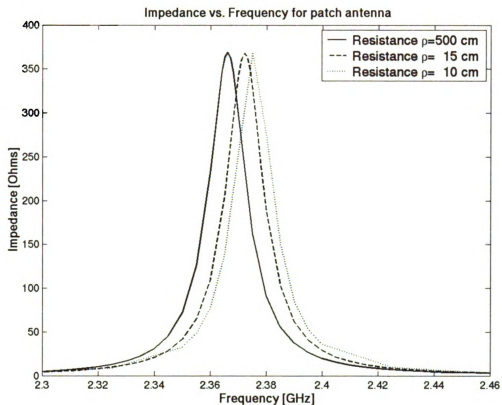


Figure 4.20 Resistance for a patch antenna with probe feed located at $(-1.25, 0.0)$ and patch size of 4.0 cm \times 3.0 cm; $\epsilon_r = 2.32 - j0.00$, $u_r = 1.0$.

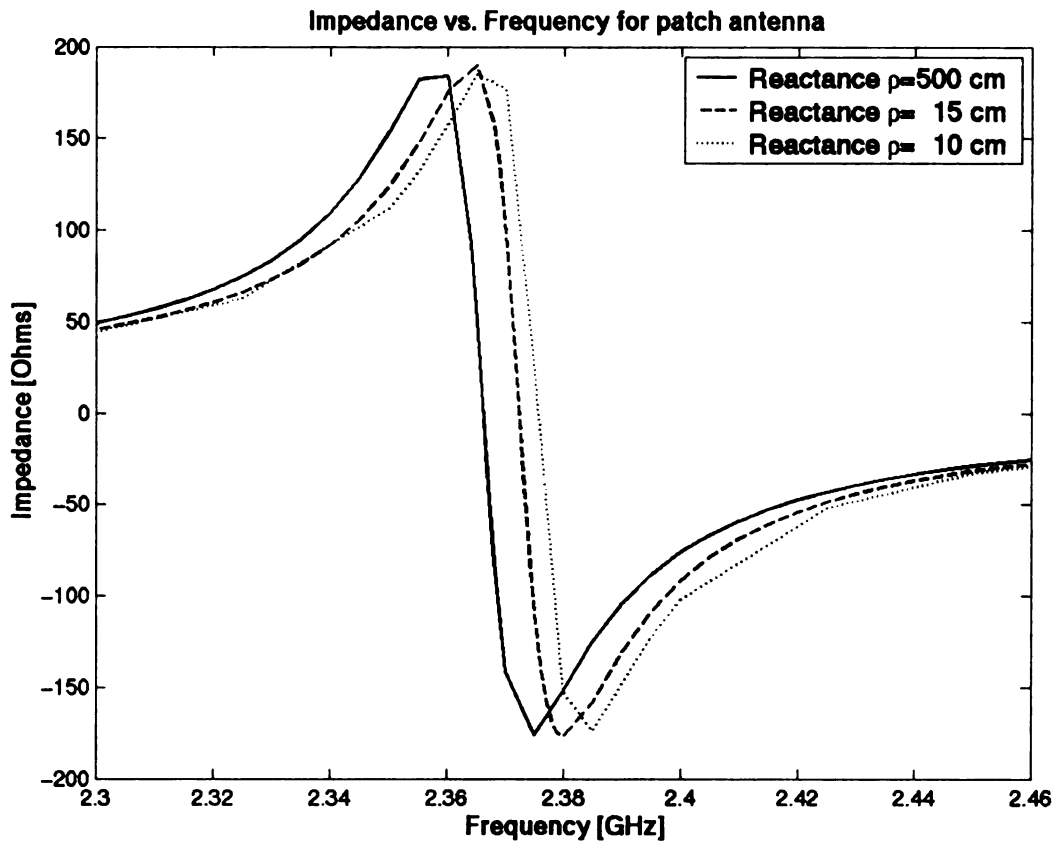


Figure 4.21 Reactance for a patch antenna with probe feed located at $(-1.25, 0.0)$ and patch size of 4.0 cm \times 3.0 cm, $\epsilon_r = 2.32 - j0.00$, $u_r = 1.0$.

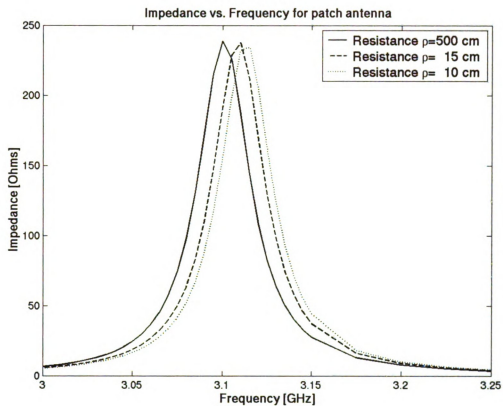


Figure 4.22 Resistance for a patch antenna with probe feed located at $(-1.0, 0.0)$ and patch size of $3.0 \text{ cm} \times 3.0 \text{ cm}$; $\epsilon_r = 2.32 - j0.00$, $u_r = 1.0$.

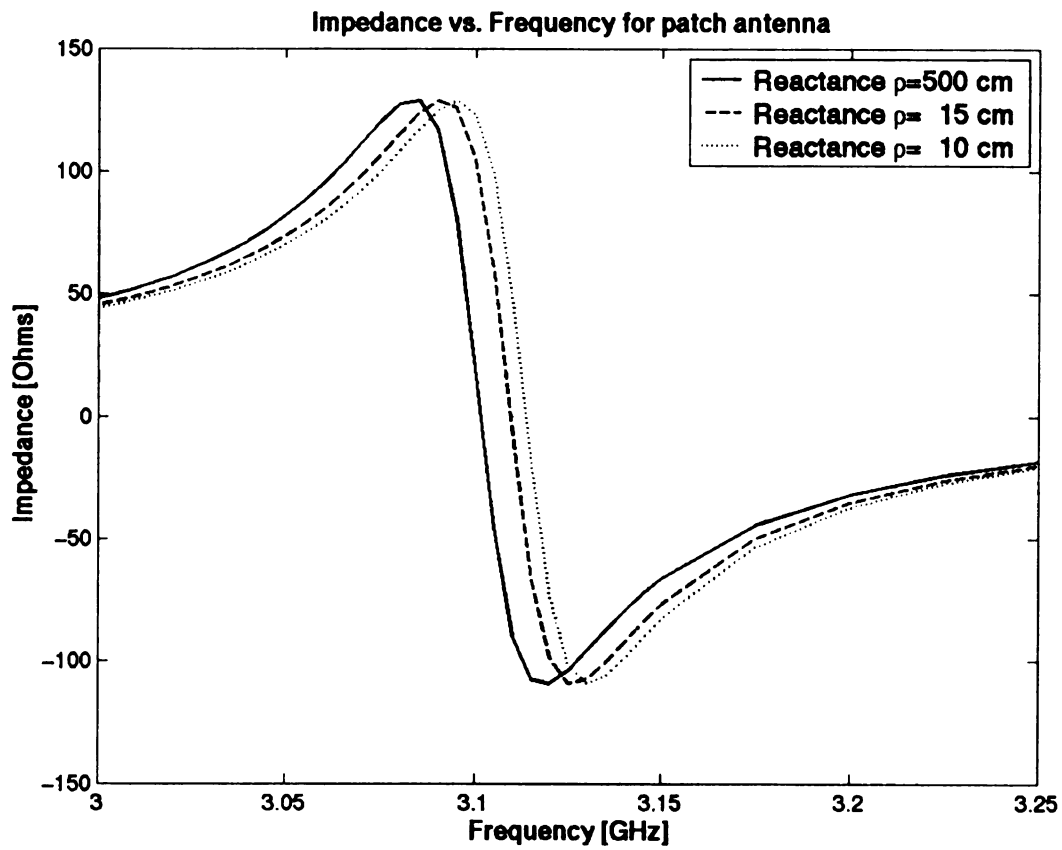


Figure 4.23 Reactance for a patch antenna with probe feed located at (-1.0, 0.0) and patch size of 3.0 cm x 3.0 cm; $\epsilon_r = 2.32 - j0.00$, $u_r = 1.0$.

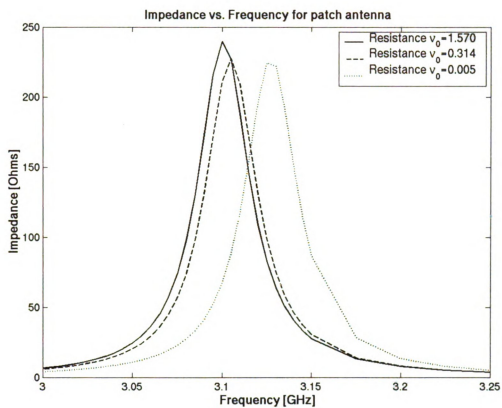


Figure 4.24 Resistance for a patch antenna with patch size of 3.0 cm x 3.0 cm mounted in an elliptic cylinder; $\epsilon_r = 2.32 - j0.0$, $\mu_r = 1.0$.

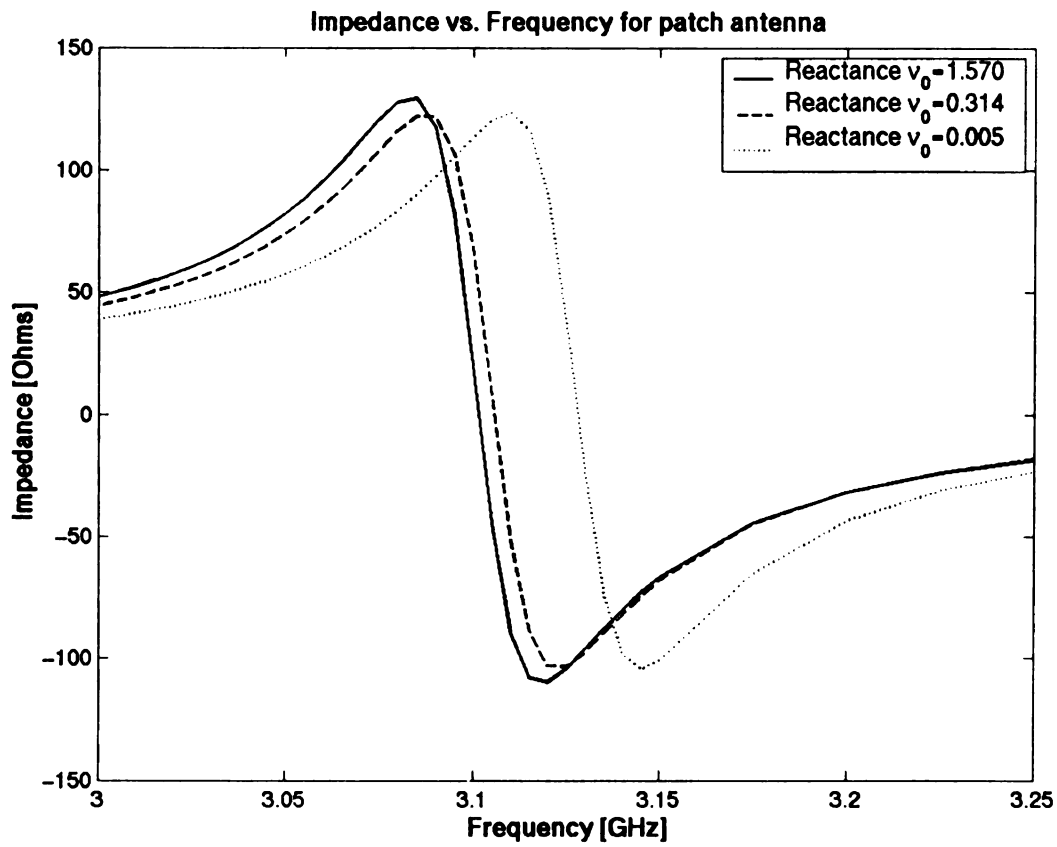


Figure 4.25 Reactance for a patch antenna with patch size of 3.0 cm x 3.0 cm mounted in an elliptic cylinder; $\epsilon_r = 2.32 - j0.0$, $u_r = 1.0$.

CHAPTER 5

MUTUAL COUPLING BETWEEN MICROSTRIP ANTENNA

5.1 Introduction

The mutual coupling between microstrip antennas mounted in a ground plane and in circular and elliptic cylinders is investigated in this chapter. A moment method solution to the microstrip antenna problem was proposed [13] in 1981 and the mutual coupling between patch antennas embedded on the ground plane with infinite extended substrate was calculated and measured by Pozar [14] and Carver [15], respectively. In this chapter, the numerical results using FE-BI method are compared with these moment method results.

The mutual coupling between patch antennas embedded in circular cylinders with different radii is calculated in this chapter. The mutual resistance, reactance and coupling coefficient, S_{12} , are plotted with respect to frequency to analyze the effects of curvature on coupling. Also, the same antenna is mounted on different portions of the elliptic cylinder, corresponding to different local curvature, and the computed results are discussed. The field structure is primarily determined by the position of the probe feed, and the feed location is found to impact the mutual coupling. Therefore, the probe feed is relocated and numerical results for coupling for various feed configurations are inspected to assess the influences of the location of the probe feed on mutual coupling.

In addition to curvature, the position of the probe feed, the size of patches and the distance between the two rectangular patches play an important role in mutual coupling. In this chapter, the various patch dimensions are used to analyze the effects of patch size on mutual coupling. Also, the numerical results are computed for the antenna mounted in

circular cylinders with different radii. For convenience, symmetric patches are used in the examples.

In this chapter, a two-port network model is used to determine mutual coupling. The coupling parameter S_{12} is determined from the input impedance and coupled impedance using conversion between S -parameters and Z -parameters.

5.2. Mutual Coupling

To analyze coupling between the two probe fed microstrip antennas, a two-port network representation is used. The relation between the port voltages and currents are defined as

$$\begin{bmatrix} V_1 \\ V_2 \end{bmatrix} = \begin{bmatrix} Z_{11} & Z_{12} \\ Z_{21} & Z_{22} \end{bmatrix} \begin{bmatrix} I_1 \\ I_2 \end{bmatrix} \quad (5.1)$$

The self-input impedance Z_{11} and Z_{22} can be determined using (4.7), giving

$$\begin{aligned} Z_{11} &= \frac{-\int_V \mathbf{E}^{(1)} \cdot \mathbf{J}_i^{(1)} dV}{I_0^2} \\ Z_{22} &= \frac{-\int_V \mathbf{E}^{(2)} \cdot \mathbf{J}_i^{(2)} dV}{I_0^2} \end{aligned} \quad (5.2)$$

where $\mathbf{E}^{(1)}$ are the electric fields due to the source current $\mathbf{J}_i^{(1)}$ at port one when the source at port two $\mathbf{J}_i^{(2)}$ is turned off, and $\mathbf{E}^{(2)}$ is the electric field due to the source current $\mathbf{J}_i^{(2)}$ at port two when the source at port one is turned off. The coupling impedance Z_{21} can be determined by the following relationship,

$$\begin{aligned}
Z_{21} &= \frac{-1}{I_0^2} \int_V \mathbf{E}^{(2)} \cdot \mathbf{J}_i^{(1)} dV = \frac{-1}{I_0^2} \int_V (\mathbf{E}' - \mathbf{E}^{(1)}) \cdot \mathbf{J}_i^{(1)} dV \\
&= \frac{-1}{I_0^2} \int_V \mathbf{E}' \cdot \mathbf{J}_i^{(1)} dV - \frac{1}{I_0^2} \int_V \mathbf{E}^{(1)} \cdot \mathbf{J}_i^{(1)} dV \\
&= Z_1 - Z_{11}
\end{aligned} \tag{5.3}$$

where \mathbf{E}' is the total electric field due to both $\mathbf{J}_i^{(1)}$ and $\mathbf{J}_i^{(2)}$. Also, Z_1 is the impedance when both $\mathbf{J}_i^{(1)}$ and $\mathbf{J}_i^{(2)}$ are used. Generally, $Z_{12} = Z_{21}$. For simplicity, a unit current is used for I_0 here. It is noted that the self-input impedance of port one is equal to that of port two ($Z_{11} = Z_{22}$) when the two patches are symmetrically located. For microstrip antennas mounted on an elliptic cylinder, if the two patches are placed in regions with different surface curvature, then $Z_{11} \neq Z_{22}$ even if the two patches have the same area.

The coupling parameter S_{12} is determined from the following formulation [32]

$$S_{12} = \frac{2Z_{12}Z_0}{(Z_{11} + Z_0)(Z_{22} + Z_0) - Z_{12}Z_{21}} \tag{5.4}$$

where Z_0 is 50Ω here.

5.3. Numerical Results and Discussions

The calculation results of the mutual impedance between two coax-fed microstrip antennas are shown in this section. Several characteristics of the microstrip antenna are observed from the presented calculations. The E-plane and H-plane are associated with the arrangement of the patches and the location of the probe feed and are used here to facilitate comparison with reference data. The distance between patches is varied to observe the influence of separation on mutual coupling and resonant frequency. Also, the effects on coupling due to the surface curvature are checked by applying several

scenarios of antennas mounted on differing circular cylinders and on different portions of the elliptic cylinder.

Since the patch size of the microstrip antenna plays an important role not only on the strength of the surface wave being excited, but also on the resonant frequency of the antenna, the computations presented also include several scenarios for observing the influence due to the patch size.

5.3.1 Comparisons between FE-BI and Moment Method for H-Plane Coupling

For a microstrip antenna embedded on a plane ground coated with substrate, the mutual coupling between patch antennas has been presented by Pozar [14] in 1982. In that paper, a moment method solution using the rigorous dielectric slab Green's function is presented. Also, the measured results were published in 1981 by Carver [15]. The geometry of two rectangular microstrip patches is shown in Figure 5.1 and the results for mutual coupling vs. $\frac{s}{\lambda_0}$ are shown in Figure 5.2, where s is the distance between the patches. Figure 5.2 presents good agreement for mutual coupling (S_{12}) data comparing measurements and computed results using a moment method solution for two coax-fed microstrip antennas.

To verify the FE-BI method presented in this dissertation, comparisons are made with the results shown in Figure 5.2. The microstrip antenna was mounted on a circular cylinder with a very large radius so that the antenna can be considered mounted on a ground plane. For H-plane coupling, the geometry in Figure 5.3 is used. The size of cavity is 0.1588 cm x 35 cm x 24 cm. The size of each rectangular patch is $W=10.0$ cm and $L=6.0$ cm. The cavity-backed antenna was meshed into 420 elements with 1021

unknowns using a unit cell with dimensions 0.1588 cm x 1 cm x 2 cm. The dielectric constant of the cavity was $\epsilon_r = 2.55$. The mutual coupling, S_{12} , vs. $\frac{s}{\lambda_0}$ is shown in Figure 5.4. In Figure 5.4 the coupling computed using FE-BI is greater than that using a moment method solution. Physically since the aperture in FE-BI is not electrically large, there are interactions between the fields and the cavity walls that impact the mutual coupling. Such boundary conditions are not present in the moment method model. The size of the cavity is not sufficiently large so that the antenna fields damp out enough before hitting the walls of the cavity. The other reason for this deviation may be coming from the position of the probe feed. If the center point of each patch on the aperture is considered as origin, then the position of the probe feed in Pozar's computation is on the central axial line and probably slightly above the lower edge of the patch. In comparison, the location of the probe feed for the FE-BI method is on the central line but 1 cm above the lower edge of the patch.

To improve the agreement illustrated in Figure 5.4, the dimensions of the cavity are extended to 0.1588 cm x 53 cm x 30 cm while the patch size remains the same. The total elements and unknowns are increased to 795 and 2104, respectively and each unit cell remains the same size of 0.1588 cm x 1 cm x 2 cm. The comparison for mutual coupling using FE-BI with a moment method solution and measured data is shown in Figure 5.5. In this figure, it is observed that the agreement between the measured data and the FE-BI computed results have improved.

For convenience, the FE-BI results in Figure 5.5 and 5.4 are presented together in Figure 5.6. In Figure 5.6, it is observed that mutual coupling contributed from the standing wave becomes important when the separated distance, s , increases. This

indicates that the reflective fields become the dominant coupling mechanism for coupling when the antenna separation increases. Meanwhile, the direct fields attributed to coupling become weaker. On the other hand, when the separation becomes smaller, the deviation between these two computed results reduces. At that time the direct fields are dominant for the mutual coupling.

Next, the position of the probe feed is relocated to the central axial line on the lower edge. An illustration of this geometry is shown in Figure 5.7. The numerical results are shown in Figure 5.8. Figure 5.8 illustrates the good agreement between the FE-BI solution, moment method solution, and measured data.

The resonant frequency found using the FE-BI method is 1.34 GHz, which is less than the 1.410 GHz computed by a moment method solution. Theoretically, for H-plane coupling, since the patch length $L=6$ cm used for FE-BI computation is shorter than $L=6.55$ used in a moment method solution, the resonant frequency should be higher than 1.410 GHz. Therefore, there is some accuracy problem arising from cavity meshing for the FE-BI model. To improve accuracy, a new cavity of 0.1588 cm x 51 cm x 16 cm is created and meshed finer into 832 elements with 2101 unknowns and with unit cell dimensions of 0.1588 cm x 1 cm x 1 cm. The computed results are shown in Figure 5.9 and the resonant frequency is 1.430 GHz, which is slightly higher than 1.410 GHz computed by a moment method solution. For convenience, the results for both cases, in which the probe feed is placed in the axial central line of the patch and 1 cm above the lower edge and right on the lower edge, are shown in Figure 5.9. Figure 5.9 shows a good agreement between the computation results and measured data.

5.3.2 Comparisons between FE-BI and Moment Method for E-Plane Coupling

For E-plane coupling, the cavity-backed antenna with a 0.1588 cm x 35 cm x 30 cm cavity was used as shown in Figure 5.10. It was meshed into 1050 elements with 2749 unknowns with unit cell dimensions of 0.1588 cm x 1 cm x 1 cm. The position of the probe feed was placed in two different locations. One was on the horizontal central line of the patch and along the right edge of the patch (i.e. FE-BI case (1) in Figure 5.11) while the other was on the horizontal central line of the patch and 1 cm left of the right edge (i.e. FE-BI case (2) in Figure 5.11). The computed results are shown in Figure 5.11. Good agreement between computed results using the FE-BI model, a moment method solution, and measured data is achieved except for the case with a very small separation between the two rectangular patches, i.e. $\frac{s}{\lambda_0} < 0.2$. Here the resonant frequency is the same as H-plane coupling, i.e. $f_r = 1.430$ GHz. Also, the resonant frequency is independent of the position of the probe feed as long as the probe feed is located on the central line of the patch, since such a feed location excites a single mode. For the case with $\frac{s}{\lambda_0} < 0.2$, the patch antennas are so close to each other such that the fields dramatically vary with respect to position in the cavity. Hence the finer meshing of the antenna geometry is required for the FE-BI method to accurately compute the fields inside the cavity and upon the aperture. A cavity-backed antenna with a 0.1588 cm x 20 cm x 14 cm cavity was meshed into 1120 elements with 2201 unknowns with unit cell dimensions of 0.1588 cm x 0.5 cm x 0.5 cm. A probe feed was placed on the horizontal central line of the patch and along the right edge of the patch (i.e. FE-BI case (1) in

Figure 5.12) while the other was on the horizontal central line of the patch and 1 cm left of the right edge (i.e. FE-BI case (2) in Figure 5.12). The computed results are shown in Figure 5.12. Good agreement between computed results using the FE-BI model, a moment method solution, and measured data is achieved even for the case with a very small separation between antennas.

In Figure 5.9 for the H-plane coupling and Figure 5.12 for the E-plane coupling, it is concluded that the mutual coupling level decreases monotonically with increasing separation between patches. The difference in the mutual coupling between the E-plane and H-plane coupling increases as separation increases. This difference in mutual coupling increases from 3 dB for $\frac{s}{\lambda_0} = 0.125$ to 11 dB for $\frac{s}{\lambda_0} = 0.75$. For E-plane coupling the mutual coupling is higher than that for the H-plane coupling. Physically, this is because the surface waves and creeping waves are stronger in the E-plane case.

From the numerical results and discussions above, it is concluded that the cavity size should be made large enough to ensure that there is no interaction between fields and wall boundary to contribute to increase mutual coupling. Then the case of a patch on the top of the infinite extended substrate could be approximated. However, in practice operational concerns dictate the smallest cavity possible and hence the need for an FE-BI model to assess the design trade-offs inherent in such designs. Also, the cavity should be subdivided into finer elements with an edge length of $\frac{\lambda}{20}$ to achieve greater accuracy.

For E-plane coupling case with $\frac{s}{\lambda_0} < 0.2$, the length of unit cell should be less than $\frac{\lambda}{40}$ to have a reliable computed results.

The numerical results from the FE-BI method have shown a very good agreement with a moment method solution and measured data for E-plane and H-plane coupling between the microstrip antennas mounted on the ground plane. In the next section a microstrip antenna will be embedded in a surface with curvature to see the effects on mutual coupling by the surface curvature.

5.3.3 Numerical Results and Discussions for H-Plane Coupling on a Curved Surface

In section 5.3.2 and 5.3.3 the computed results of E-plane and H-plane coupling for two microstrip antennas mounted in a ground plane were presented. In this section, microstrip antennas mounted on surfaces with different curvatures are used to analyze the variation of the mutual coupling with respect to the surface curvature.

The geometry of a microstrip antenna mounted in a curved surface with two identical 3 cm x 3 cm patches is shown in Figure 5.13. For this case the two probe feeds are placed in the locations corresponding to 0.5 cm below the center point of each patch and along the central line. This cavity-backed patch antenna was meshed with 200 elements consisting of 373 unknowns and with unit cell dimensions of 0.1 cm x 0.5 cm x 0.5 cm. The mutual resistance and reactance versus frequency for an antenna mounted in different circular cylinders with radii of 25 cm, 50 cm and 100 cm are shown in Figure 5.14 and 5.15, respectively. The mutual coupling (S_{12}) vs. frequency is shown in Figure 5.16. From Figure 5.14 and 5.15, the mutual resistance and reactance have greater variation around the resonance when the antenna is mounted on the cylinder with less curvature. This is because the surface wave being excited on a surface with less curvature has little energy shedding away from the surface and more energy can reach the other

patch, resulting in greater mutual coupling. In Figure 5.16 it can be observed that the peak value of mutual coupling occurs at resonance since at this frequency the maximum energy is radiated from the patch antenna. Also, the difference in the magnitude of mutual coupling for the antenna mounted in the cylinder with $\rho = 100$ cm and $\rho = 25$ cm is about 10 dB. For an antenna mounted in a region with high curvature, the surface wave has greater energy loss due to the fields shedding away from the surface, thus H-plane coupling demonstrates lower mutual coupling for the case with $\rho = 25$ cm.

For the same microstrip antenna mounted in an elliptic cylinder with major axis $a=50$ cm and minor axis $b=25$ cm, computed results for mutual resistance, reactance and coupling associated with different locations on the elliptic cylinder are shown in Figure 5.17, 5.18 and 5.19. From these results, when the antenna is embedded in the elliptic cylinder starting from $\nu_0 = 0.02$, which is a highly curved region, the magnitude of the mutual resistance and reactance are much smaller compared to values for the antenna mounted in the elliptic cylinder starting from $\nu_0 = \frac{\pi}{6}$ or $\frac{\pi}{2}$ (e.g., regions with less curvature). There is little difference in the mutual coupling for the antenna mounted in the elliptic starting from $\nu_0 = \frac{\pi}{6}$ compared to $\nu_0 = \frac{\pi}{2}$. Therefore, the main variation for the coupling happens when the antenna is in a region with high curvature. For antennas mounted on both a circular cylinder and an elliptic cylinder, it can be concluded that coupling decreases with decreasing radius of curvature for H-plane coupling.

For the H-plane coupling the field in the space between the patches is primarily a TE mode and there is not as strong a dominant mode surface wave excitation; therefore there is less coupling between the patches.

5.3.4 Numerical Results and Discussions for E-Plane Coupling on a Curved Surface

The geometry of a patch antenna mounted on a curved surface with E-plane coupling between patches is shown in Figure 5.20. Here two coaxial probe feeds are located 0.5 cm to the left of the center point of each patch and along the central line of the patch. The cavity-backed patch antenna was subdivided into 200 elements with 373 unknowns and with unit cell dimensions of 0.1 cm x 0.5 cm x 0.5 cm. The mutual resistance and reactance as a function of frequency for an antenna mounted on different circular cylinders with radii of 25 cm, 50 cm and 100 cm are shown in Figure 5.21 and 5.22. The mutual coupling vs. frequency for these cases is shown in Figure 5.23.

From Figure 5.21 and 5.22, the absolute value of the mutual resistance and reactance at resonance have increased with increasing radius from $\rho = 25$ cm to 50 cm, then decreased with increasing radius from $\rho = 50$ cm to 100 cm. In Figure 5.23, it is observed that the difference of the magnitude of mutual coupling for the antenna mounted in a cylinder is 7.42 dB from $\rho = 25$ cm to $\rho = 50$ cm and 4.52 dB from $\rho = 50$ cm to $\rho = 100$ cm. The total difference is 11.94 dB from $\rho = 25$ cm to $\rho = 100.0$ cm. This is compared with H-plane coupling in Figure 5.16 that only has a 9.72 dB difference from $\rho = 25$ cm to $\rho = 100$ cm. Hence E-plane coupling exhibits greater curvature-dependency. Since for the E-plane arrangement the fields in the space between the patches are primarily TM, there is a stronger surface wave excitation between the patches, and the coupling is larger and demonstrates greater curvature-dependency. Also, the theoretical explanation for the effects of mutual coupling as simply due to the surface curvature for H-plane coupling is no longer completely satisfied for E-plane coupling.

This is because the field structure between the edges of the patches for E-plane coupling is different from the H-plane coupling and that fields have the least energy loss traveling at a specific curvature. It can be observed that for the E-plane coupling when the surface is curved to a specific curvature, the creeping wave travels to the other patch along the interface has lower loss, resulting in higher coupling.

For the same microstrip antenna mounted in an elliptic cylinder with major axis $a=50$ cm and minor axis $b=25$ cm, computed results for mutual resistance, reactance and coupling associated with different locations on the elliptic cylinder are shown in Figure 5.24, 5.25 and 5.26, respectively. From these results, when the antenna is embedded in the elliptic cylinder starting from $\nu_0 = 0.02$, which is a surface with significant curvature variation, the magnitude of mutual resistance and reactance are much smaller compared to values for the antenna mounted in the elliptic cylinder starting from $\nu_0 = \frac{\pi}{6}$ or $\frac{\pi}{2}$. It is also observed that the mutual coupling has little difference between $\nu_0 = \frac{\pi}{6}$ and $\frac{\pi}{2}$ in an elliptic cylinder. So the main variation for the coupling is observed when the antenna is located in the region with high curvature. For a patch antenna mounted in a circular cylinder, the maximum mutual coupling was observed when the radius of the surface curvature is around 50 cm, and not for the planar case. Comparing the E-plane coupling with H-plane coupling at the resonant frequency for the patch antenna mounted in the elliptic cylinder, it can be observed in Figure 5.19 and 5.26 that the coupling increased 11.1 dB for the patch antenna moving from $\nu_0 = 0.02$ to $\frac{\pi}{2}$ in H-plane coupling case while the coupling increased 8.9 dB for the same antenna moving from $\nu_0 = 0.02$ to $\frac{\pi}{6}$

and decreased 1.52 dB from $\nu_0 = \frac{\pi}{6}$ to $\frac{\pi}{2}$ in E-plane coupling. The total change of coupling is 10.45 dB for the patch antenna located at $\nu_0 = 0.02$ as compared to the case when the antenna is located at $\nu_0 = \frac{\pi}{2}$. It is not obvious which type of coupling is more dependent on curvature for this antenna mounted on an elliptic cylinder with $a=50$ cm, $b=25$ cm. However, it is expected that if an elliptic cylinder with $a=100$ cm, $b=25$ cm, is used, the E-plane coupling will have a still greater dependence.

Next consider the case where the second probe feed is located 0.5 cm to the right of the center point of the patch while the first probe feed remains as before. This case is shown in Figure 5.27. The mutual resistance and reactance versus frequency for the antenna mounted on circular cylinders with radii of 25 cm, 50 cm and 100 cm is shown in Figure 5.28 and 5.29, and mutual coupling (S_{12}) vs. frequency is shown in Figure 5.30. In Figure 5.28, 5.29 and 5.30, the results are generally similar to the previous E-plane coupling case except that the reactance and resistance now is opposite to the associated value in the previous E-plane coupling case. Here the mutual coupling has reached its maximum value at $\rho = 50$ cm and decreases as the radius of curvature increases or decreases. Comparing the mutual coupling with the value for the E-plane case shown in Figure 5.23, here the magnitude of the mutual coupling is much higher when the frequency is less than the resonant frequency, but is of the same order for frequency greater than the resonant frequency.

5.3.5 Numerical Results for Various Sizes of Patch Antennas

In this section the microstrip antenna with patch size of 2 cm x 2 cm, 3 cm x 3 cm and 4 cm x 4 cm are mounted in cylinders with radii of 25 cm, 50 cm and 100 cm, and the H-plane mutual coupling is calculated to assess the performance of this antenna with respect to the surface curvature. The geometry of these microstrip antennas is shown in Figure 5.31. For these cases, the two probe feeds are placed in the locations corresponding to 0.5 cm below the center point of each patch. These cavity-backed patch antennas were meshed into 200 elements with 373 unknowns and with unit cell dimensions of 0.1 cm x 0.5 cm x 0.5 cm.

For the microstrip antenna with the patch size of 4 cm x 4 cm and a separation of only 1 cm, the mutual coupling vs. frequency is shown in Figure 5.32. In Figure 5.32, compared with others, the antenna mounted in the cylinder with radius of 25 cm has the highest coupling at the resonant frequency and the coupling decreases from 13.08 dB for $\rho = 25$ cm to 16.48 dB for $\rho = 100$ cm. In this case, since the separation between two patch antennas is so small compared to the surface wavelength ($\frac{s}{\lambda_0} = 0.11$), the creeping wave traveling the region between the patches behaves similar to the case of a ground plane even though the antenna is mounted in the cylinder with the smallest radius of $\rho = 25$ cm. Therefore, the loss of energy of the creeping wave due to the curvature of cylinder can be neglected here, and the only factor that causes the decreasing of the mutual coupling is the wavelength at resonance. For $\rho = 25$ cm the resonant frequency is 3.32 GHz with a resonant wavelength of 9.06 cm while the resonant frequency is 3.38 GHz with a resonant wavelength of 8.87 cm for $\rho = 100$ cm. Thus the creeping wave

with the higher frequency and shorter wavelength has larger energy loss during traveling. That is the reason for the slightly decreased coupling when the radius of the cylinder is increased from $\rho = 25$ cm to 100 cm.

For the microstrip antenna with the patch size of 3 cm x 3 cm and the edge space of 2.0 cm, the mutual coupling vs. frequency is shown in Figure 5.33. In Figure 5.33, compared with others, the antenna mounted on a cylinder with radius of 100 cm has the highest coupling value at the resonant frequency and the coupling value decreases from 16.98 dB for $\rho = 100$ cm to 26.70 dB for $\rho = 25$ cm. In this case, since the separation between the patch antennas has increased, the wave traveling in this region cannot be treated as if traveling on a ground plane. Therefore, the energy loss of the creeping wave due to the curvature plays an important role for the mutual coupling of the microstrip antennas. For an antenna mounted in the cylinder with $\rho = 25$ cm, the two patches on the cylinder body are subtended by a larger angle, which results in attenuation of the space wave and thus weakens the coupling. The difference of coupling value between $\rho = 25$ cm and $\rho = 100$ cm is 9.75 dB in this case while it is just 3.55 dB for previous case. In this case the primary change of the coupling happens when the patch antennas are moved from a curved area to a less curved region.

For the microstrip antenna with the patch size of 2 cm x 2 cm and a separation of 3 cm, the mutual coupling vs. frequency is shown in Figure 5.34. In Figure 5.34, compared with others, the antenna mounted in the cylinder with radius of 100 cm has the highest coupling value at the resonant frequency and the coupling value decreases from 19.3 dB for $\rho = 100$ cm to 29.90 dB for $\rho = 25$ cm. In this case, the separation between the patch antennas is large enough so that the energy loss of the creeping wave due to the curvature

plays an important role for the mutual coupling of the microstrip antennas. The difference of coupling value between $\rho = 25$ cm and $\rho = 100$ cm is 10.6 dB in this case, which is slightly higher than the case with the patch size of 3 cm x 3 cm. Also, in this case the primary variation of the mutual coupling appeared when the patch antennas are removed to a pseudo-ground plane from the circular cylinder with $\rho = 50$ cm.

In Figure 5.32, 5.33 and 5.34, among all patch antennas with different patch sizes mounted in a cylinder, the coupling value is the highest for the patch with size of 4 cm x 4 cm at resonance. This is not only because the size of patch is the largest but also the edge space between the patches is the smallest. Also, the shape of the mutual coupling vs. frequency curve for the antenna with patch size of 4 cm x 4 cm is the sharpest while it is the broadest for the antenna with patch size of 2 cm x 2 cm.

5.4 Conclusion

In this chapter, the mutual coupling between patch antennas was investigated. For the microstrip antenna mounted in the infinite ground plane, the numerical results agree with the data provided by measurements and the numerical results using moment method for both E-plane and H-plane coupling. It should be noted that interactions with the side walls of the cavity can alter the coupling. Also, the cavity should be meshed into

elements with length less than $\frac{\lambda}{20}$ to have accurate results. For E-plane coupling case

with $\frac{s}{\lambda_0} < 0.2$, the length of unit cell should be less than $\frac{\lambda}{40}$ to have a reliable computed

results. Physically, for the H-plane coupling, the surface fields in the space between the patches are primarily TE and there is not as strong a dominant mode surface wave

excitation; therefore there is less coupling observed between the patches. For the E-plane coupling the fields in the space between the patches are primarily TM, therefore, the surface wave excitation is stronger between the patches and hence the coupling is greater.

For a microstrip antenna mounted on a circular cylinder and an elliptic cylinder, the mutual coupling for patch antennas is curvature-dependant. For the H-plane coupling, the coupling decreases as the radius of curvature increases. Therefore, coupling effects between patch antennas generally reaches its maximum when it is placed in the ground plane. Physically, more energy of the surface wave sheds away from the surface in a region with high curvature, which weakens the antenna coupling. However, for the E-plane coupling case, the highest coupling occurs at some specific curvature. Generally the E-plane coupling is more curvature-dependant since there is a stronger surface excitation between the patches.

However, for the numerical results and discussions for E-plane coupling on a curved surface, the mutual resistance and reactance as a function of frequency for an antenna mounted on different circular cylinders shows that the absolute value of the mutual resistance and reactance at resonance have increased with increasing radius from the radius of 25 cm to 50 cm, then decreased with increasing radius from the radius of 50 cm to 100 cm. The numerical results should be further analyzed in future work.

For microstrip antennas with different patch sizes and H-plane coupling, an antenna with larger patches and smaller separation between patches has greater coupling. The variation of the mutual coupling due to the surface curvature is more obvious when

$\frac{s}{\lambda_0} > 0.11$. The primarily change in the mutual coupling due to the variation of the

surface curvature occurs either for a region with a high curvature or for a region with a less curvature, depending on the patch size and the separation.

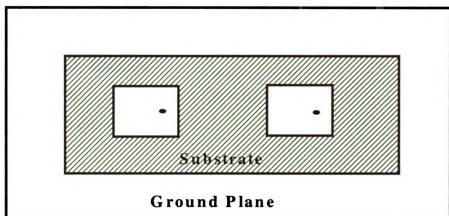


Figure 5.1 Experimental arrangement for measurement of microstrip antenna S-parameter (R.P. Jedlicka, 1981)

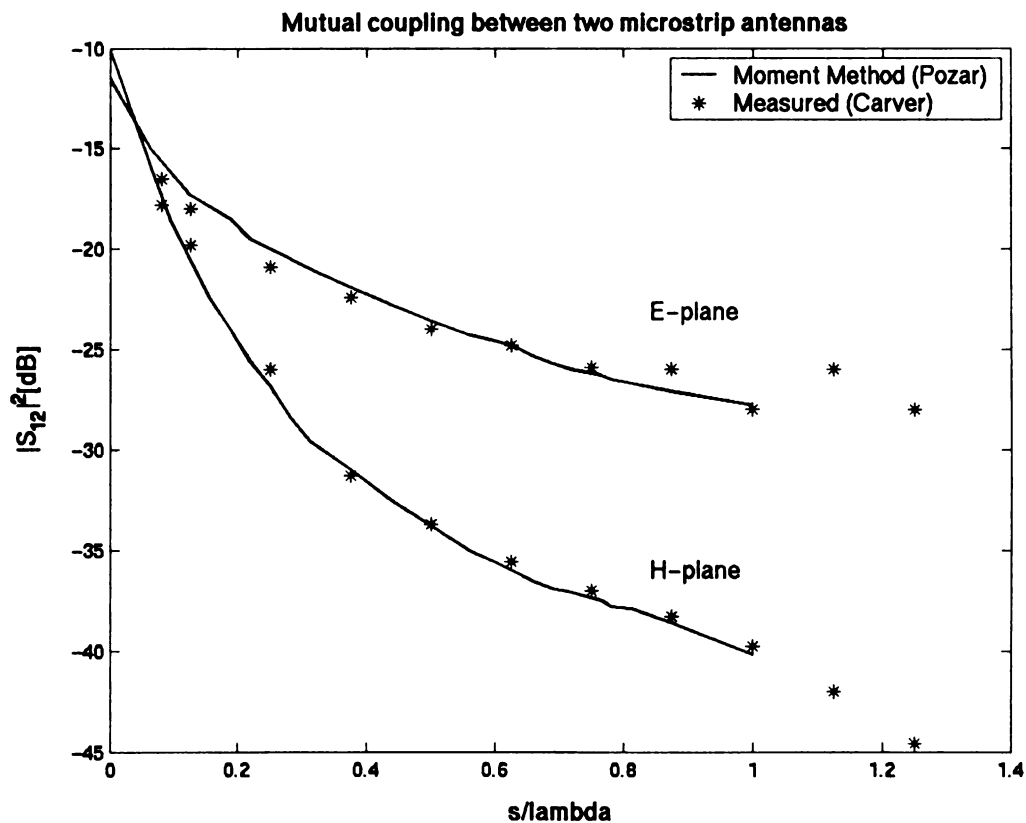
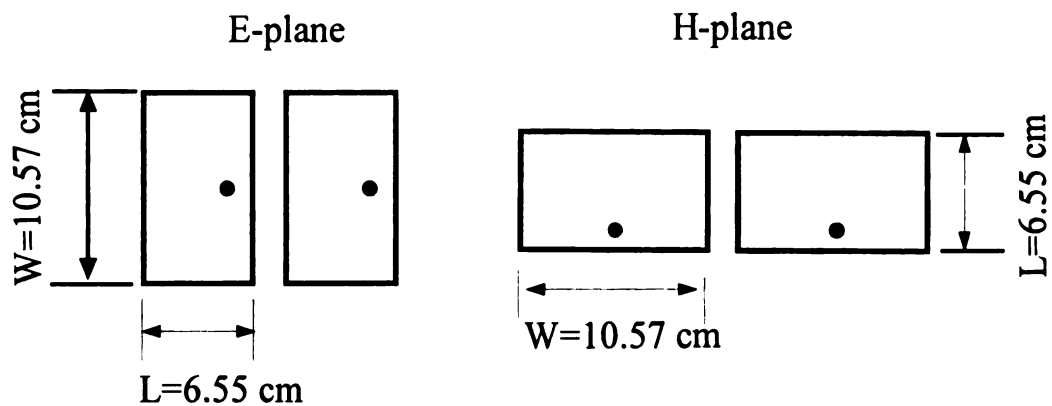
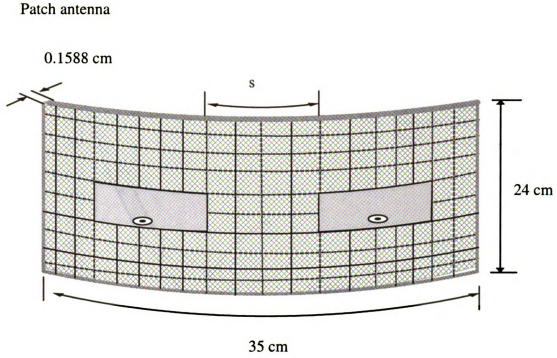


Figure 5.2 Measured and calculated mutual coupling between two coax-fed microstrip antennas, for both E-plane and H-plane coupling. $W=10.57$ cm, $L=6.55$ cm, $d=0.1588$ cm, dielectric constant ≈ 2.55 (David M. 1982).



Patch size and location of probe feed

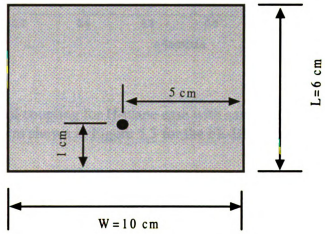


Figure 5.3 Geometry for patch antennas with H-plane coupling in pseudo-ground plane.

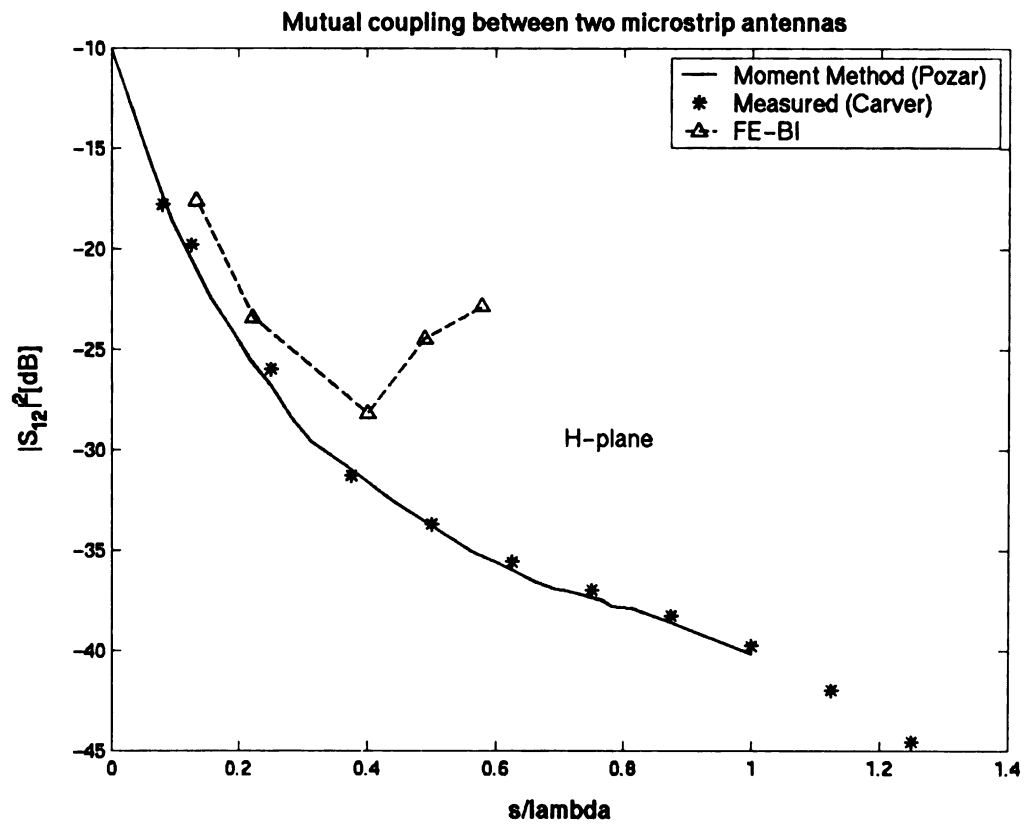


Figure 5.4 Mutual coupling for H-plane case with cavity of 0.1588. cm x 35 cm x 24 cm shown in Figure 5.3 for the FE-BI method.

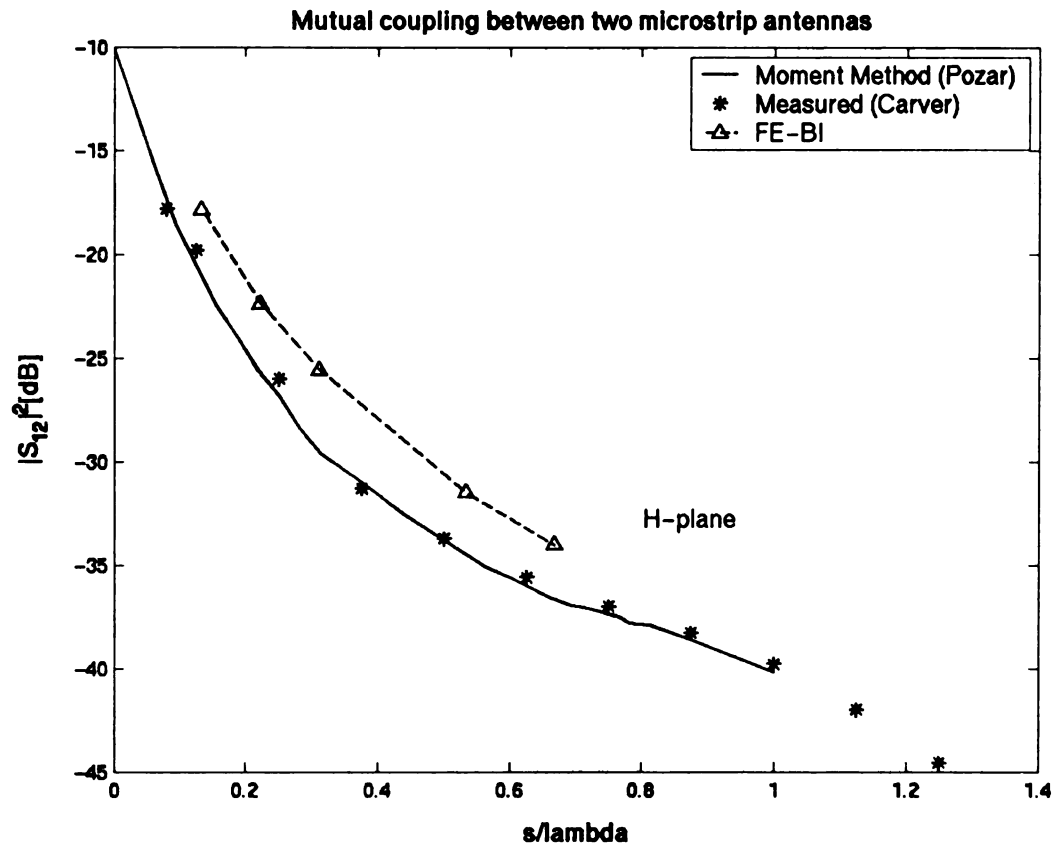


Figure 5.5 Comparison of mutual coupling calculated by FE-BI with a moment method solution and data by measurements; the size of cavity-backed antenna in FE-BI calculation is 0.1588 cm x 53 cm x 30 cm.

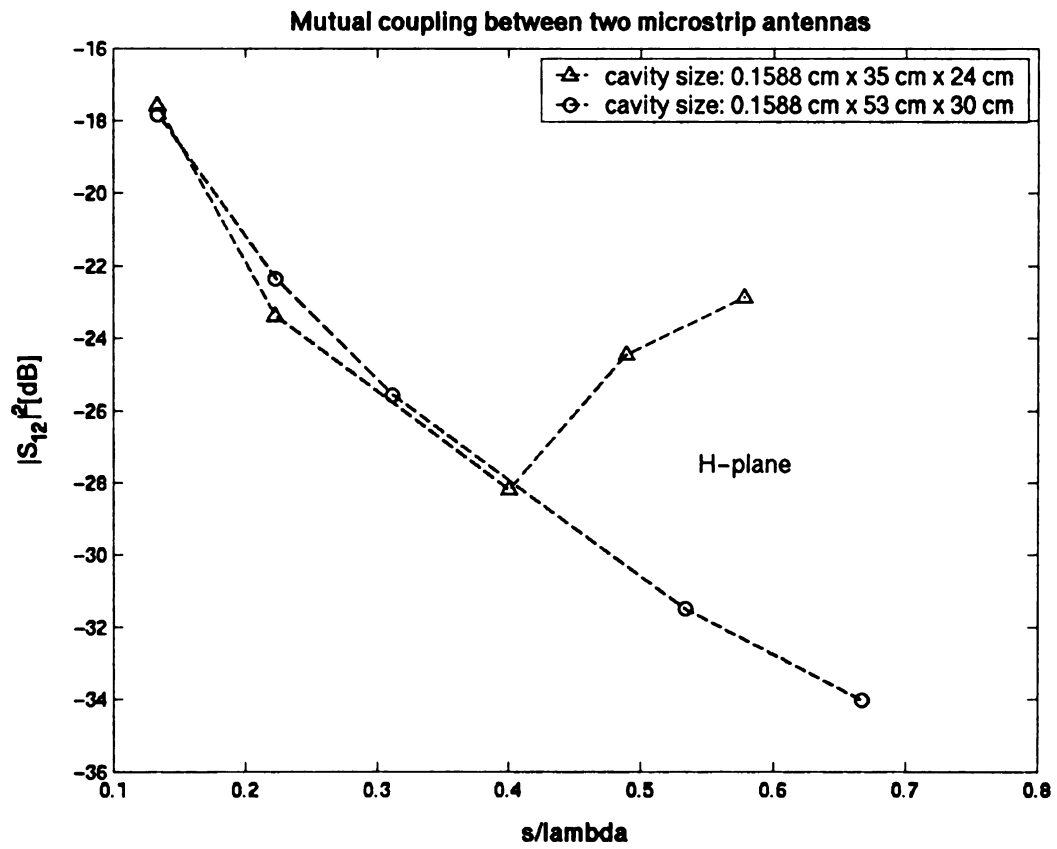
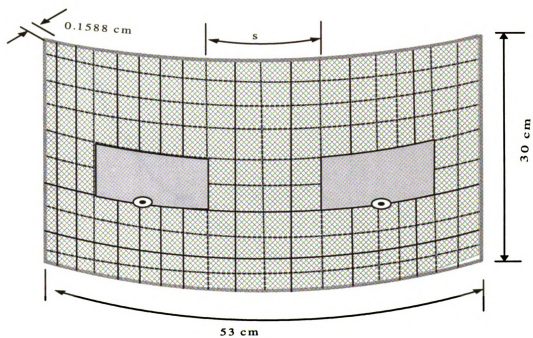


Figure 5.6 Comparison of mutual coupling using FE-BI method between different size of cavity of 0.1588 cm x 35 cm x 24 cm and 0.1588 cm x 53 cm x 30 cm.

Patch antenna



Patch size and location of probe feed

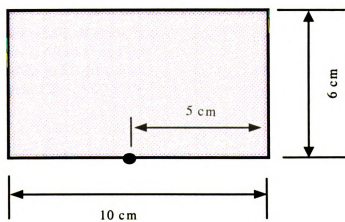


Figure 5.7 .Geometry for patch antennas with H-plane coupling in pseudo-ground plane.

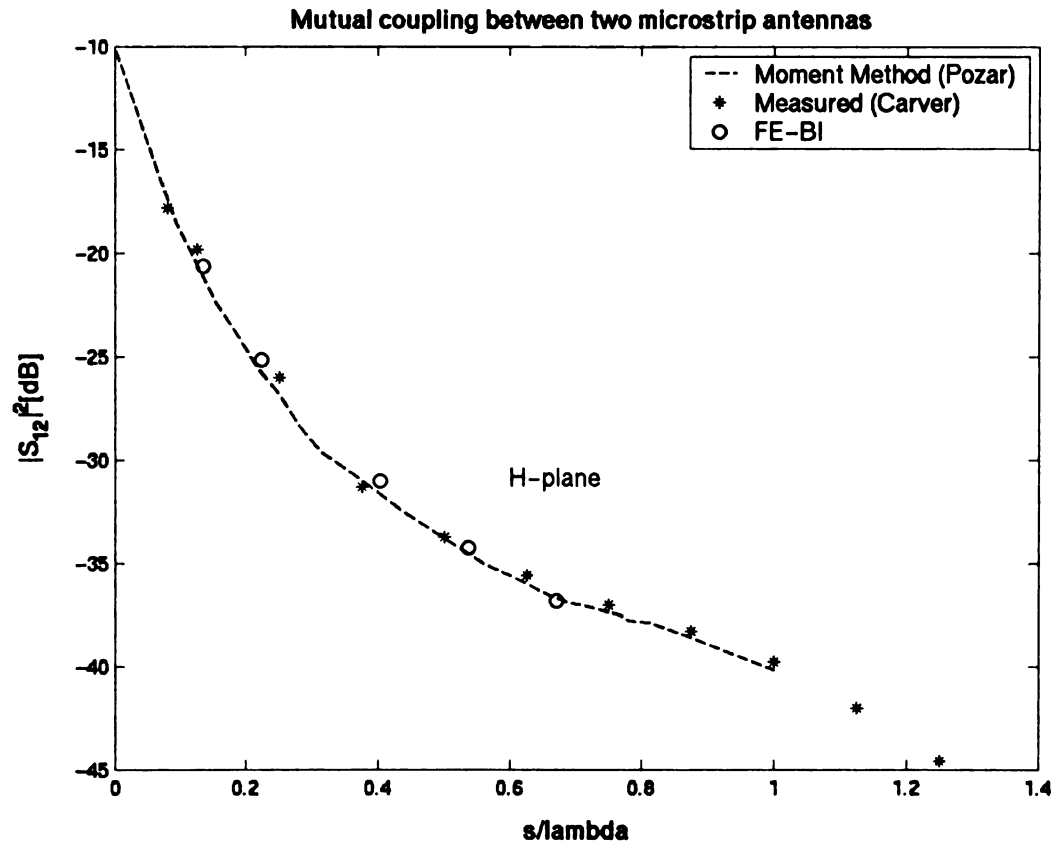


Figure 5.8 Comparison of mutual coupling calculated by FE-BI with a moment method solution and data by measurements; the size of cavity-backed antenna in FE-BI calculation is 0.1588 cm x 53 cm x 30 cm, shown in Figure 5.7.

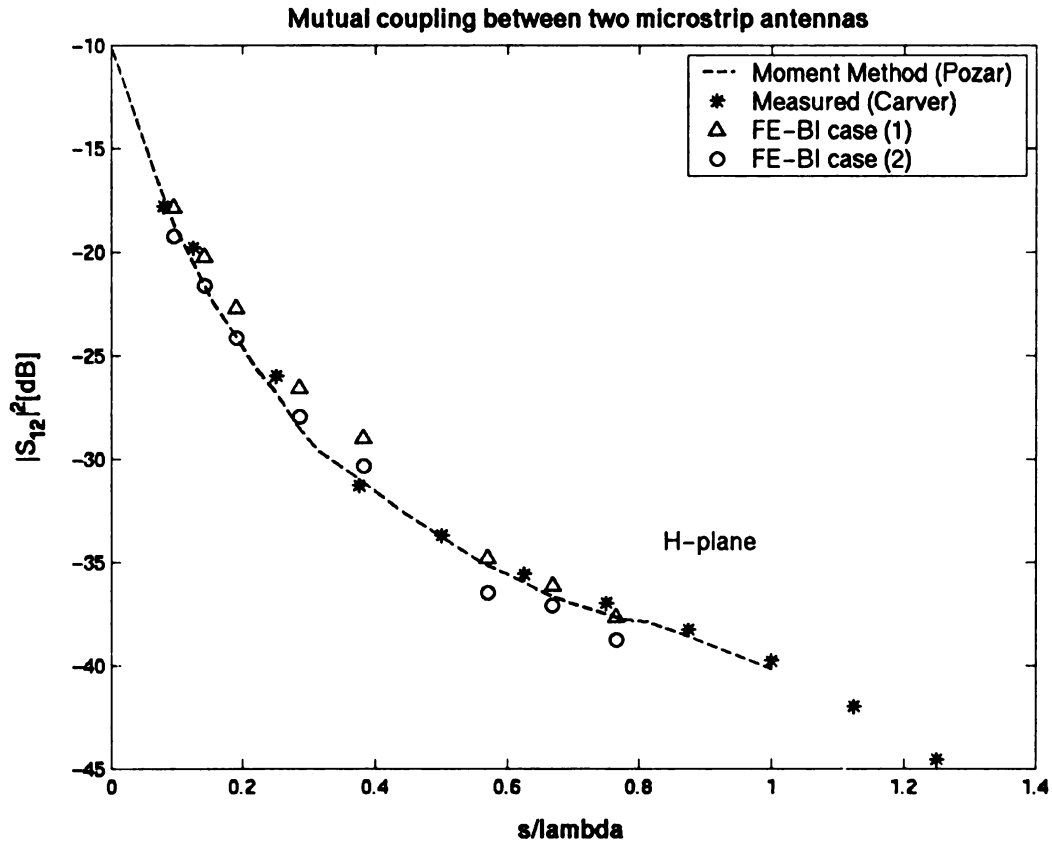
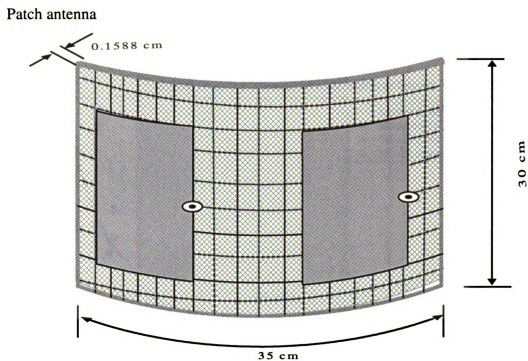


Figure 5.9 Comparison of mutual coupling calculated by FE-BI with a moment method solution and measured data; the size of cavity-backed antenna in FE-BI calculation is 0.1588 cm x 51 cm x 16 cm and unit cell of 0.1588 cm x 1 cm x 1 cm.

Pat

Pat



Patch size and location of probe feed

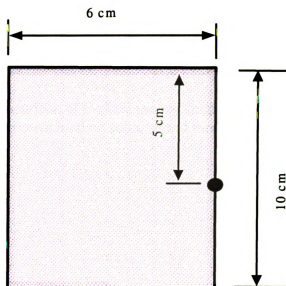


Figure 5.10 .Geometry for patch antennas with E-plane coupling in a pseudo-plane ground.

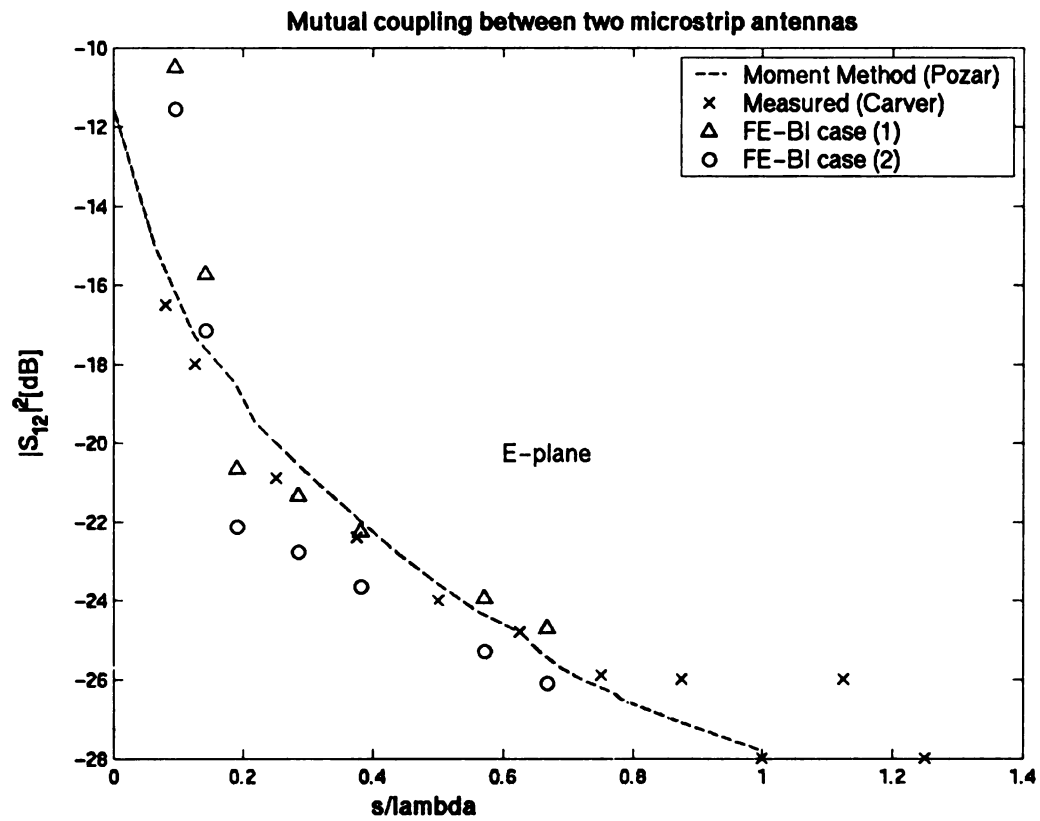


Figure 5.11 Comparison of E-plane mutual coupling calculated by FE-BI with a moment method solution and measured data.

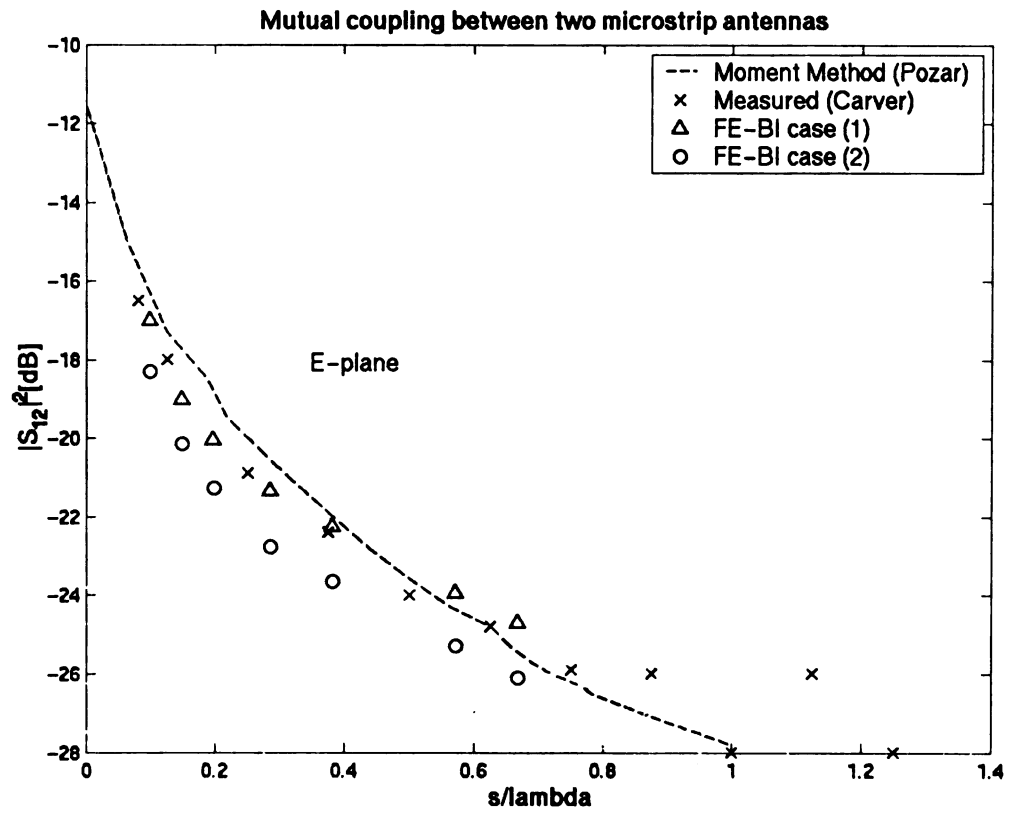
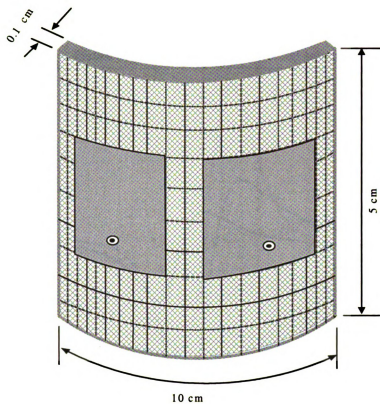


Figure 5.12 Comparison of E-plane mutual coupling calculated by FE-BI with a moment method solution and measured data.

Patch

Figure

Patch antenna



Patch size and location of probe feed

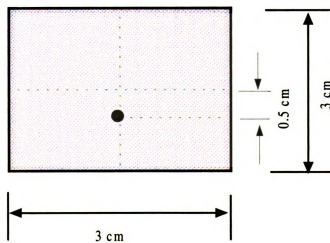


Figure 5.13 Geometry for patch antennas mounted in curved surface with H-plane Coupling.

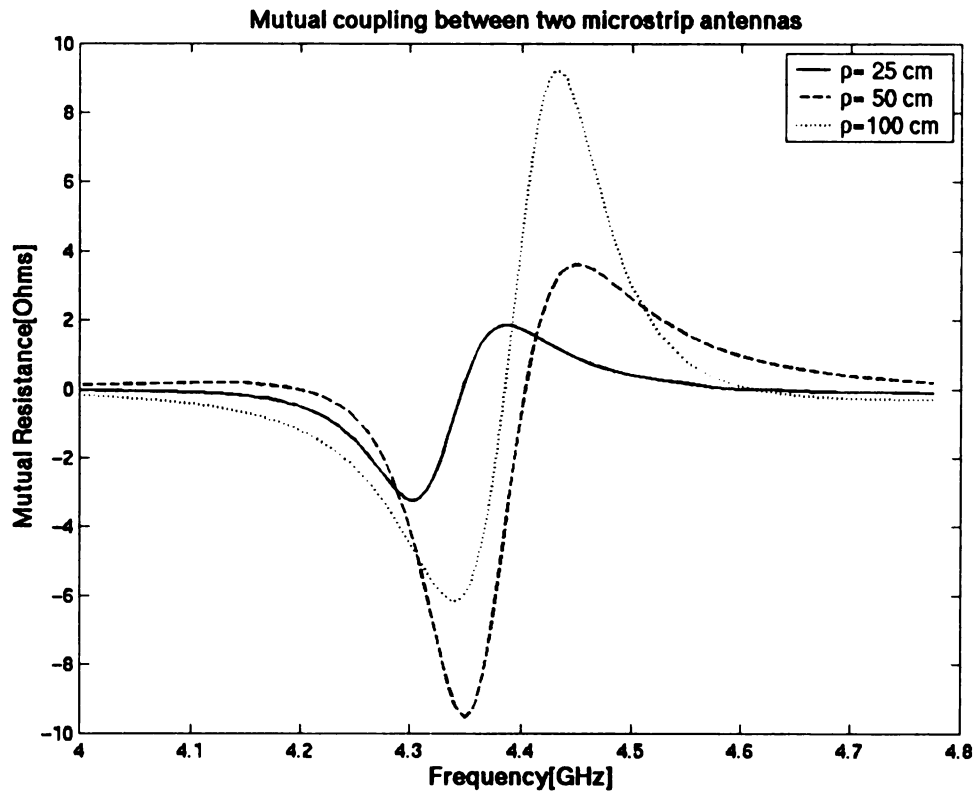


Figure 5.14 Mutual resistance for patch antennas with H-plane coupling.

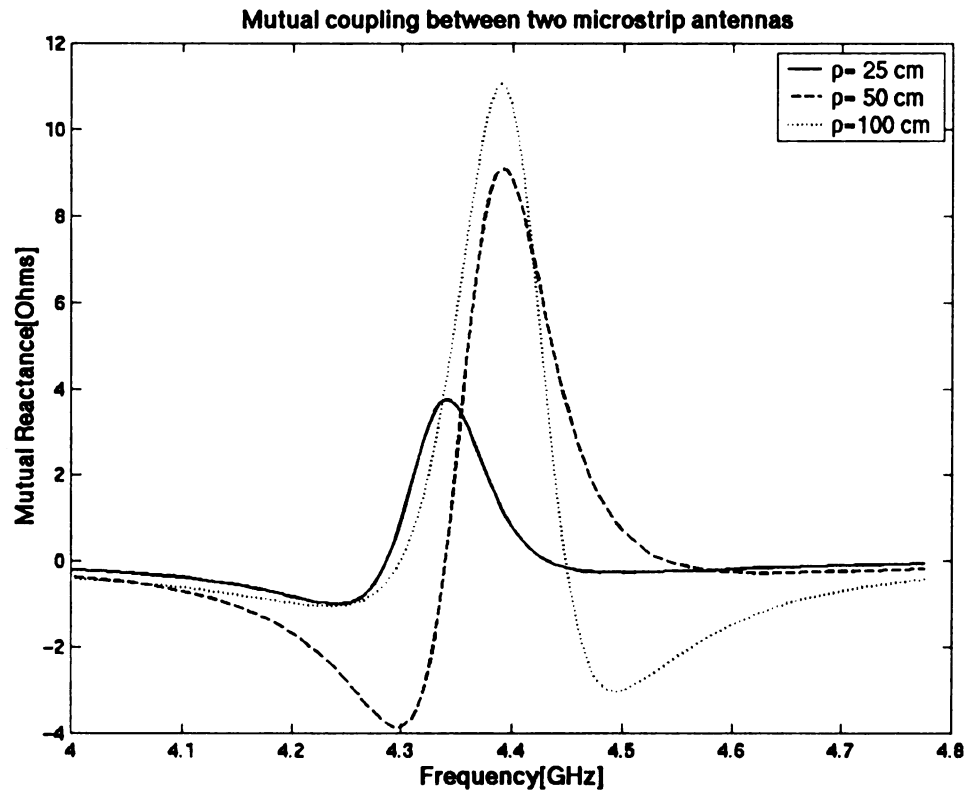


Figure 5.15 Mutual reactance for patch antennas with H-plane coupling.

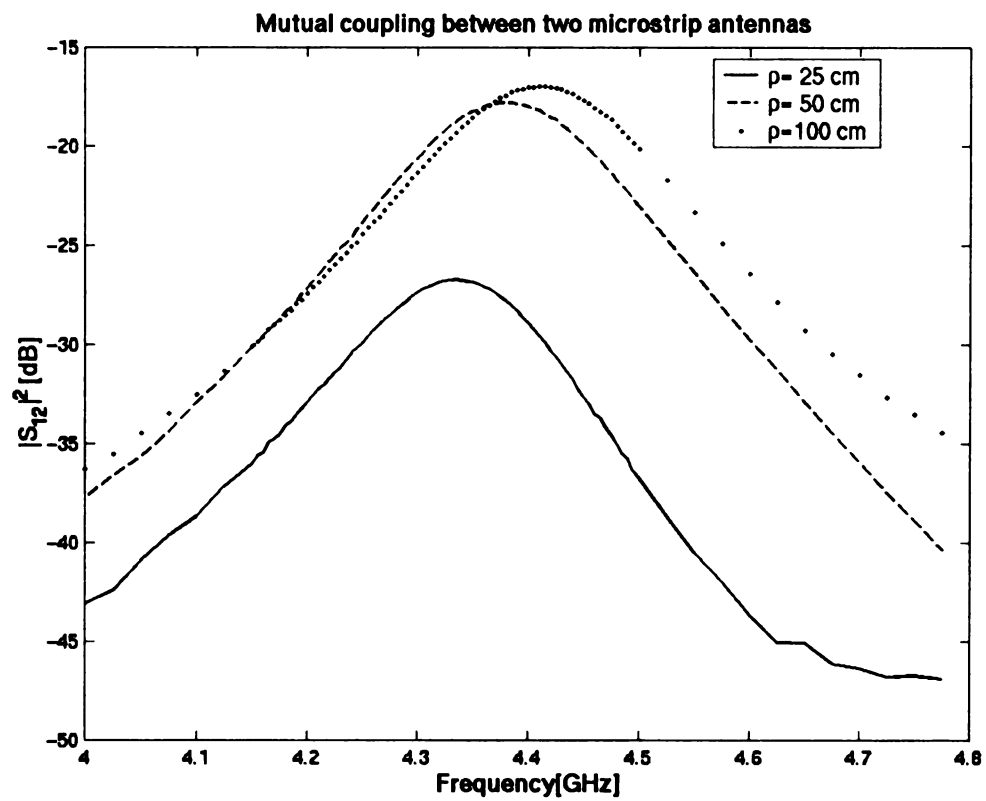


Figure 5.16 Mutual Coupling for patch antennas with H-plane coupling.

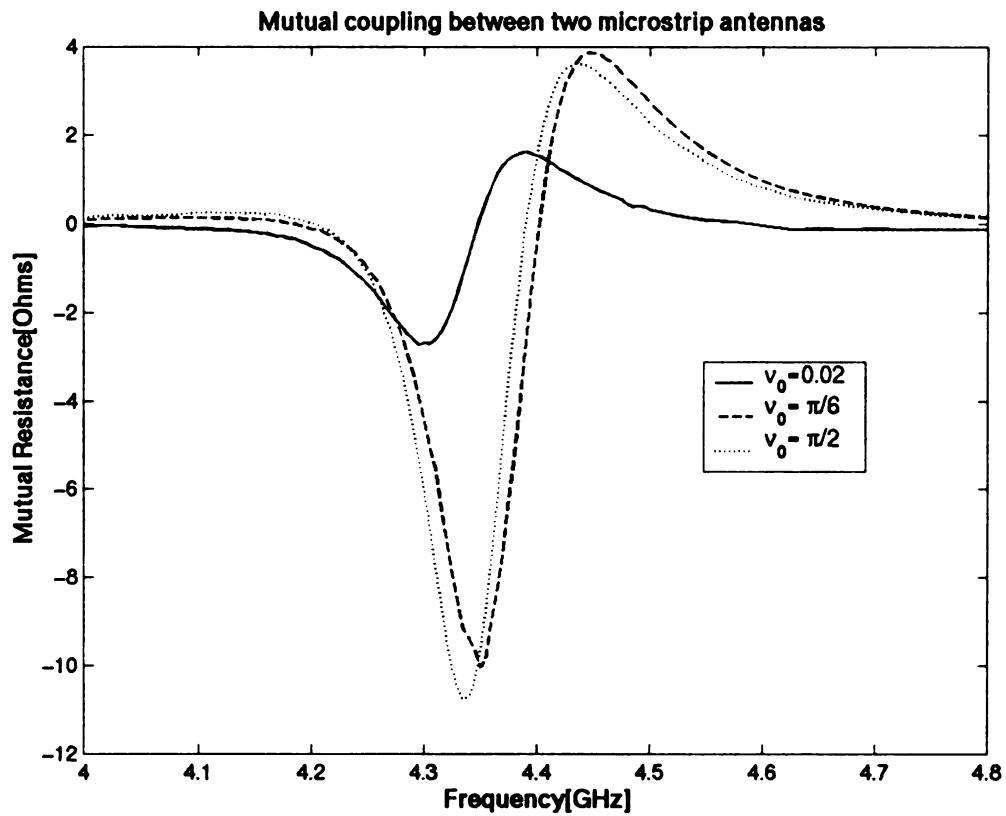


Figure 5.17 Mutual resistance for patch antennas mounted in an elliptic cylinder with H-plane coupling.

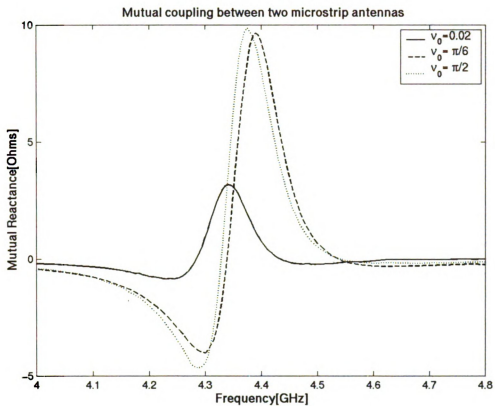


Figure 5.18 Mutual reactance for patch antennas mounted in an elliptic cylinder with H-plane coupling.

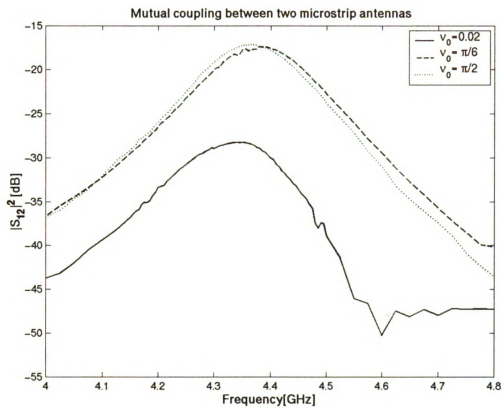
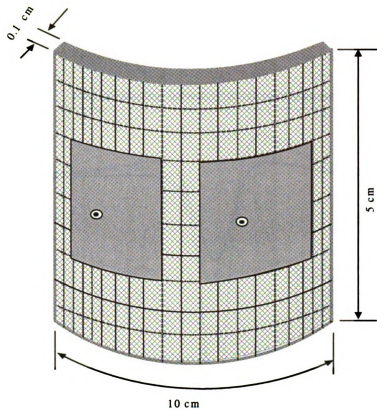


Figure 5.19 Mutual coupling for patch antennas mounted in an elliptic cylinder with H-plane coupling.

F

Fi

Patch antenna



Patch size and location of probe feed

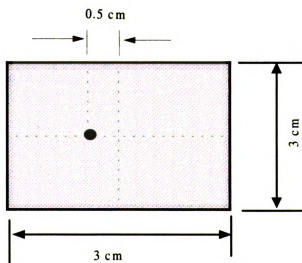


Figure 5.20 Geometry for patch antennas mounted in curved surface with E-plane coupling

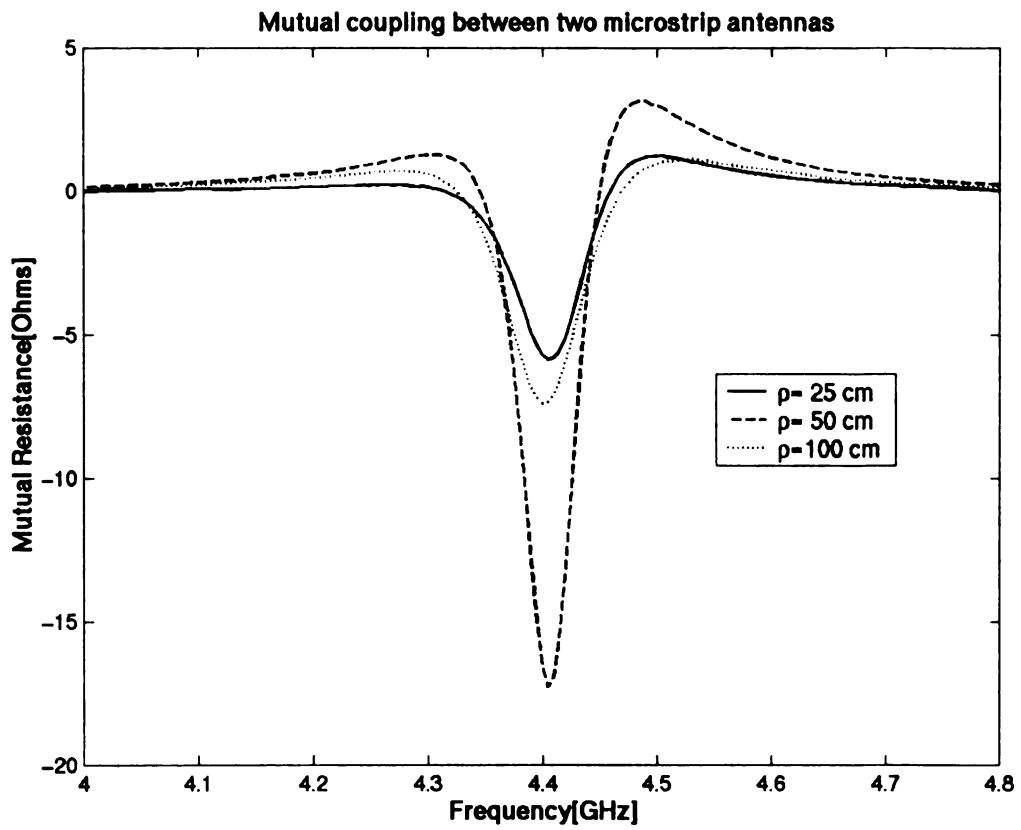


Figure 5.21 Mutual resistance for patch antennas mounted in circular cylinders with E-plane coupling.

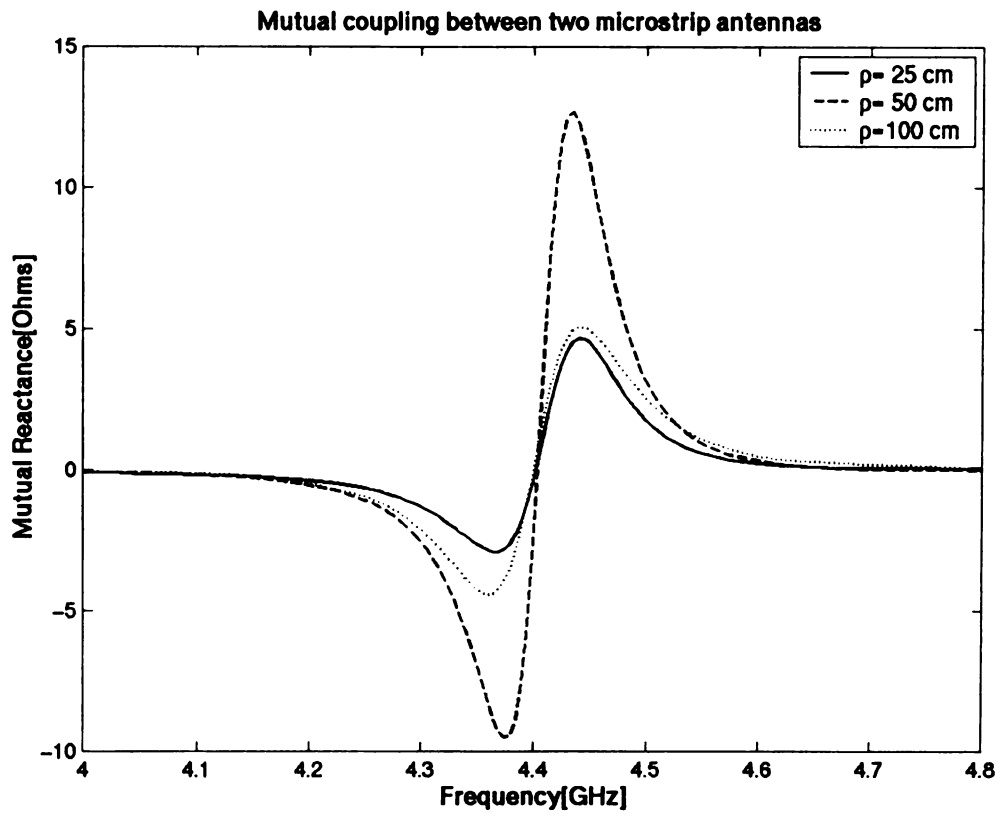


Figure 5.22 Mutual reactance for patch antennas mounted in circular cylinders with E-plane coupling.

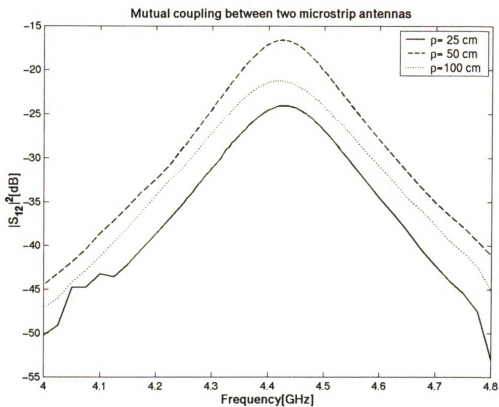


Figure 5.23 Mutual coupling for patch antennas mounted in circular cylinders with E-plane coupling.

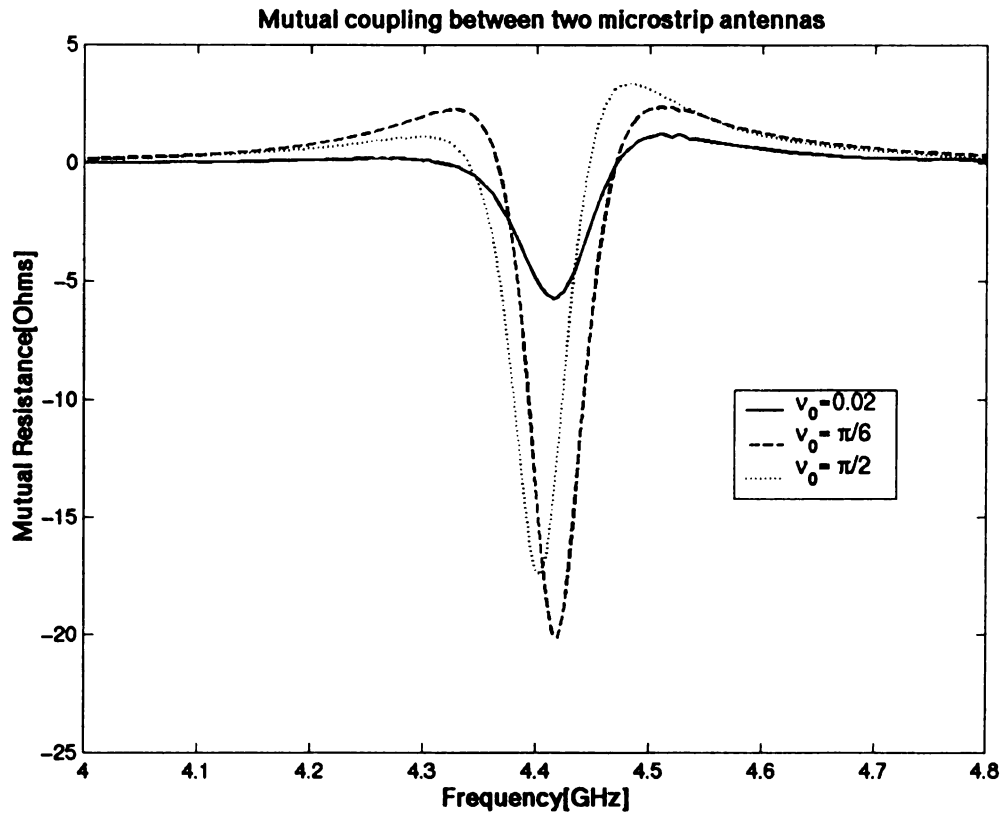


Figure 5.24 Mutual resistance for patch antennas mounted in an elliptic cylinder with E-plane coupling.

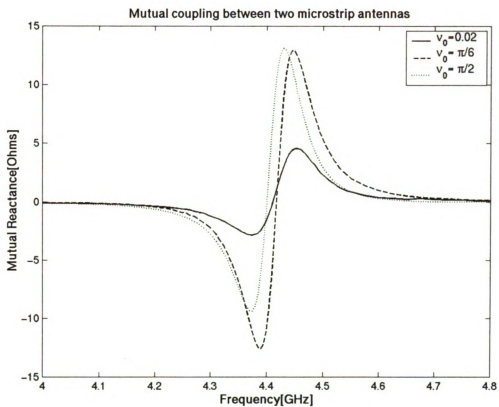


Figure 5.25 Mutual reactance for patch antennas mounted in an elliptic cylinder with E-plane coupling.

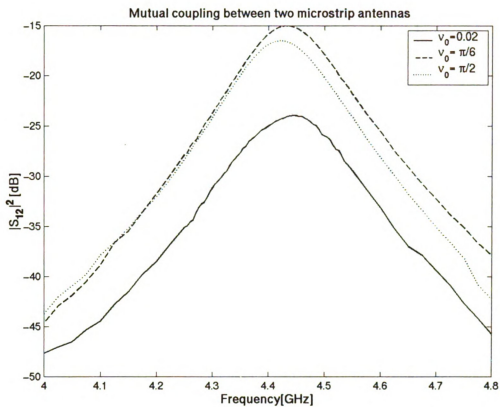
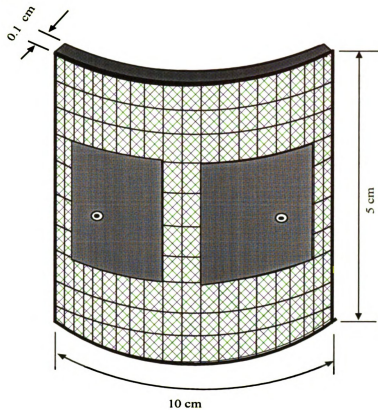


Figure 5.26 Mutual coupling between patch antennas mounted in an elliptic cylinder with E-plane coupling.

Patch antenna



Patch size and location of probe feed

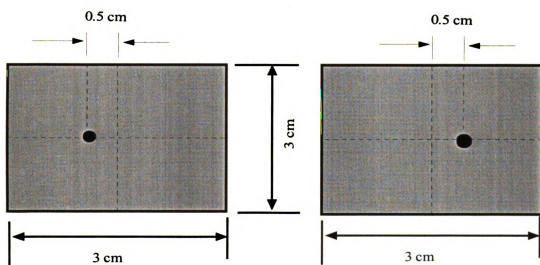


Figure 5.27 Geometry for patch antennas mounted in curved surface with special E-plane coupling

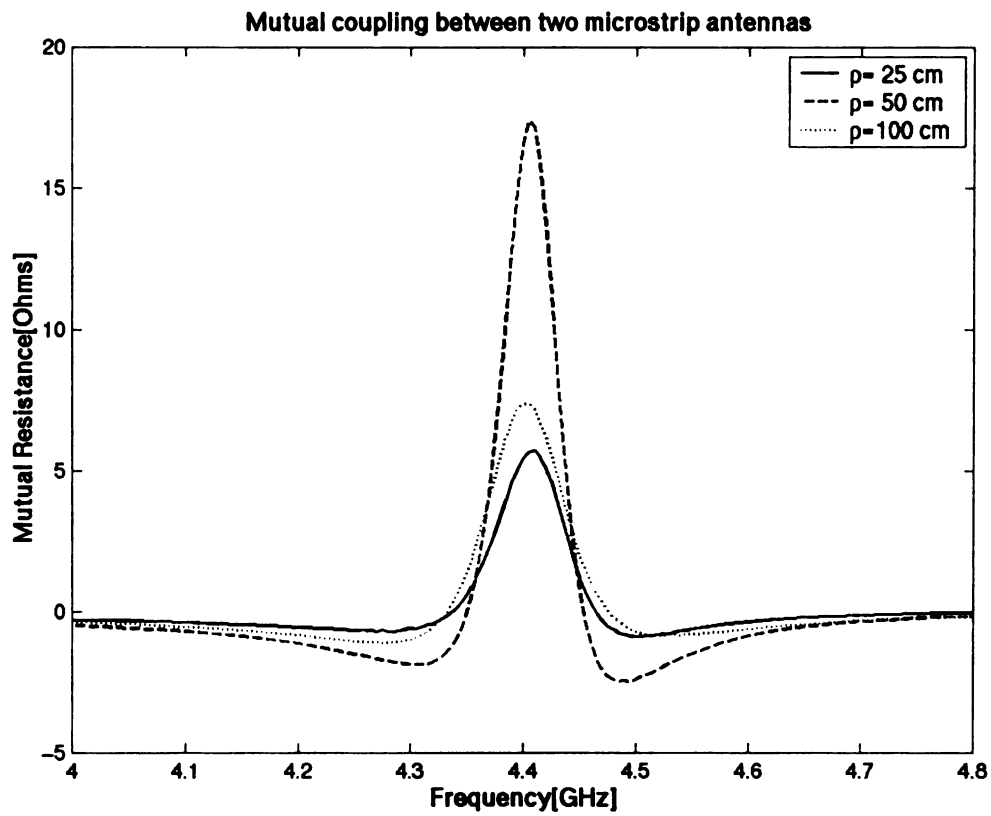


Figure 5.28 Mutual resistance for patch antennas mounted in circular cylinders with special E-plane coupling.

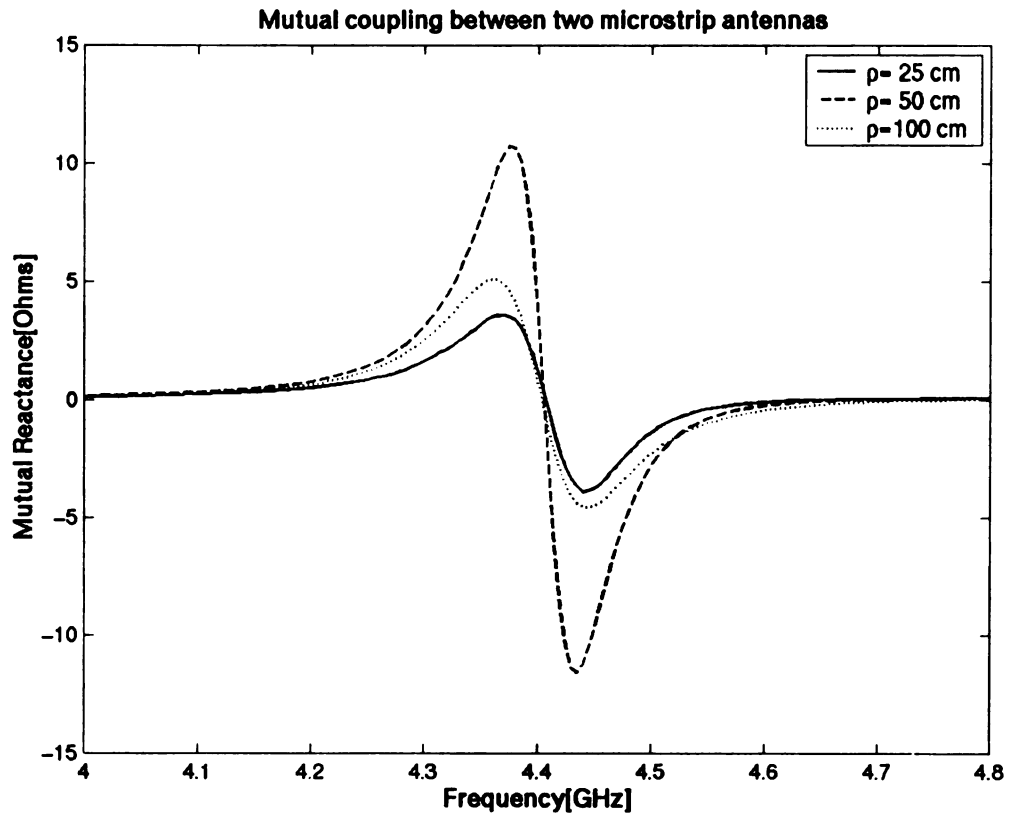


Figure 5.29 Mutual reactance for patch antennas mounted in circular cylinders with special E-plane coupling.

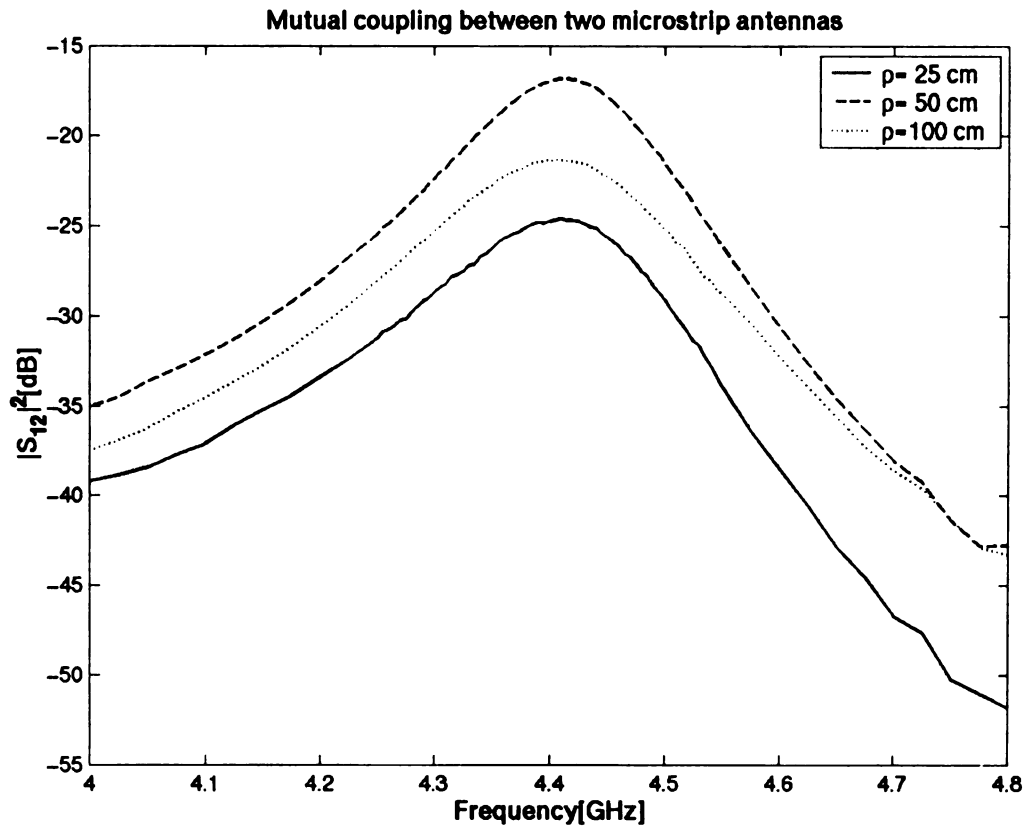


Figure 5.30 Mutual coupling for patch antennas mounted in circular cylinders with special E-plane coupling.

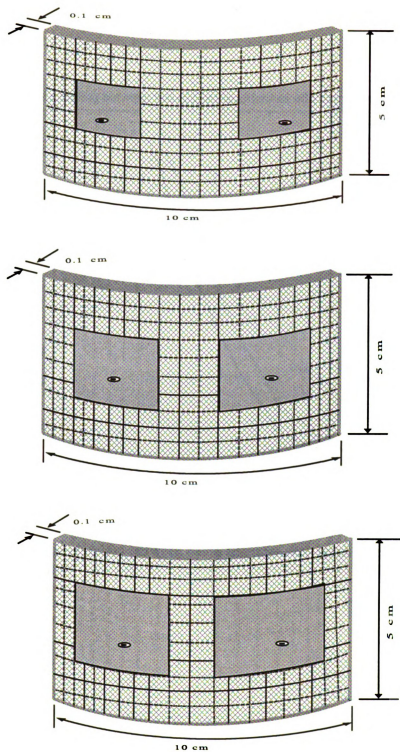


Figure 5.31 Geometry for patch antennas with patch sizes of 2 cm x 2 cm, 3 cm x 3 cm and 4 cm x 4 cm.

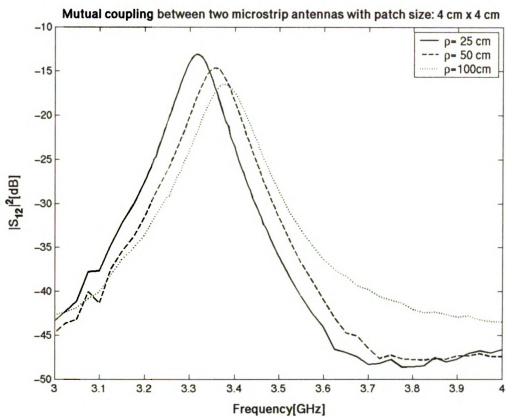


Figure 5.32 Mutual coupling between patch antennas with patch size of 4 cm x 4 cm.

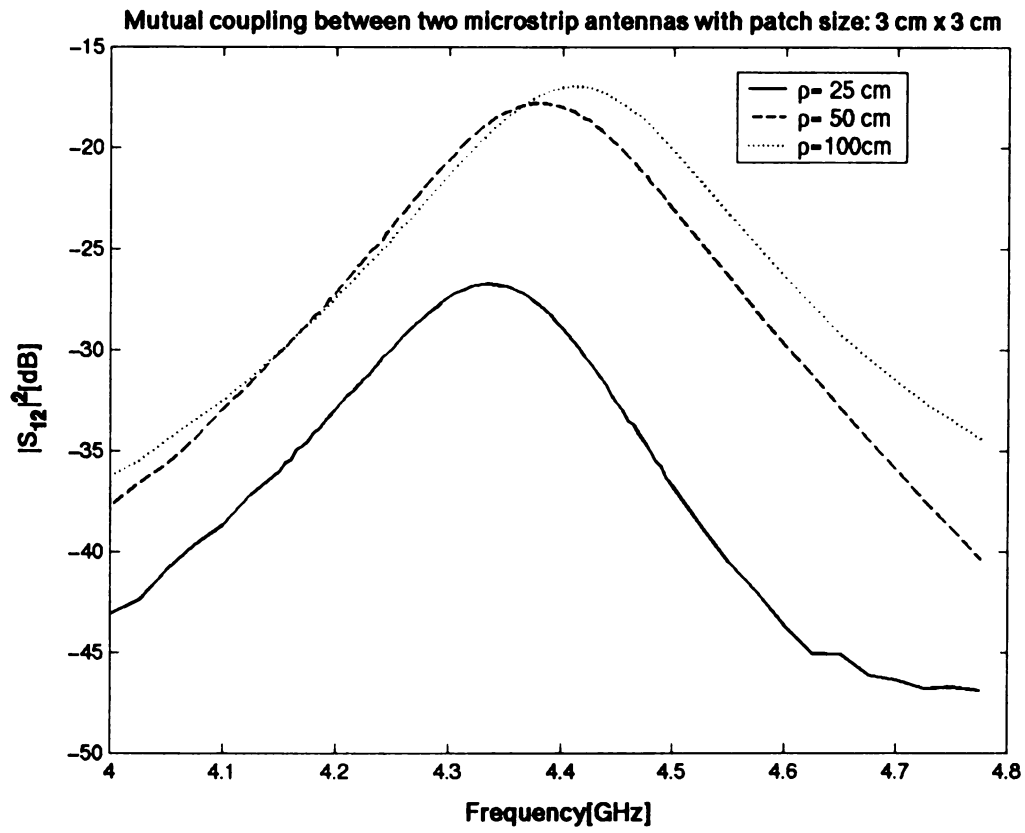


Figure 5.33 Mutual coupling between patch antennas with patch size of 3 cm x 3 cm.

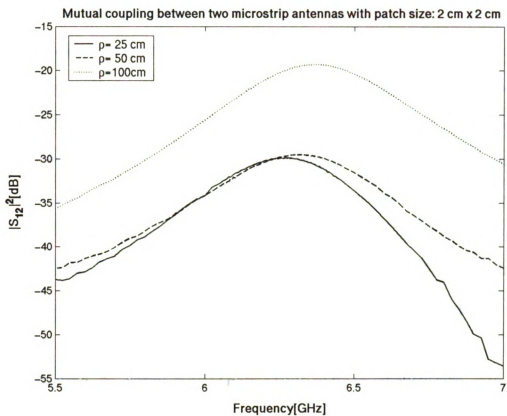


Figure 5.34 Mutual coupling between patch antennas with patch size of 2 cm x 2 cm.

CHAPTER 6

SUMMARY AND FUTURE WORK

In this dissertation, a hybrid finite element-boundary integral method has been presented that is appropriate for simulation of conformal antennas and cavities recessed in an infinite, perfectly conducting, elliptic cylinder. New elliptic-shell elements were developed that are suitable for discretizing elliptic-rectangular cavities. These shape functions are surface conforming and divergence-free. These also reduce, for cylinders whose major and minor axes are identical, to the cylindrical shell elements previously reported in [33]. The accuracy of the finite element formulation, and in particular the new elliptic shell shape functions, was demonstrated by comparison with known results for circular-rectangular and planar-rectangular cavities. Resonances for an elliptic-rectangular cavity were also presented.

In Chapter 3, the surface dyadic Green's function for an infinitely long, perfectly conducting elliptic cylinder was derived. In this approach, vector wave functions representing electromagnetic fields in the elliptic cylinder coordinate system are generated based on the elliptic cylinder scalar wave functions. Since the dyadic Green's function, developed by eigenfunction expansion, is very difficult to evaluate numerically, an efficient asymptotic dyadic Green's function was derived based on a UTD formulation [25] and this was specialized for elliptic cylinders. The behavior of this Green's function as a function of geodesic path length and curvature was demonstrated.

For solution of the linear system, several techniques have been used to reduce the large memory requirement and improve the efficiency of the solution computation. In the computer program used to demonstrate the capabilities of this new formulation, the

biconjugate gradient (BiCG) solver has been chosen since it requires significantly less memory than is required for a direct matrix solution method. The BiCG method is also computationally efficient, since it utilizes only one matrix-vector product per iteration for symmetric matrices. The Compressed Sparse Row (CSR) [34] storage format is used to reduce the memory demand for the sparse matrix. To increase the computation speed, several complicated functions like the hard and soft type Fock function have been saved in a data file to provide available data instead of requiring re-computing each time. Also, the matrix for the FEM is calculated one time only and the result is saved for later use.

The exterior and interior portions of the hybrid finite element-boundary integral computer program have been validated for the empty cavity, conformal slot antenna and conformal patch antenna. The input resistance for a typical conformal patch antenna was presented. The resonance frequency was seen to shift due to location on the elliptic cylinder and this behavior is attributed to curvature variation. The input impedance and resonant frequency are sensitive to the variation of the surface curvature for the patch antennas mounted in a region of high curvature. Therefore, the performance of the conformal antennas embedded in a region with little curvature variation can be approximated by using an equivalent circular cylinder. Such an approximation fails for the case of antennas embedded in a surface with significant curvature variation. Also, the dependence of the performance of patch antennas on curvature is relative to the excited mode associated with the location of the probe feed.

In this research the mutual coupling between two patch antennas was investigated. For the microstrip antenna mounted in an infinite ground plane, the numerical results have been shown to agree with the data provided by measurements and numerical results

using the moment method for both of E-plane coupling and H-plane coupling. It should be noted that interactions with the side walls of the cavity can alter the coupling. Also, the cavity should be meshed into elements with edge length less than $\frac{\lambda}{20}$ to obtain accurate results. For patch antennas mounted in a ground plane, the H-plane coupling and E-plane coupling have been discussed with their associated surface wave mode. Generally, for H-plane coupling the surface wave mode between the patches is primarily TE and coupling is less significant between the patches. For the E-plane coupling case, the surface wave mode is primarily TM; therefore, the surface wave excitation is stronger between the patches resulting in greater coupling.

For a microstrip antenna mounted on a circular cylinder or an elliptic cylinder, the mutual coupling for patch antennas is curvature-dependant. For the H-plane configuration, the coupling decreases as the radius of curvature increases. Therefore, coupling effects between patch antennas generally reach a maximum when the antennas are placed in a ground plane. Physically, more energy in the creeping wave is shed away from the surface in regions with high curvature, and this weakens the antenna coupling. However, for the E-plane configuration, the greatest coupling occurs at some specific curvature instead of for the ground plane case. Generally the E-plane coupling is more curvature-dependant since there is a stronger surface excitation between the patches.

For microstrip antennas with different patch size and with H-plane coupling, the antenna with larger patches and smaller separation between patches has greater coupling. The primarily change in the mutual coupling due to the variation of the surface curvature occurs for a region with either higher curvature or lower curvature, depending on the patch size and the separation.

The numerical results presented in this dissertation will serve two purposes. First, they are used to analyze the performance of antennas with respect to surface curvature. Second, they can be used as a reference for future developments in this area.

In future work, since the computation of fields near the probe feed or of fields with higher variation in space requires a fine mesh near the antenna geometry, the total number of unknowns will dramatically increase, especially when the length of the unit cell is as small as $1/50\lambda$. Therefore, the FE-BI program should be upgraded to compute the cavity field with higher efficiency and be capable of computing a model case with more than ten thousand unknowns.

A non-uniform mesh should be developed for the FE-BI program to save computation time and computer resources. Finer elliptic shell elements should be used to mesh the regions when the fields have higher variation while coarse elliptic shell elements are applied to mesh the region where fields have less variation. Distorted elliptic shell elements should be developed to transition from small to larger elements and they should retain the property of being divergence free.

For the E-plane coupling case the mutual coupling between antennas mounted on a cylinder with a specific surface curvature is maximum compared to when they are mounted on a ground plane, unlike the case for the H-plane coupling. Therefore, the relation between mutual coupling and the surface curvature should be investigated further. To achieve more accurate results, the antenna cavity should be meshed into finer unit cells to better represent variation of the fields inside the cavity and upon the aperture of the antennas.

The radiation pattern should be analyzed for the patch antennas recessed in different portions of an elliptic cylinder to realize the influence on the radiation pattern by the surface curvature. The formulation of asymptotic far-zone dyadic Green's functions in the spherical coordinate system transformed from near-zone dyadic Green's function in the elliptic coordinates system for both the lit and shadow regions should be developed and applied to the calculation of the fields.

Also, an experiment should be set up to measure the data for mutual coupling between patch antennas and for the radiation pattern of patch antennas mounted in different portions of the elliptic cylinder to verify the numerical results.

BIBLIOGRAPHY

- [1] L.C. Kempel, J.L. Volakis, and R.J. Sliva, "Radiation by cavity-backed antennas on a circular cylinder," *IEE Proc.-Microw. Antennas Propag.*, vol. 142, no. 3, June 1995.
- [2] K-L Wong, *Design of nonplanar microstrip antennas and transmission lines*, New York: Wiley, 1999.
- [3] J.T. Aberle and F. Zavosh, "Analysis of probe-fed circular microstrip patches backed by circular cavities," *Electromagnetics*, vol. 14, no. 2, pp. 239-258, April-June 1994.
- [4] D.M. Pozar and S.M. Voda, "A rigorous analysis of a microstripline fed patch antenna," *IEEE Antennas Propagat. Mag.*, vol. 35, pp.1343-1350, 1987.
- [5] J. Ashkenazy, S. Shtrikman, and D Treeves, "Electric surface current model for the analysis of microstrip antennas on cylindrical bodies," *IEEE Trans. Antennas Propagat.*, vol. AP-33, no. 3, pp. 295-300, March 1985.
- [6] L. Josefsson and P. Persson, "An Analysis of Mutual Coupling on Doubly Curved Convex Surfaces," *2001 IEEE APS Int. Symp., Dig.*, vol. 2, Boston, MA, 2001, pp. 342-345.
- [7] J.T. Aberle, D.M. Pozar, and C.R. Birtcher, "Evaluation of input impedance and radar cross section of probe-fed microstrip patch elements using an accurate feed model," *IEEE Trans. Antennas Propagat.*, 39, pp. 1691-1696, Dec. 1991.
- [8] J-M Jin, *The Finite Element Method in Electromagnetics*, New York: Wiley-Interscience, 1993.
- [9] L.C. Kempel and J.L. Volakis, "Scattering by cavity-backed antennas on a circular cylinder," *IEEE Trans. Antennas Propagat.*, 42, pp. 1268-1279, Sept. 1994.
- [10] J.L. Volakis, A. Chatterjee, and L.C. Kempel, *Finite Element Method for Engineering*, New York: IEEE Press, 1998.
- [11] C-T Tai, *Dyadic Green Functions in Electromagnetic Theory*, 2nd ed., Piscataway, NJ: IEEE Press, 1994.

- [12] P.H. Pathak and N.N. Wang, "An analysis of the mutual coupling between antennas on a smooth convex surface," Final Report 784583-7, Ohio State University ElectroScience Laboratory, Dept. Elec. Eng., Oct. 1978.
- [13] E. H. Newman and P. Tulyathan, "Analysis of microstrip antennas using moment methods," *IEEE Trans. Antennas Propagat.*, vol. AP-29, pp. 47-53, Jan. 1981.
- [14] David M. Pozar, "Input impedance and mutual coupling of rectangular microstrip antennas," *IEEE Trans. Antennas Propagat.*, vol. AP-30, No.6, Nov. 1982.
- [15] R. P. Jedlicka, M. T. Poe, and K. R. Carver, "Measured mutual coupling between microstrip antennas," *IEEE Trans. Antennas Propagat.*, vol. AP-29, pp. 147-149, Jan. 1981.
- [16] P. Silvester and M.S. Hsieh, "Finite-element solution of 2-dimensional exterior field problem," *Proc. Inst. Elec. Eng.*, vol. 118, pp. 1743-1747, Dec. 1971.
- [17] B.H. McDonald and A. Wexler, "Finite-element solution of unbounded field problems," *IEEE Trans. Microwave Theory Tech.*, vol. 20, pp. 841-847, Dec. 1972.
- [18] J-M Jin and J.L. Volakis, "A finite element boundary integral formulation for scattering by three-dimensional cavity-backed apertures," *IEEE Trans. Antennas Propagat.*, vol. 39, No. 1, pp. 97-104, Jan. 1991.
- [19] J-M Jin and J.L. Volakis, "A hybrid finite element method for scattering and radiation by microstrip patch antennas and arrays residing in a cavity," *IEEE Trans. Antennas Propagat.*, vol. 39, No. 11, pp. 1598-1604, Nov. 1991.
- [20] J-M Jin and J.L. Volakis, "Electromagnetic scattering by and transmission through a three-dimensional slot in a thick conducting plane," *IEEE Trans. Antennas Propagat.*, vol. 39, No. 4, pp. 543-550, Apr. 1991.
- [21] Robert E. Collin, *Field Theory of Guided Waves*, Oxford: IEEE Press, 1991.
- [22] Z.J. Cendes, "Vector finite elements for electromagnetic field computation," *IEEE Trans. Magnetics*, vol. 27, No. 5, pp. 3958-3966, Sept. 1991.
- [23] A. Chatterjee, J-M. Jin, and J.L. Volakis, "Computation of cavity resonances using edge-based finite elements," *IEEE Trans. Microwave Theory Tech.*, vol. 40, No. 11, pp. 2106-2108, Nov. 1992.
- [24] L.C. Kempel and J.L. Volakis, "Radiation and scattering by cavity-backed antennas on a circular cylinder," Technical Report for NASA Grant NAG-1-1478, 030601-1-T, July 1993.

- [25] P.H. Pathak and N.N. Wang, "A uniform GTD solution for the Radiation from Sources on a Convex Surface," *IEEE Trans. Antennas Propagat.*, vol. AP-29, No. 4, July 1981.
- [26] Shanjie Zhang, and Jianming Jin, "Computation of Special Functions," New York: Wiley-Interscience, 1996.
- [27] M. Abramowitz and I.A. Stegun, "Handbook of Mathematical Functions with Formulas, Graphs, and Mathematical Tables," U.S. Department of Commerce National Bureau of Standards Applied Mathematics Series 55.
- [28] Julius Adams Stratton, "Electromagnetic Theory," McGraw-Hill, 1941.
- [29] N.A. Logan, "General research in diffraction theory," Lockheed Aircraft Corp., Missiles and Space Div., vol. 1 and 2, Report LMSD-28808, Dec. 1959.
- [30] Constantine A. Balanis, "Advanced Engineering Electromagnetics," John Wiley & Sons, 1989.
- [31] Constantine A. Balanis, "Antenna theory Analysis and Design," John Wiley & Sons, 1997.
- [32] David M. Pozar "Microwave Engineering," John Wiley & Sons, 1998.
- [33] L.C. Kempel and J.L. Volakis, "A finite element-boundary integral method for conformal antenna arrays on a circular cylinder," Technical Report for NASA Grant NCA2-543, 027723-6-T, July 1992.
- [34] R. Mittra, A.W. Peterson, and S.L. Ray, "Computational Methods for Electromagnetics," New York: IEEE Press, 1998.